Studies on tiny and huge seismic sources using long period surface waves: From the hum to 2004 Sumatra-Andaman earthquake.

by

Junkee Rhie

B.S. (Seoul National University) 1995
M.S. (Seoul National University) 2000

A dissertation submitted in partial satisfaction of the
requirements for the degree of
Doctor of Philosophy

in

Geophysics

in the

GRADUATE DIVISION
of the
UNIVERSITY of CALIFORNIA at BERKELEY

Committee in charge:

Professor Barbara Romanowicz, Chair
Professor Douglas Dreger
Professor David Brillinger

Spring 2006

The dissertation of Junkee Rhie is approved:

Chair Date

Date

Date

University of California at Berkeley

Spring 2006

Studies on tiny and huge seismic sources using long period surface waves: From the hum to 2004 Sumatra-Andaman earthquake.

by

Junkee Rhie

Abstract

Studies on tiny and huge seismic sources using long period surface waves: From the hum to 2004 Sumatra-Andaman earthquake.

by

Junkee Rhie
Doctor of Philosophy in Geophysics

University of California at Berkeley

Professor Barbara Romanowicz, Chair

We study the source processes of two extreme cases, the hum of the Earth and the 2004 great Sumatra-Andaman earthquake, by using long period surface waves.

To study the source mechanism of the hum, we develop an array-based method to detect and locate very weak sources of long period surface waves, utilizing the dispersive properties of Rayleigh waves. We observe the variations in seismic amplitudes at two regional arrays: BDSN (in California) and F-net (in Japan). Our results indicate that the sources of the hum are primarily in the oceans and the dominant source regions are shifting from northern Pacific to southern oceans during northern hemispheric winter and summer, respectively. The comparison of short term variations in seismic amplitudes between the arrays and the comparison of variations in seismic amplitudes to ocean wave measurements at the coasts near the two arrays indicate that the source process consists of three steps: 1) energy conversion from atmospheric perturbation (e.g., storm) to short period ocean waves, 2) non-linear interactions of short period ocean waves to generate long period ocean waves (e.g., infragravity waves), 3) non-linear coupling of long period ocean waves to the seafloor to develop long period surface waves . In step 3, a portion of the infragravity wave can leak, propagate through the ocean, and couple to the seafloor on the other side of the ocean.

To study the very complex source process of the 2004 great Sumatra-Andaman earthquake, we jointly invert the long period (100-500 s) global seismic waveforms and near field GPS static offsets for slip distribution on the fault plane. The sensitivity test of rupture velocity indicates that the optimal rupture velocities range from 1.8 to 2.6 km/s. Our data set is not sensitive to the dip and curvature of the fault plane. We apply a Jackknife method to estimate the uncertainty in slip distribution over the given fault plane, and find that slip is well resolved along the whole rupture with uncertainties less than 23 %. Our preferred model suggests that the Sumatra-Andaman earthquake had a magnitude of M_w 9.25 +0.022 / -0.024. However, possible contamination of near-field GPS data by additional post-seismic deformation suggests that we may be slightly overestimating M_w.

Professor Barbara Romanowicz
Dissertation Committee Chair

Contents

List of Figures

List of Tables

Acknowledgements

I sincerely thank Barbara Romanowicz, my supervisor, for her helpful advice and encouragement. The first three years had a been very hard time for me because of the very slow progress on my research. As I remember, I was nearly about to change the subject of the Ph.D. thesis. She has always showed me her endless enthusiasm for sciences and positive attitude to my work. It has really encouraged me to keep studying this topic and finally finish it.

I also thank two other dissertation committee members: Doug Dreger and David Brillinger. Doug is my co-supervisor of my Ph.D. research and I have really enjoyed working with him. Discussions with him have been very helpful to understanding various aspects of the seismology. David Brillinger is a professor of statistics and he taught me the power of statistics in various scientific fields in his time series analysis class.

I would like to express my gratitude to Lane Johnson, Michael Manga, Roland Bürgmann, Bob Uhrhammer and Mark Murray for their enthusiastic teaching, helpful advice and collaboration.

I want to give my thanks to former and current colleagues at Berkeley Seismological Laboratory. Thanks to Yuancheng Gung, Hrvoje Tkalčić, Wu-Cheng Chi, Akiko To, David Dolenc, Mark Panning, Sébastien Rousset, Aimin Cao, Ahyi Kim, Dennise Templeton, Vedran Lekic, Mei Xue, Sean Ford, Alexey Shulgin, Yann Capdeville, Ludovic Bréger, Federica Marone, Fabio Cammarano and all BSL staff for their assistances.

I wish to express my gratitude to my parents and sister in Korea for their love. I am sure that I could have not finished this without their help.

I am indebted to people in the Berkeley Central Presbyterian Church in Berkeley for their love and encouragements in Christ.

Finally, I want to give my thanks from deep in my heart to God for letting me know him, guiding me, allowing me to know a tiny piece of the secret of the world he created, and making me believe that he will let me know more in the future.

Chapter 1

Introduction

In this dissertation, we study the tiniest and largest seismic sources by using long period surface waves. Long period surface waves are dominant and/or only detectable phase in most seismograms regardless of the size of the seismic sources. Therefore, they are very useful both in the study of the mechanism of very tiny seismic sources (e.g., the incessant excitation of the Earth's free oscillations) and for the study of the first order characteristics of very large and complex seismic sources, such as the 2004 great Sumatra-Andaman earthquake.

The great Chilean earthquake of May 22, 1960 made possible the first observations of free oscillations of the Earth [*Benioff et al.,* 1961]. Since then the excitation of free oscillations have been considered as transient phenomena generated by earthquakes or volcanic eruptions [*Kanamori and Mori,* 1992], because large earthquakes and volcanic eruptions are not frequent enough to sustain the observable free oscillations even if we include relatively rare slow/silent earthquakes [*Beroza and Jordan,* 1990]. Recent development of seismic sensors and deployment of global seismic stations allow us to detect the incessant excitation of the Earth's free oscillations. Hereafter, we refer to this excitation as the hum of the Earth, for short. Since its first observation in 1998, many observational and theoretical studies have been done by many researchers to

resolve the excitation source mechanism and dominant source regions as well. For the first time, the observation of the evidence for oceanic origin of the hum and possible mechanism is reported [*Rhie and Romanowicz,* 2004]. The study of the hum of the Earth using long period surface waves is a main topic of this dissertation.

In chapter 2, we develop and apply an array-based method, which utilizes the propagation properties of long period Rayleigh waves to study the hum. This approach is different from many previous studies using the standing wave approaches [*Nawa et al.,* 1998; *Suda et al.,* 1998; *Tanimoto et al.,* 1998] or the correlation of signals across full great-circle paths [*Ekström,* 2001], which are not appropriate to locate the sources. After painstaking optimization and tuning of the method, we were able to detect some important characteristics of the hum, which have not been reported nor observed before, by using two regional arrays in California (Berkeley Digital Seismic Networks) and Japan (F-net): The locations of the hum sources are primarily in the ocean and they shift seasonally from northern Pacific to the southern ocean during northern hemisphere winter and summer, respectively. Based on this observation, we confirm the hypothesis of the oceanic origin of the hum [*Watada and Masters*, 2001; *Tanimoto,* 2003; *Rhie and Romanowicz*, 2003] and suggest probable mechanism of the hum by atmosphere-ocean-sea floor coupling. This work has been published in *Nature* under the reference [*Rhie and Romanowicz,* 2004].

The more detailed excitation process of the hum inferred from the comparison of the short term variations in long period seismic amplitudes at two arrays and ocean wave measurements by buoys near California and Japan coast is documented in chapter 3. We observe significant time delays ($\sim$ 8 hour) of arrival times of the peaks related to hum events at the two arrays. The peak arrives at BDSN earlier than the corresponding peak at F-net. This observation implies that the actual locations of energy conversion from ocean wave to solid Earth for BDSN and F-net are likely to be different. The variations in long period seismic amplitudes correlate well with the ocean wave measurements at buoys during the period of no large earthquakes. We find evidence for cross continental propagation of the long period seismic energy observed

at the array near the California coast (BDSN). We also observe correlation between the variation in long period and short period seismic amplitudes at two arrays during northern hemisphere winter. This observation indicates that the two oceanic origin seismic sources such as the hum (long period) and microseisms (short period) basically have the same mechanism during northern hemispheric winter. Chapter 3 has been submitted to *Geochemistry Geophysics Geosystems* under the reference [*Rhie and Romanowicz*, 2006a].

In chapter 4, we switch gears to very large and transient seismic sources instead of the tiny and continuous ones (the hum of the Earth). However, we still use long period surface waves to study the source. The 2004 Sumatra-Andaman event is a very important event because it is the first well recorded great event since global deployment of seismic and geodetic stations. The source study of a great earthquake is very difficult because it is very complex. Many different data sets with different frequency contents, such as short period P waveforms [*Ishii et al.*, 2005], long-period normal modes [*Park et al.*, 2005; *Stein and Okal*, 2005], long period waveforms [*Tsai et al.*, 2005], broad band seismic waveforms [*Ammon et al.*, 2005] and geodetic data [*Banerjee et al.*, 2005; *Subarya et al.*, 2006; *Vigny et al.*, 2005], can be used to study the source. We jointly invert global seismic waveforms and near field static offsets for slip distribution over multiple fault planes. Although our slip model cannot show very detailed source process, it is appropriate to understand first order characteristics of the 2004 Sumatra-Andaman event. Chapter 4 has been submitted to the *Bulletin of the Seismological Society of America* under the reference [*Rhie et al.*, 2006b]

Chapter 2

Excitation of Earth's continuous free oscillations by atmosphere-ocean-seafloor coupling

This chapter has been published in *Nature* [*Rhie and Romanowicz,* 2004] under the title 'Excitation of Earth's continuous free oscillations by atmosphere-ocean-seafloor coupling,' and also includes supplementary online material published at the magazine's website (sections 2.7-2.8)

Summary

The Earth undergoes continuous oscillations, and free oscillation peaks have been consistently identified in seismic records in the frequency range 2-7 mHz [*Suda et al.,* 1998; *Tanimoto et al.,* 1998], on days without significant earthquakes. The level of daily excitation of this 'hum' is equivalent to that of magnitude 5.75 and 6.0 earthquakes [*Tanimoto et al.,* 1998; *Ekström,* 2001], which cannot be explained by summing

the contributions of small earthquakes [*Suda et al.,* 1998; *Tanimoto and Um,* 1999]. As slow or silent earthquakes have been ruled out as a source for the hum [*Ekström,* 2001] (except in a few isolated cases [*Beroza and Jordan,* 1990]), turbulent motions in the atmosphere or processes in the oceans have been invoked [*Kobayashi and Nishida,* 1998; *Tanimoto and Um,* 1999; *Watada and Masters*, 2001; *Fukao et al.,* 2002] as the excitation mechanism. We have developed an array-based method to detect and locate sources of the excitation of the hum. Our results demonstrate that the Earth's hum originates mainly in the northern Pacific Ocean during Northern Hemisphere winter, and in the Southern oceans during Southern Hemisphere winter. We conclude that the Earth's hum is generated by the interaction between atmosphere, ocean and sea floor, probably through the conversion of storm energy to oceanic infragravity waves that interact with seafloor topography

2.1 Introduction

Elucidating the physical mechanism responsible for the continuous oscillations represents an intriguing scientific challenge. The source(s) should be close to the Earth's surface, as the fundamental mode appears to be preferentially excited. One proposed mechanism relates the observed oscillations to random excitation by turbulent motions in the atmosphere [*Kobayashi and Nishida,* 1998; *Tanimoto and Um,* 1999; *Fukao et al.,* 2002]. Amplitude levels and frequency dependence estimated stochastically, and constrained by actual barometer readings, are in agreement with the observed continuous oscillation levels. Also in support of this interpretation, seasonal variations in the level of energy present in the continuous oscillations have a six-month periodicity, with maxima in January and July corresponding to winter in Northern and Southern hemispheres respectively [*Ekström,* 2001], correlated with maxima in average atmospheric pressure variations. On the other hand, *Nishida and Kobayashi* [1999]

proposed that the source might be distributed over the entire surface of the Earth. The fact that the background mode signal can be brought out even more clearly by correcting the observed spectra for signal correlated with local barograph recordings provides further evidence for the non-local character of the excitation process [*Roult and Crawford* 2000]. An alternative potential source of excitation of the 'hum' could be in the oceans, resulting from interaction between wind and ocean waves. Such an interpretation is supported by the similarity of the shape of ocean-bottom pressure spectra and ground-motion noise spectra [*Watada and Masters*, 2001].

In order to make further progress on this issue, it is important to determine whether the excitation source is indeed distributed over most of the Earth, or whether most of it occurs either in the oceans or on land. The approaches used so far, based on the computation of spectra, or the correlation of signals across full great-circle paths [*Ekström,* 2001], allow the detection but not the location of the sources. The latter must be addressed using a propagating wave methodology.

2.2 Results and discussion

We have developed an array-based method to detect and locate sources of very-long-period surface wave energy, using the dispersive properties of Rayleigh waves [*Rhie and Romanowicz*, 2002]. The use of surface waves to detect and locate earthquakes was proposed many decades ago [*von Seggern,* 1972]. Generally moderate size events and relatively short periods (that is 20-100 s) have been considered [*Rouland et al.,* 1992]. Array methods have been developed and applied widely for detection and analysis of body waves in the azimuth-slowness domain [*Rost and Thomas*, 2002], and for the analysis of sources of microseisms [*Friedrich et al.*, 1998; *Schulte-Pelkum et al.*, 2004]. Recently, Ekström *et al.* [2003] developed a stacking technique based on a global network of $\sim$ 100 long-period seismic stations and, in the period band 35-150

s, they detected many glacial earthquakes depleted in high-frequency energy. On the other hand, *Nishida et al.* [2002] showed that the vertical seismic background noise in the entire pass-band from 2 to 20 mHz is dominated by globally propagating Rayleigh waves. Here we utilize the dispersive properties of mantle Rayleigh waves in the period band 150-500 s across two regional networks of very broadband seismometers, one in Japan (F-net) and the other in California (BDSN). Our analysis is centered around a period of 240 s, where the dispersion of Rayleigh waves presents a characteristic Airy phase. For each array, time domain seismograms are stacked after correcting for dispersion and attenuation across the array, assuming plane wave propagation from an arbitrary azimuth (see section 2.3, and Figure 2.1). We first exercised and tested the array sensitivity on real earthquake data, for the three-year period 2000-02.

In order to attempt detection and location of non-earthquake sources of surface wave energy, it is necessary to first remove all intervals of time affected by earthquakes of moment magnitude $M_w > 5.5$ (see section 2.4), whereas smaller earthquakes do not significantly contribute to Rayleigh wave energy above 150 s [*Suda et al.,* 1998; *Tanimoto et al.,* 1998]. Many detections of Rayleigh wave energy are observed on quiet days, unrelated to earthquakes (see, for example, Figures 2.2a, 2.2b, 2.2c, and 2.2d). Maximum stack amplitudes for BDSN and F-net correlate strongly as a function of time, indicating that the source of the Rayleigh wave 'noise' is common for the two arrays (Figure 2.2e). Moreover, inspection of the Rayleigh wave energy distribution as a function of time and direction of arrival reveals striking spatial coherency. Because the array shape can introduce artificial distortions in the amplitude patterns as a function of azimuth, we first consider a component of the energy which is independent of the array response. For each day and for each array, we compute the Fourier spectrum of the stack amplitude as a function of azimuth and compare it to that of the array response.

The distribution of stack amplitudes as a function of time and back azimuth has a strong 'degree one' harmonic component in azimuth. This cannot be due to the array response which is dominated by even harmonics in azimuth, and indicates a

true preferential direction of arrival. For each array, the direction of the maximum in degree one is stable at the seasonal scale; it is consistently different in (Northern Hemisphere) winter and summer (Figures 2.3a and 2.3b). Then for each array, we compute the amplitude of the stack as a function of azimuth, averaged over summer and winter separately, calculate its Fourier spectrum and extract the degree one component (Figures 2.3c and 2.3d) as well as the azimuth of the corresponding maximum. By combining the directions of maximum stack amplitude obtained for each array, in summer and winter respectively, and back-projecting along the corresponding great-circle paths, we infer that the sources locate preferentially in the northern Pacific Ocean in the winter (Figure 2.4a), and in the southern oceans in the summer (Figure 2.4b). These locations corresponding to regions of maximum storm activity in the northern and southern winters respectively, as indicated by the comparison with significant wave height maps (Figures 2.4c and 2.4d).

The degree one distribution only gives a first-order idea of the preferential direction of arrival at each array. More insight is obtained by determining how a distribution of sources, initially uniform in azimuth, needs to be modified to fit the original observed seasonal patterns. Such an analysis (see section 2.6 and Figures 2.5 and 2.6) confirms that, in the winter, much of the energy originates in the North Pacific Ocean, while in the summer, the activity shifts to the southern seas. We have also verified (through forward modeling experiments described in detail in section 2.8) that distributions of sources over continental areas are not compatible with the observations at both arrays simultaneously, whereas even a rough preferential distribution of sources in the northern Pacific fits the winter patterns for both arrays rather well. In the summer, we require a distribution of sources in the southern oceans, with preferential contributions from parts of the south Pacific and south Atlantic. Although a precise location of the sources would necessitate a more precise knowledge of the array response, our experiments clearly show that neither a uniform distribution of sources around the globe nor a distribution over continents are compatible with the data, in contrast to a distribution alternating between northern and southern oceans in winter and summer, respectively.

Finally, we considered a particular day, 31 January 2000, which corresponds to a maximum in the amplitude of the stacks for both F-net and BDSN (Figure 2.2e). We computed the stack amplitude as a function of azimuth over this 24 h interval at each array (Figures 2.2a and 2.2b), and noted that the maximum average stack amplitude over this time interval points to a well defined direction of arrival, which is in general agreement with that found on other winter days. We confirm that the energy maxima correspond to the arrival of Rayleigh waves (Figures 2.2c and 2.2d) by searching for the phase velocity and azimuth which give the maximum stack amplitude, averaged over that day. To analyze the time/space distribution of these sources, we conducted a parameter search in and around the north Pacific region. We find that the sources are distributed in space and time over a region spanning several thousand km^2, and with a correlation time of the order of $\sim$ 6 h (Figure 2.7).

Our results show that the ocean plays a key role in the excitation of the Earth's 'hum'. Part of the energy contained in ocean waves (generated by significant storms over the mid-latitude oceans) is converted to elastic waves. Infragravity waves are obvious candidates for the energy transfer from storms, through the ocean, to the sea floor [*Tanimoto,* 2003]. They are indirectly driven by winds over ocean basins, and are probably generated in shallow water through conversion from short-period ocean waves by nonlinear processes [*Webb et al.*, 1991]. Some of the energy leaks out and propagates as free waves into the ocean basins [*Munk et al.*, 1964]. Hydrodynamic filtering may play a role in determining which infragravity waves interact with the deep ocean floor [*Webb and Crawford*, 1999], with short-period waves generated nearer to the coasts. The mechanism of generation of elastic waves probably involves focusing of infragravity waves by the concave shape of the continental boundaries towards the deep ocean, as well as by topography of the deep ocean floor. The efficiency with which long-period Rayleigh waves are generated in particular areas of the ocean basins must thus depend on the depth of the ocean floor, the shape of the continental shelves bounding the ocean basin, as well as the strength and persistence of storms. Notably, even though individual storms can be as strong over the north Atlantic as they are over the north Pacific, only the latter is detected in our data, which is in agreement

with differences of 20-30 dB in pressure noise between these oceans in the infragravity wave band [*Webb*, 1998].

More detailed understanding of source distribution in space and time and its relation to ocean storms will require expanding the observational time windows by precisely removing signals due to earthquakes through a forward modeling approach, as is feasible at elastic models of the mantle [*Ekström et al.,* 1997] as well as further analysis of wave height information. Also, the deployment of high-quality very broadband seismometers in the Southern Hemisphere (for example, across Australia) would help to characterize the source distribution better. Finally, we note that multi-disciplinary long-term ocean observatories spanning the entire water column (from sea floor to sea surface), such as are being proposed in the framework of the OOI (Ocean Observatories Initiative) program, should acquire data that would help to make progress in our understanding of this complex energy transfer process.

2.3 Array detection and location

We consider two regional networks of very broadband seismic stations in the Northern Hemisphere (1) the Berkeley Digital Seismic Network (BDSN) in northern California, augmented by several stations of the TERRAscope network in southern California; and (2) the F-net in Japan. BDSN and F-net stations are equipped with very broadband STS-1 seismometers [*Wielandt and Streckeisen*, 1982].

We pre-processed vertical component time series by removing glitches and tides and deconvolving the instrument response to velocity. We then filter the data using either a gaussian filter centered at 240 s, or, in some experiments, a band-pass filter between 150 and 500 s (Figures 2.7 and 2.8g). Two approximations are considered. We ignore the effect of lateral heterogeneity on the propagation of mantle Rayleigh waves, and

we assume that they propagate across an array as plane waves (Figure 2.1), with a well defined incident azimuth (except in Figure 2.7, where the plane wave approximation is not used). The whole year is divided into 1-day intervals. For each time interval, and for each increment in back azimuth of 5°, we align the waveforms from 10 or more stations using the center of the array as reference point, and correct for dispersion and attenuation of the fundamental mode Rayleigh wave across the array, according to the reference PREM velocity model [*Dziewonski and Anderson,* 1981]. We stack the corrected waveforms using a phase weighted stack [*Schimmel and Paulssen,* 1997], which reduces uncorrelated noise, as compared to straight stacking (Figure 2.9). We tested the sensitivity of our array stacking for the detection of known earthquakes (Figures 2.9 and 2.10). Associating the detections obtained at three different arrays (including an array in western Europe) leads to an earthquake location method (see section 2.9), which works well at the magnitude 6 level, as we were able to detect and locate 73% of magnitude 6 and larger earthquakes without any optimization of the method.

2.4 Removal of intervals of time contaminated by earthquakes

We removed intervals of variable length, according to the size of the earthquake, for all earthquake of magnitude $M_w > 5.5$. We first rejected any day within which an earthquake $M_w > 6$ has occurred. We then defined a time span for additional rejection, using an exponential function constrained to be 3 days for $M_w \geq 7$, and 1.5 days for $M_w \geq 6$, starting at the origin time of the event. We also rejected a window before the earthquake, of length 10 % of the length rejected following the origin time, to account for contamination due to the non-causal low-frequency filtering of the data. There are only a few 'quiet' windows left in one year, corresponding to $\sim$ 18 % of the

time in 2000. Similar results are obtained for 2001.

2.5 Detection of Rayleigh waves during 'quiet' intervals

The same approach used for detecting earthquakes is applied during quiet intervals. Figure 2.8 shows an example for a specific interval of time during day 2000/01/31, the same day as shown in Figure 2.2. Alignment of traces is improved after taking into account Rayleigh wave dispersion in a specific azimuth range (Figures 2.8b and 2.8c). The corresponding stack amplitude has a maximum which is localized in time and azimuth (Figure 2.8a). The detected energy indeed corresponding to Rayleigh waves, as verified by a parameter search in azimuth and phase velocity space (Figure 2.8f) as well as in period versus phase velocity space (Figure 2.8g).

2.6 Removal of array response

Because the arrays considered are not completely symmetric, it is important to verify that biases due to the non-uniform array response in azimuth are not dominating the results. For this purpose, we have estimated the array response by randomly generating many synthetic seismograms and distributing them uniformly in azimuth. This procedure is described in detail in section 2.7.

The amplitude of the array response cannot be directly compared to that of the observed patterns, so that we cannot completely remove it from the observed stack

amplitudes. However, the array response has almost perfect 180 ° symmetry, with amplitude lobes corresponding to the elongated direction of the array, as expected. The corresponding Fourier spectra in azimuth are dominated by even degrees (particularly degree two), and have practically no degree one (of a similar size as degree two, Figures 2.11e and 2.11f), which defines a specific direction of maximum amplitude, different in the summer from in the winter (Figure 2.3). By conservatively analyzing only the degree one component in the data, we guarantee that there is no contamination by the array response, while losing some directional resolution contained in the higher-degree azimuthal terms. Further experiments confirm that the degree one analysis indeed gives a good indication of the spatial distribution of source energy and its seasonal variations.

2.7 Array response

In order to determine the distortions in the amplitude patterns as a function of back-azimuth due to the array shape, we compute synthetic stacks corresponding to a uniform distribution of sources of Rayleigh waves around the globe. It is not possible to generate completely accurate synthetic waveforms for the hum, because the source mechanism is not known at present. However, several previous studies help us to define the properties of the waveforms: (1) waveforms mainly consist of fundamental mode Rayleigh waves; (2) mean energy over long time spans should be constant as a function of direction of arrival, if sources are completely random in time and space. Our synthetics are designed to satisfy these two conditions. We calculate 16 reference Rayleigh wave synthetics which correspond to sources at distances of 20 to 170° from the center of the array (i.e., every 10°), an arbitrary moment tensor solution and shallow focal depth (15km). Construction of random source synthetics then involves three steps: 1) we randomly choose 1 out of the 16 synthetics and randomly perturb

the source amplitude and source phase; 2) we randomly distribute the origin time, over an interval of 24 hours, of 4000 such synthetics. Each 24 hour waveform thus obtained is then assigned a specific direction in azimuth and then we repeat steps 1) and 2) for every 10° step in azimuth; 3) For each station in the array, we sum the 36 traces thus obtained, after correcting each for Rayleigh wave dispersion with respect to the center of the array. We then perform the array stacking procedure in the same way as for real data and obtain a distribution of amplitude as a function of azimuth. Ten realizations of this experiment are then averaged to obtain the array response shape shown in Figures 2.11c and 2.11d, which can be compared to the seasonal distribution of amplitudes (Figures 2.11a and 2.11b). The distributions shown in Figures 2.5 and 2.6 are obtained by modifying the uniformly distributed source amplitudes in particular azimuth ranges.

2.8 Generation of regional source distributions

For the synthetic calculations shown in Figures 2.12 and 2.13, we adopted a more computationally efficient approach. We first considered 642 points uniformly distributed over the sphere, using a sphere triangulation algorithm. For a one day period, and for each point we considered 30 sources with randomly distributed origin times. Source amplitudes and phases were obtained by adding a random perturbation to a reference source model, as was done in the array response analysis described above. Source amplitudes are constant in all azimuths (thus ignoring any possible non-uniform radiation pattern). Rayleigh waves are propagated to each station of each array, following which they are stacked using the same procedure as for real data, and the stacks are averaged over one day. To obtain a preferential distribution of sources in a particular region of the globe, the source amplitudes for the points located within that region are increased by a factor ranging between 100% and 400%, depending on the region,

and so as to obtain an optimal fit to the data. To save computational time, we only considered a relatively sparse distribution of sources and a realization of the experiment over only one day, whereas 10 days are required to obtain a completely stable pattern. However, we verified that the fluctuations between the realizations do not impact the key features of each regional distribution.

2.9 Locating large known earthquakes using array stacking

To demonstrate the power of the array stacking method to detect and locate long period seismic energy sources, we tried to locate large known earthquakes ($M_w \geq 6$). We consider vertical component velocity seismograms at three regional arrays. The gaussian filter with the center period of 240 s is applied to velocity seismograms. In this application, we added one more regional array in Germany (GRSN), which was not included in the study on the hum because of the narrow and shorter frequency band width of the seismometers compared to two arrays in California (BDSN) and Japan (F-net). Our location method consists of three steps: 1) Pick all peaks with maximum amplitude function (MAF, defined in Figure 2.10) larger than 1.0×10^{-9} m/s and save arrival time and back azimuth information of each peak for all arrays. A stack amplitude threshold of 1.0×10^{-9} m/s is small enough to include all Rayleigh wave arrivals at all three arrays due to M 6 level earthquakes. 2) Select most likely peaks associated with known events for all three arrays. The "detection" is declared when the differences in time and back azimuth between observed and theoretical arrival times and back azimuths for all three arrays are less than 500 s and 30°, respectively. We detected 73% of all $M_w \geq 6$ listed in the Harvard CMT catalog for 3 years (2000-2002) [*Dziewonski and Anderson,* 1981]. 3) Apply a grid search method to locate them independent of the catalog. The grid search method, which utilizes travel

time and back azimuth information of energy arrivals, has been used for earthquake location within regional arrays [*Dreger et al.,* 1998; *Uhrhammer et al.,* 2001] and we just modified the misfit function to work with our global scale application. The core of the grid search method is how sensitive the misfit function is. In this application, the misfit function is defined by

$$M = \frac{1}{N}\sum_{i=1}^{N}\sqrt{(1-\lambda)(\delta r_i)^2 + \lambda(R\delta a_i)^2}, \tag{2.1}$$

where

$$\delta r_i = |t_{oi} - t_{pi}|\, U, \tag{2.2}$$

$$t_{pi} = \frac{R\Delta_i}{U}, \tag{2.3}$$

$$t_{oi} = t_i - \frac{1}{N}\sum_{i=1}^{N}(t_i - t_{pi}), \tag{2.4}$$

and

$$\delta a_i = \cos^{-1}(\cos\Delta_i \cos\Delta_i + \sin\Delta_i \sin\Delta_i \cos\delta\phi_i). \tag{2.5}$$

Where M is the misfit function as a function of trial source locations, N is the number of arrays, and λ is a relative weighting factor of travel time and back azimuth residuals. The travel time residual (δr_i) is the uncertainty in distance (km) due to time differences between observed (t_{oi}) and predicted (t_{pi}) travel times at i^{th} array. Here the predicted travel time is defined by the division of the epicentral distance ($R\Delta_i$) from the possible source location to the array by the group velocity (U). However,

to compute the observed travel time (t_{oi}), we need to determine the origin time of the possible event. The origin time is defined by an average of time differences between arrival times (t_i) and predicted travel times. The final travel time residuals are computed by multiplication of time differences between observed and predicted travel times and the group velocity to provide a straightforward comparison to the back azimuth residuals. The back azimuth residual ($R\delta a_i$) is the uncertainty in distance due to back azimuth measurement and is defined by using spherical trigonometry. Here Δ_i is arc distance between the trial location and i^{th} array in radians, $\delta\phi_i$ is the difference in back azimuth between measured and predicted back azimuths for the trial location (see Figure 2.14 and R is the radius of the Earth in km. The misfit function is used in step 2 and 3. In step 2, the misfit function is used to select the most likely peak associated with known event for each array. In this case, the misfit functions for three arrays are computed separately (i.e., $N = 1$) for the known epicenter and origin time. In step 3, the misfit function is used to locate events and we defined grids for trial locations. To save computation time, we defined two different grids. The first grid is defined by using 3^{rd} order spherical splines. We search 162 points over the globe with nearly constant spacing and find the point with the minimum misfit value. The second grid is defined within 15° around the solution from the first grid, with finer spacing. By tuning a weighting factor, we were able to locate all detected events within 30° around the known epicenters (Figure 2.15). In many cases where we failed to detect a catalogued event, the reason was contamination by another large event. Further optimization of our method (in particular taking into account 3D structure) would likely lead to even higher success rates.

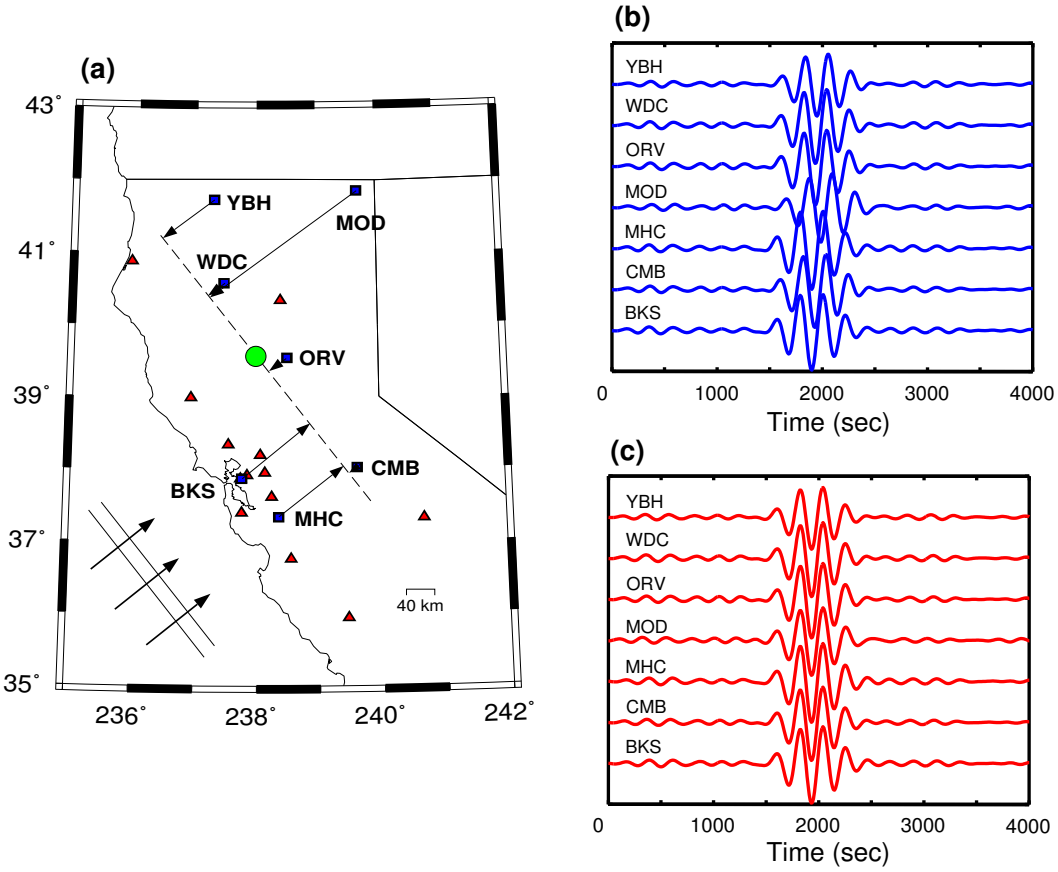

Figure 2.1: Illustration of stacking procedure. (a) Schematic diagram showing how waveforms are mapped to the center of an array assuming plane wave propagation. Symbols indicate quiet BDSN stations used in this study (blue squares), other BDSN stations (red triangles) and center of the array (green solid circle). In practice, we also use several additional stations from the TERRAscope network in southern California. (b) Vertical velocity waveforms generated by the Jan. 8, 2000 M_w 7.2 event at 7 quiet BDSN stations, filtered using a Gaussian filter centered at 240 s. (c) Same as b after back-projecting the waveforms to the center of the array, correcting for dispersion and attenuation using the reference PREM model, and the known back-azimuth of the event.

Figure 2.2: Analysis of detections for 31 January 2000. (a) Amplitude of F-net stacks as a function of time and back azimuth. Small panel on right shows mean amplitude, as a function of back azimuth. A gaussian filter centered at 240 s has been applied to waveforms before stacking. (b) Same as (a) for BDSN. (c) Mean amplitude plot as a function of phase velocity and back azimuth for F-net, confirming that the observed energy corresponds to Rayleigh wave arrivals. The two vertical white lines indicate the range of phase velocities expected for Rayleigh waves between periods of 200 and 400 s. The theoretical phase velocity at 240 s is 4.85 km/s. Blue arrow indicates the back azimuth of the maximum mean amplitude shown in (a). (d) Same as (c) for BDSN. (e) Mean amplitude of stacks as a function of time for quiet days for BDSN (red) and F-net (blue), for back azimuths of 295° and 65° respectively, in winter and back azimuths 105 ° and 235◦ in summer, normalized to the maximum amplitude for the entire time span. These azimuths correspond to the average direction of maximum amplitude in each season. The correlation coefficient between the two line series is 0.78.

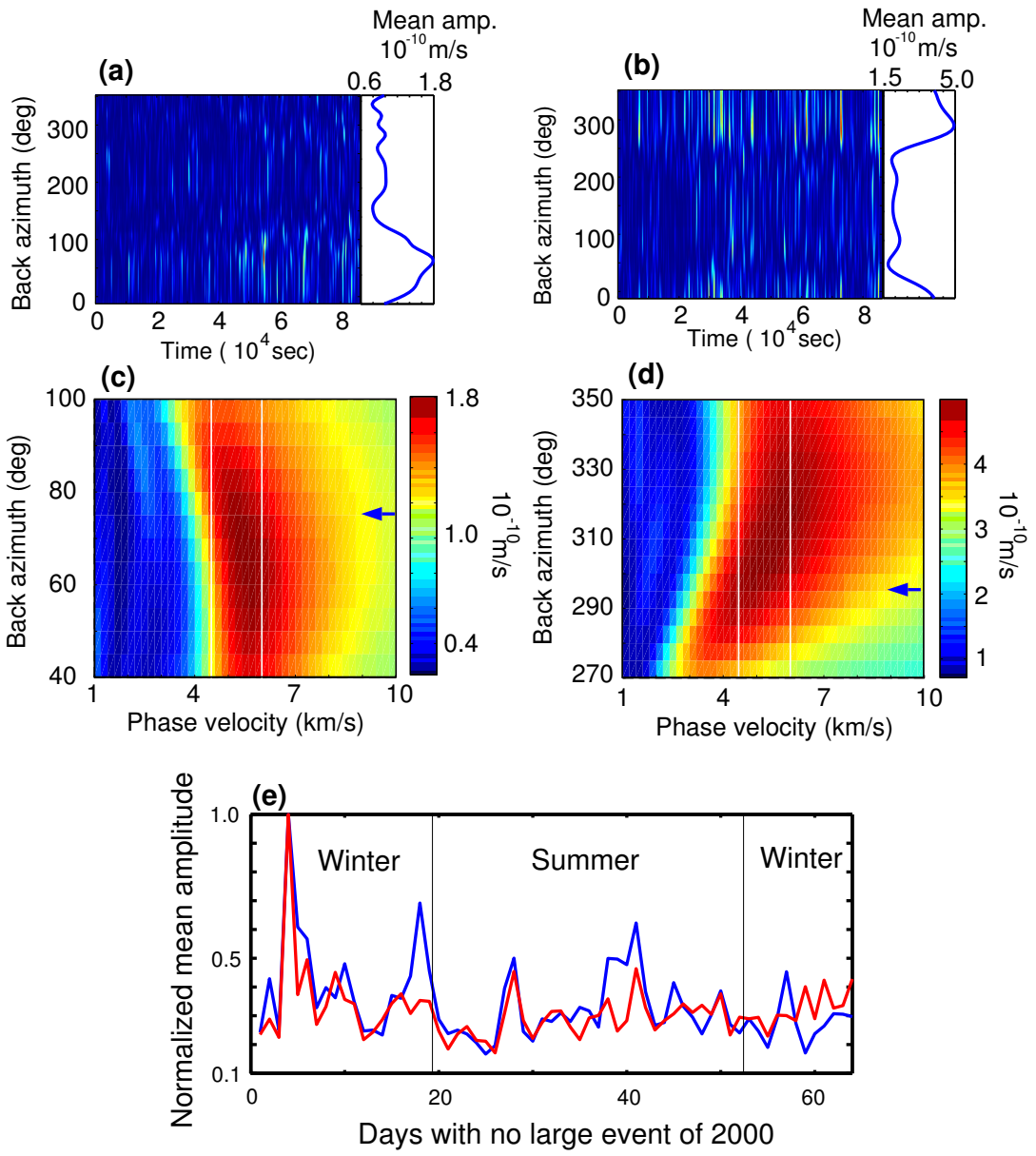

Figure 2.2: continued

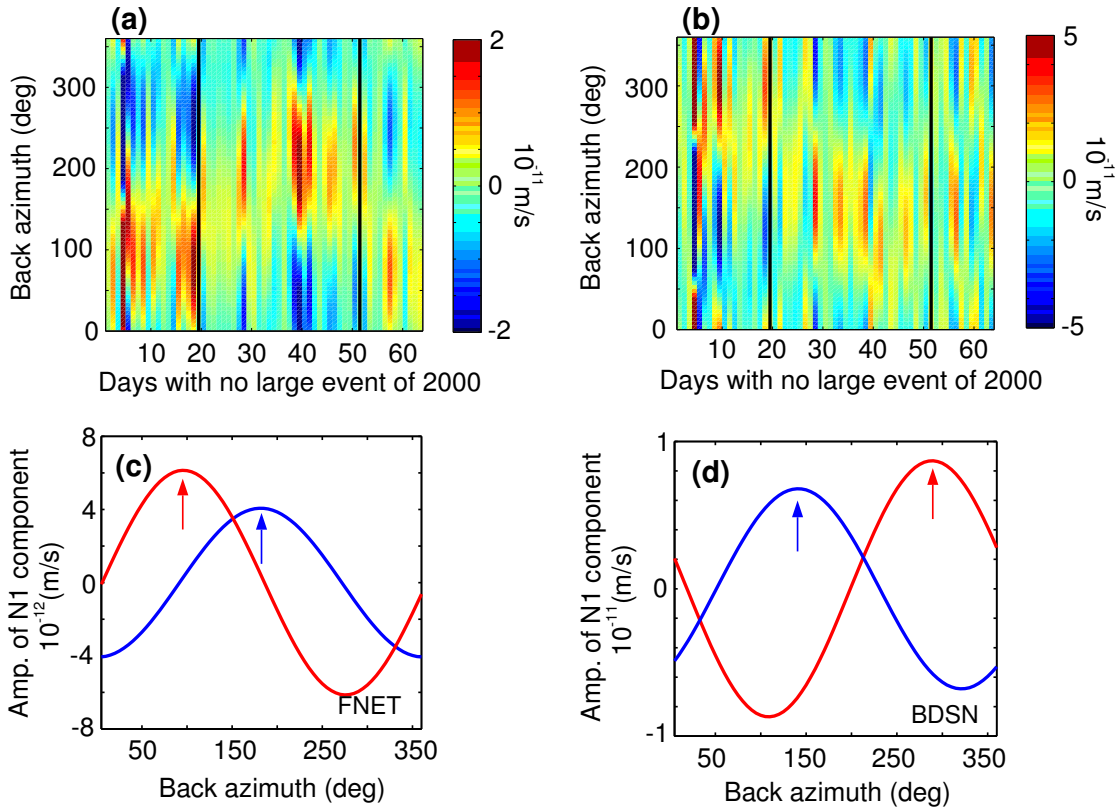

Figure 2.3: Amplitude of degree one as a function of time and back azimuth for the 64 quiet days in 2000. A 'quiet day' contains at least 12 contiguous hours uncontaminated by earthquakes, and only those intervals are considered within each day. (a) Back azimuth corresponding to the maximum in the degree one component of stack amplitude for F-net as a function of time. Black vertical lines separate winter and summer intervals. Winter is defined as January-March, and October-December. (b) Same as (a) for BDSN. (c) Degree one as a function of azimuth for F-net, averaged for the winter (red) and the summer (blue). Arrows point to maxima in back azimuth; the degree one is almost as large as degree two in the data (see, for example, Figure 2.11) and is not contaminated by array response. (d) Same as (c) for BDSN

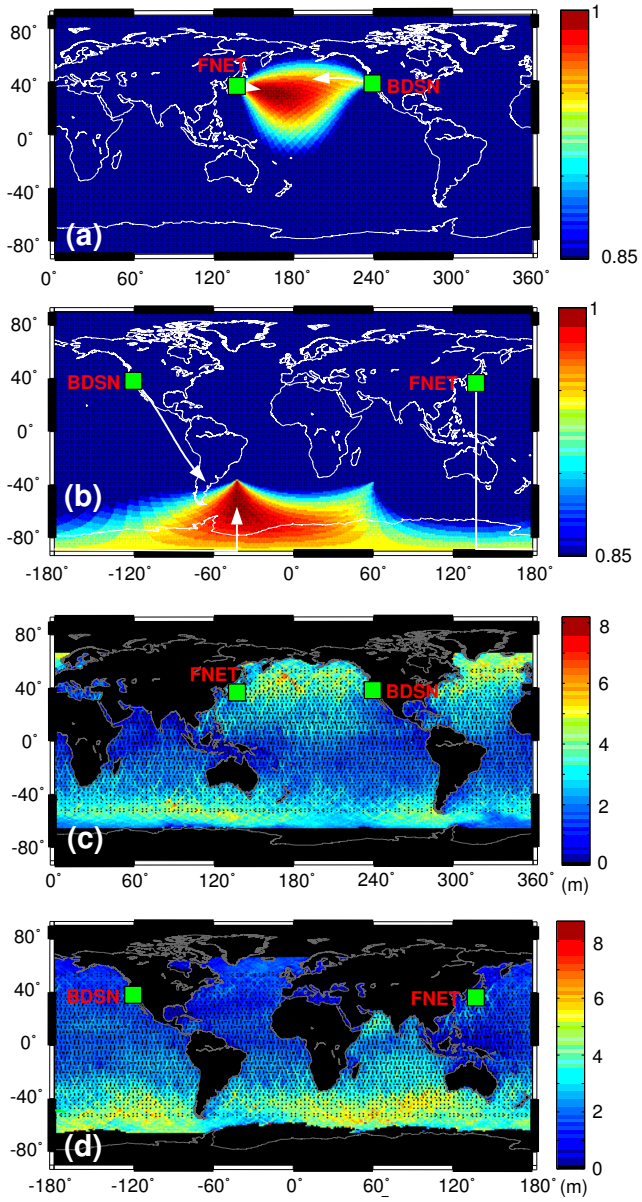

Figure 2.4: Comparison of seasonal variations in the distribution of hum-related noise (degree one only) and significant wave height in the year 2000. (a-b) The directions corresponding to mean amplitudes that are larger than 85% of the maximum are combined for the two arrays in winter (a) and in summer (b) to obtain the region of predominant sources in each season. Arrows indicate the direction of maxima. Both arrays are pointing to the North Pacific Ocean in the winter and the southern oceans in the summer. (c-d) Global distribution of significant wave height, in the winter (c) and in the summer (d), averaged from TOPEX/Poseidon images for the months of January and July 2000, respectively. Black color in (c) and (d) indicates locations with no data.

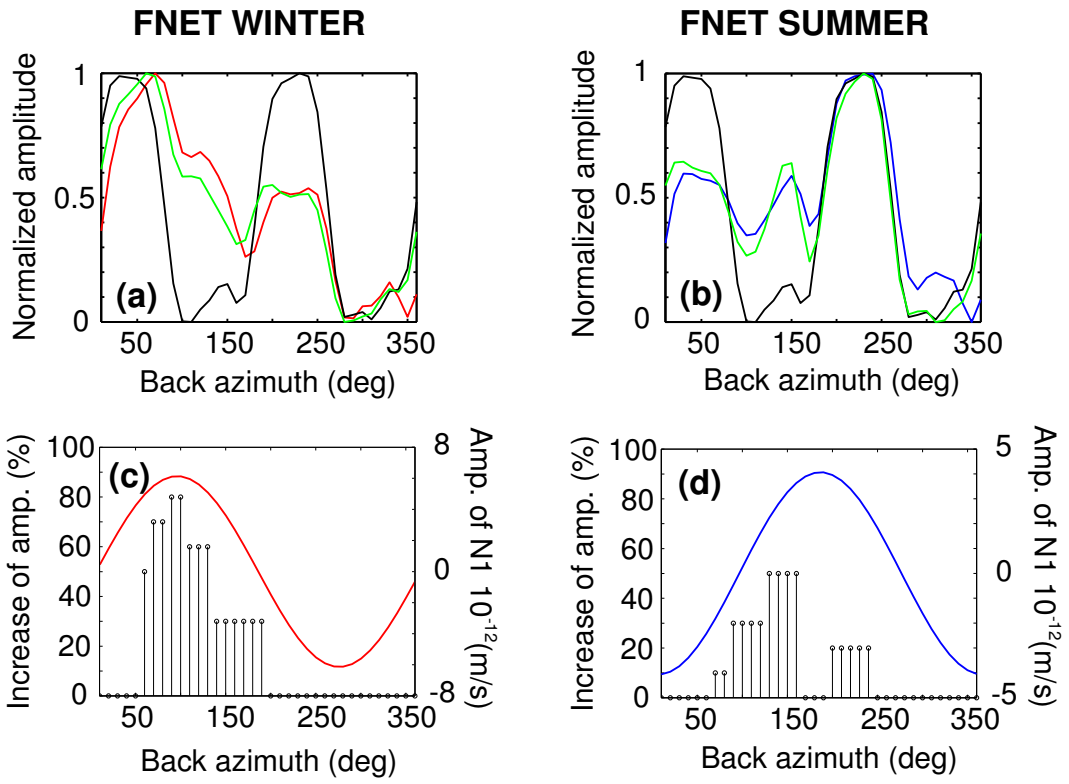

Figure 2.5: Forward modeling of source distribution in azimuth for F-net. (a) Observed (red) and fitted (green) stack amplitude as a function of azimuth, for winter, compared to array response shape (black). All have been normalized to their respective maximum amplitudes. (b) Observed (blue) and fitted (green) stack amplitude as a function of azimuth, for summer. (c) Proportion (in percent) of excess sources as a function of azimuth needed to fit the observed amplitude variations in winter, compared to the corresponding degree 1 in the observed spectrum. (d) Same as (c) for summer.

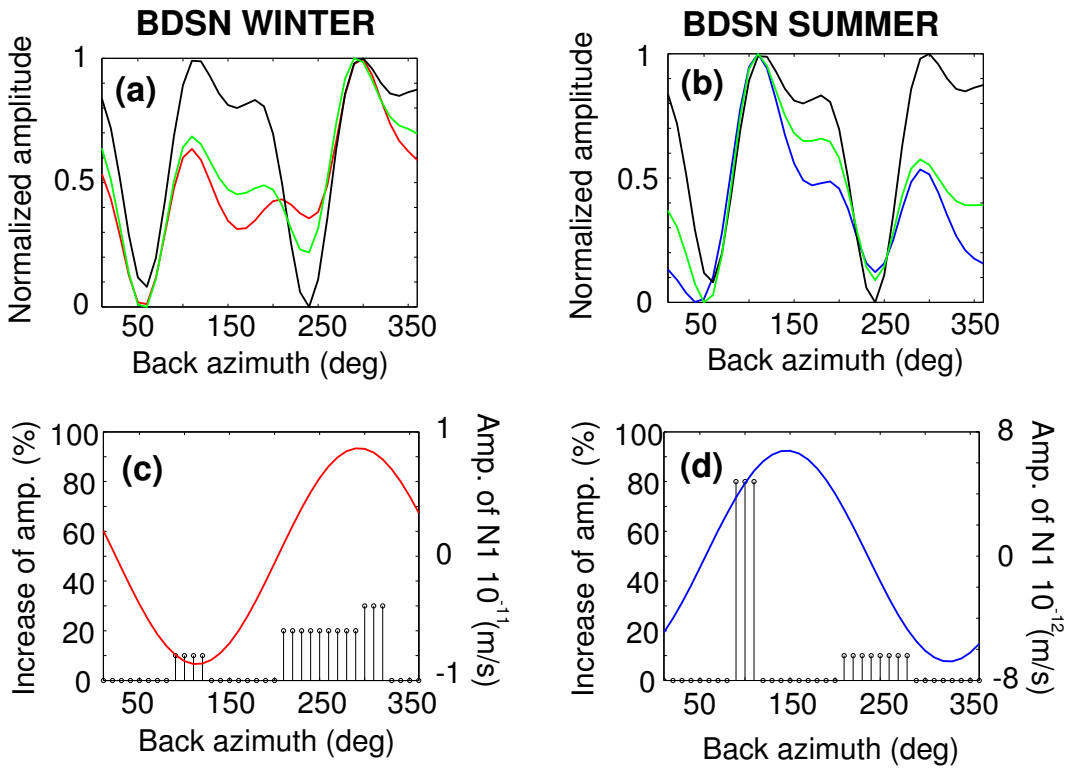

Figure 2.6: Same as Figure 2.5 for BDSN

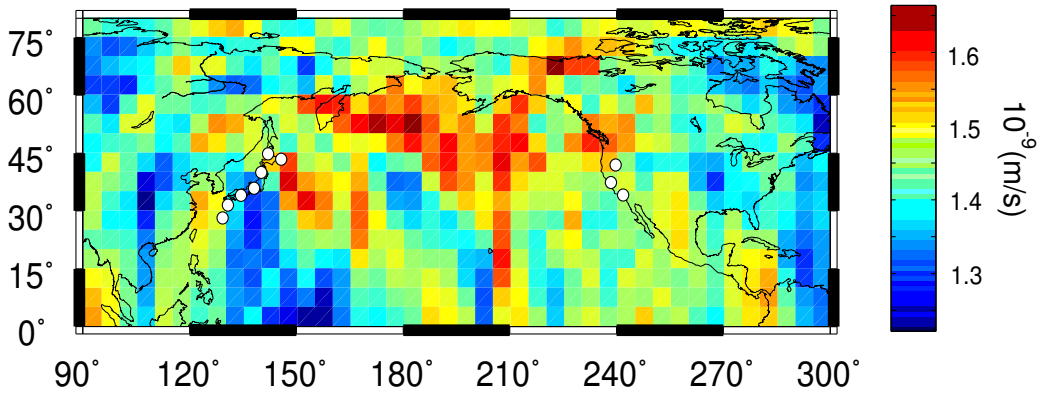

Figure 2.7: Distribution of sources for a 6 h time window on 31 January 2000 (from 14:00 to 20:00 UTC). Maximum amplitudes were averaged over all stations considered (in m/s), back-projected to the center of 5° × 5° blocks, and corrected for the dispersion of Rayleigh waves for each source station path, thereby indicating the distribution of possible source locations. F-net, BDSN (with 3 TERRAscope stations) and 10 European stations (KONO, ARU, BFO, DPC, KIEV, SSB, AQU, VSL, ESK and ISP) are used in this analysis. White dots in Japan and California indicate the areas spanned by the corresponding arrays. Waveforms have been band-pass filtered between 150 and 500 s. Analysis over shorter time windows does not lead to stable results, suggesting a correlation time of several hours and a spatially distributed source. In this analysis, the plane wave approximation is not made, nor are the results biased by the array response.

Figure 2.8: Analysis of a detection during a quiet day (January 31, 2000) on the F-net array. (a) Plot of amplitude (in m/s) of stack as a function of time and azimuth for a 6000 s interval without earthquakes. Waveforms have been filtered with a Gaussian filter centered at 240 s. Single station waveforms before and after correction for dispersion across the array at the back-azimuth of the maximum in (a) are shown in (b) and (c) respectively. Red lines show the time of best alignment. Corresponding stacks are shown in (d) before alignment and (e) after alignment. Note that the amplitude of the maximum is of the same order of magnitude as for the M5.8 event shown in Figure 2.9. (f) Search for optimal phase velocity for dispersion correction before stacking, as a function of azimuth, for the time period corresponding to the maximum in the stack (54,500-55,500 sec). White lines indicate expected range of phase velocities for Rayleigh waves. (g) Parameter search for phase velocity as a function of period for the same interval of time as in (f). Here, the data have been bandpass filtered between 150 and 500 s. The white line indicates the theoretical Rayleigh wave dispersion curve for the PREM model. For periods longer than 300 s, phase velocity is not well resolved, as expected. The results of the parameter searches in (f) and (g) confirm that the observed energy in the stacks corresponds to Rayleigh waves.

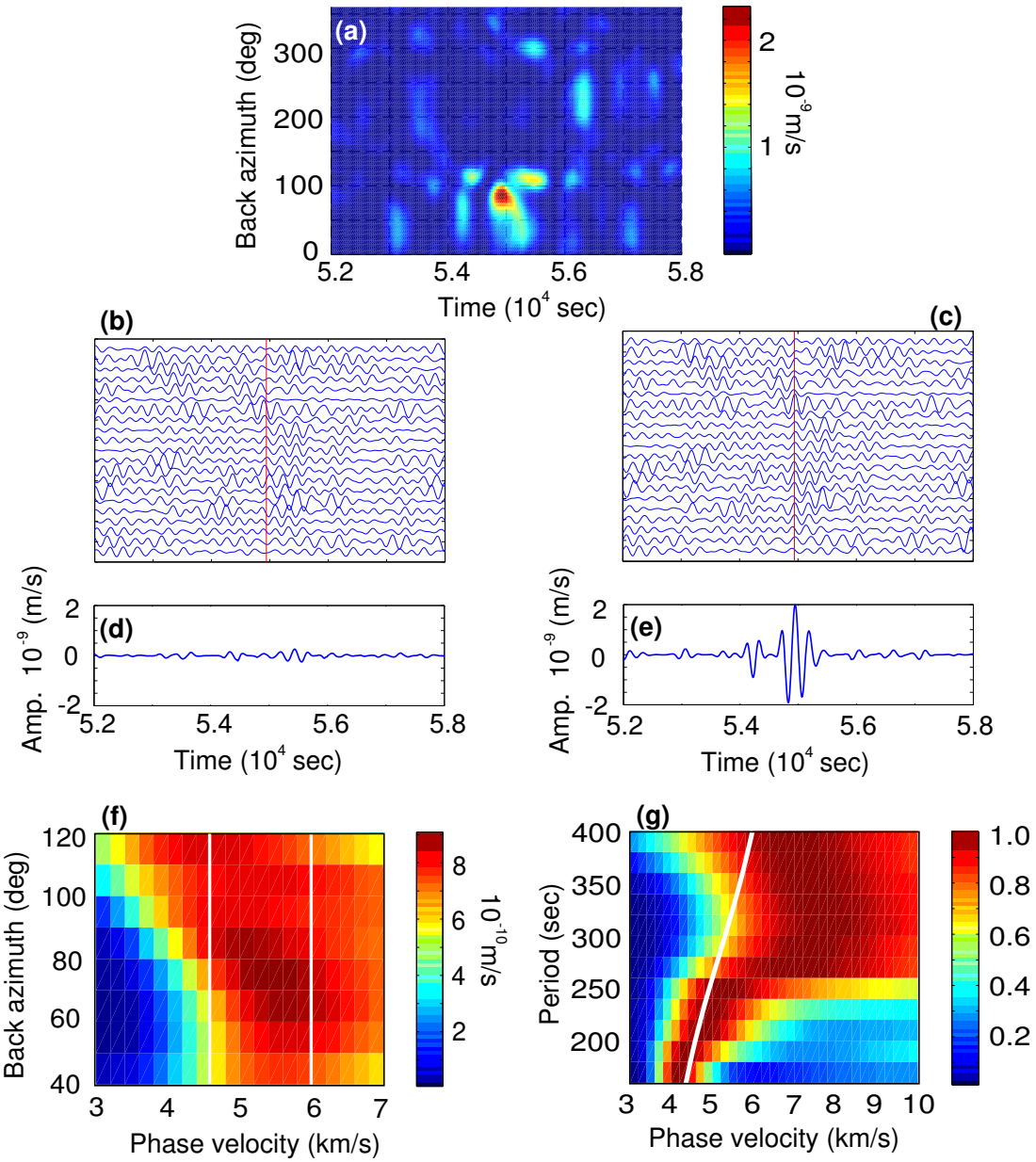

Figure 2.8: continued

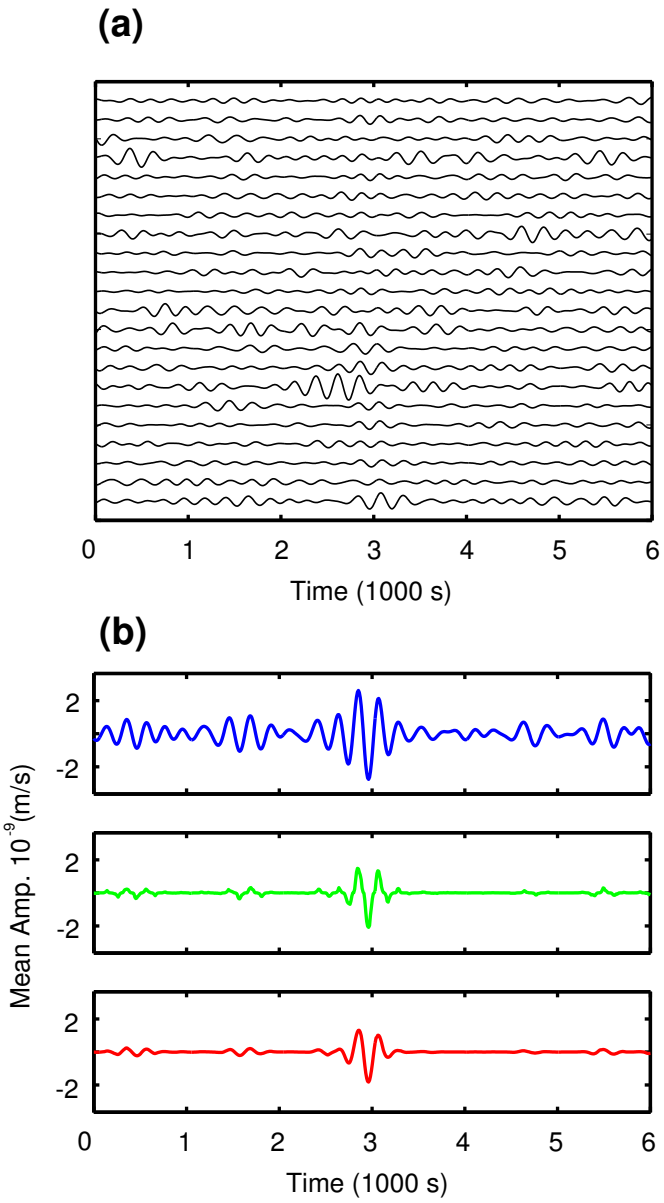

Figure 2.9: (a) Gaussian filtered waveforms (with center period 240 s) recorded at F-net stations after back-projecting to center of the array. Weak surface wave energy corresponding to the January 2, 2000 M_w 5.8 earthquake (12:58:45.2UTC; 51.54N 175.50W, distance: 36.31°) arrives around 3000 sec. (b) Comparison between three different stacking methods: straight summation and mean (blue); 3rd root stacking method (green); phase weighted stack (red). By taking the envelope of every stack for all possible azimuths, we obtain the amplitude function as a function of time and back azimuth (Figure 2.10).

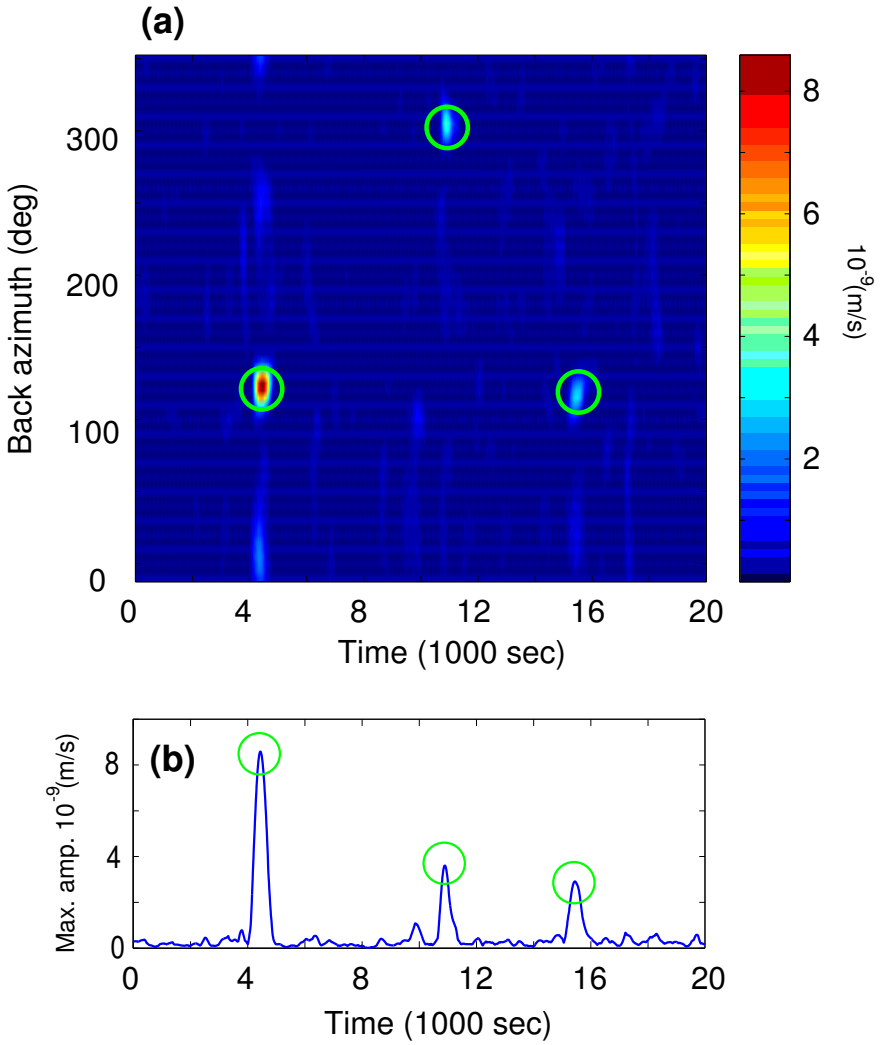

Figure 2.10: Amplitude of array stack as a function of back azimuth and time for a day with an earthquake. We pick the back-azimuth which corresponds to the maximum amplitude of the stack for the time interval considered, and define two functions of time: the "back-azimuth" function, and the corresponding "maximum amplitude" function (MAF). If that maximum exceeds a preset threshold, a detection is declared as illustrated in this example. (a) Plot of stack amplitude as a function of time and back azimuth at F-net. Green circles indicate significant amplitude in the time period considered. They correspond to R1, R2 and R3 for the January 2, 2000 M_w 5.7 earthquake (15:16:34.8UTC; 21.24S 173.30W, distance 74.17°). (b) The corresponding maximum amplitude function as a function of time, highlighting the time of arrival of R1, R2 and R3.

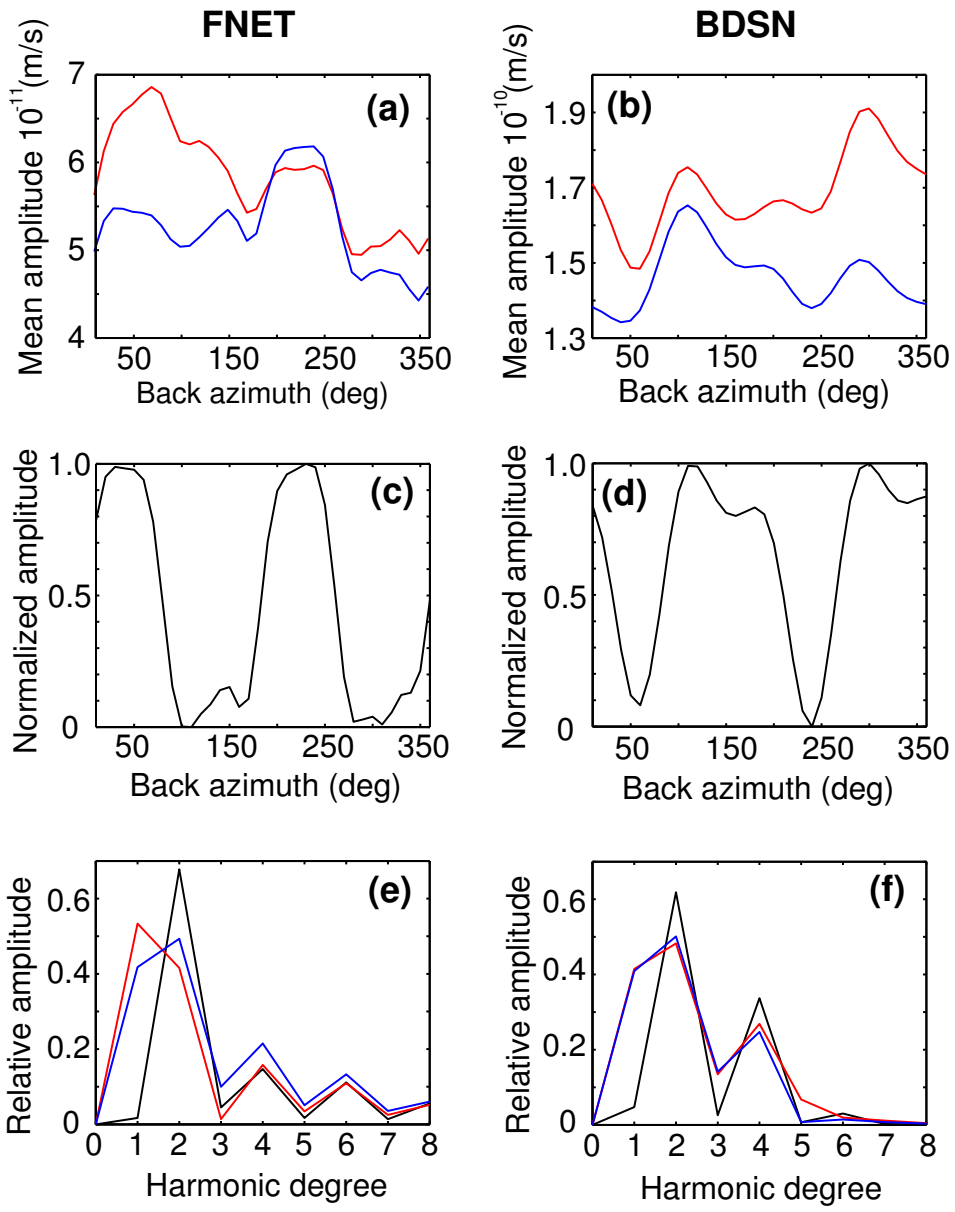

Figure 2.11: Analysis of array response. (a) Distribution of observed stack amplitude as a function of azimuth, averaged over winter (red) and summer (blue) for F-net. (b) Same as (a) for BDSN. (c) Normalized Array response for F-net computed as described in section 2.6. (d) Same as (c) for BDSN. (e) Fourier spectrum in azimuth for winter (red), summer (blue) and array response (black) for F-net. Amplitudes are normalized by total power of spectrum. (f) Same as (e) for BDSN.

Figure 2.12: Results of forward modeling of stack amplitudes as a function of azimuth, for F-net (left) and BDSN (right) for a distribution of sources concentrated over different continents. Starting from a uniform distribution over the entire globe (black), the amplitude of sources of fundamental mode Rayleigh waves is increased by 100 % over each region considered, successively. Model predictions (green) are compared with the predictions for a globally uniform distribution (black) and the observed distributions for winter (red) and summer (blue). Arrows point to the maxima in each distribution. a and b: sources in Eurasia (ER). This region is defined as spanning longitudes: 0°E-135°E for the latitude range 30°N-70°N, and longitudes 45°E-120°E for the latitude range 15oN-30oN. c and d: Africa (AF). This region is defined as spanning longitudes 15°W to 45°E for the latitude range 0°N-30°N, and longitudes 15°E-45°E for the latitude range 30oS-0oS. e and f: North America (NAM). This region is defined as spanning longitudes 125°W-70°W and latitudes 30°N-70°N. g and h: South America (SAM). This region is defined as spanning longitudes 80°W-50°W for the latitude range 0°N-12°N, longitudes 80°W-35°W for the latitude range 15°S-0°S, and longitudes 75°W-50°W for the latitude range 45°S-15°S. We note that, for each of the continental regions, when the predicted maximum amplitude is compatible with one of the observed distributions (winter or summer) for one of the arrays, it is not compatible for the other array, ruling this out as a possible solution to explain the observed patterns. We also verified that the combination of several, or all continental areas does not predict distributions compatible with both arrays simultaneously.

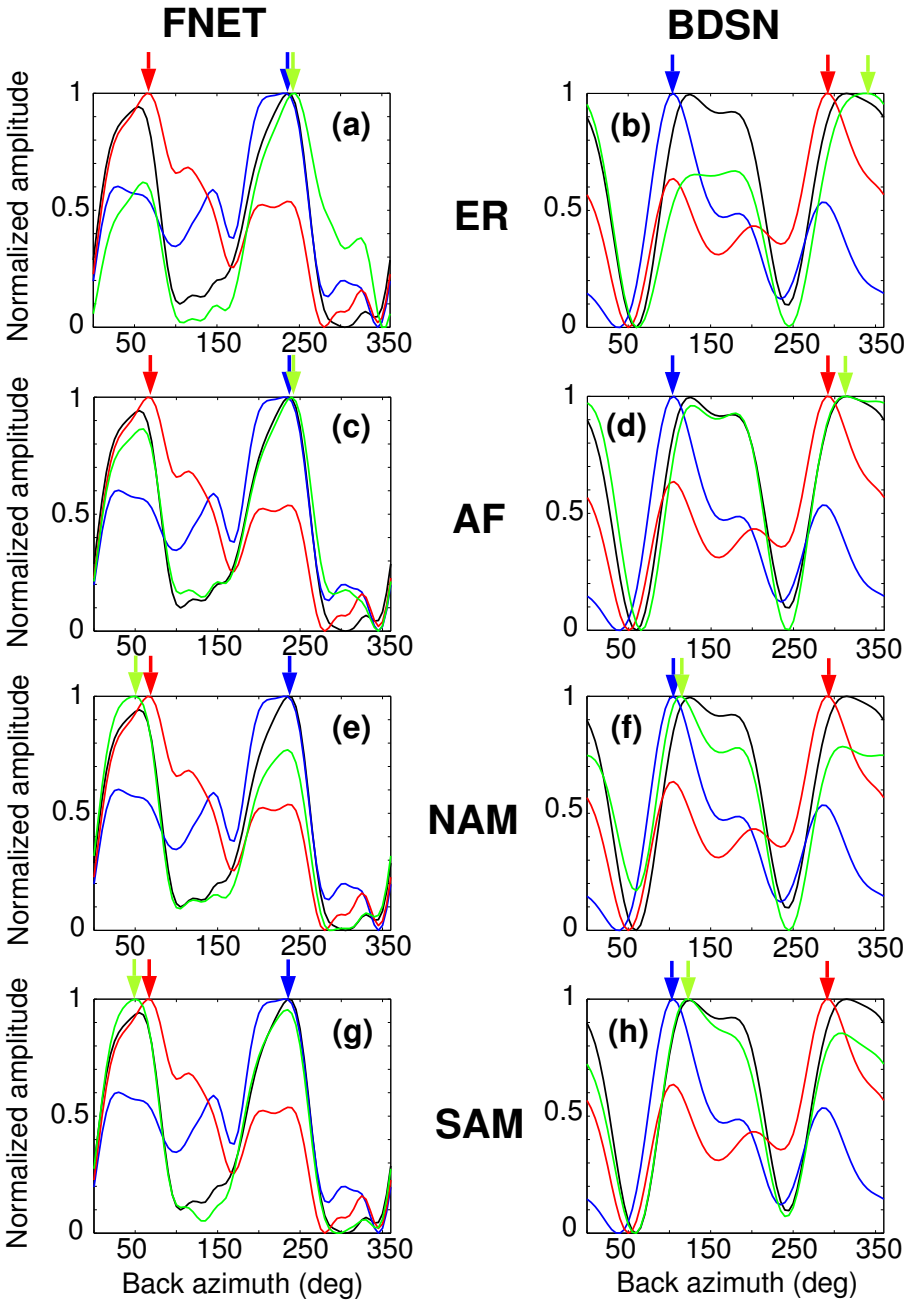

Figure 2.12: continued

Figure 2.13: Results of forward modeling of stack amplitudes as a function of azimuth, for F-net (left) and BDSN (right) for a distribution of sources concentrated over selected oceanic areas. Predicted stack amplitudes as a function of azimuth (green curves) are compared to observed ones for winter (top, red curves) and summer (bottom, blue curves), as well as those predicted for a globally uniform distribution of sources (black curves). Starting from a globally uniform distribution of sources, source amplitudes are increased in specified oceanic areas. a and b: Winter. The region considered is the northern Pacific ocean defined as spanning latitudes 0°N-60°N and longitudes 150°E-135°W, with source amplitudes increased by 150 % in this region. c and d: Summer. Here the region comprises part of the south Atlantic ocean (45°W-0°E and 75°S-10°S), with source amplitudes increased by 400 % with respect to the starting globally uniform distribution, and part of the south Pacific Ocean (160°E-90°W and 60°S-30°S) with source amplitudes increased by 200 %. In both winter and summer, predicted amplitude variations as a function of back-azimuth are compatible with the observed amplitudes at both arrays. In order to obtain more accurate fits, we would need to perform much more refined modeling, which is not warranted, given that the observed stack amplitudes are averaged over 6 months in each season, and during this time span the distribution of sources is likely not completely stationary. There are also other sources of noise (non-Rayleigh wave related) which may influence the details of the observed curves, and which we do not take into account in our experiments.

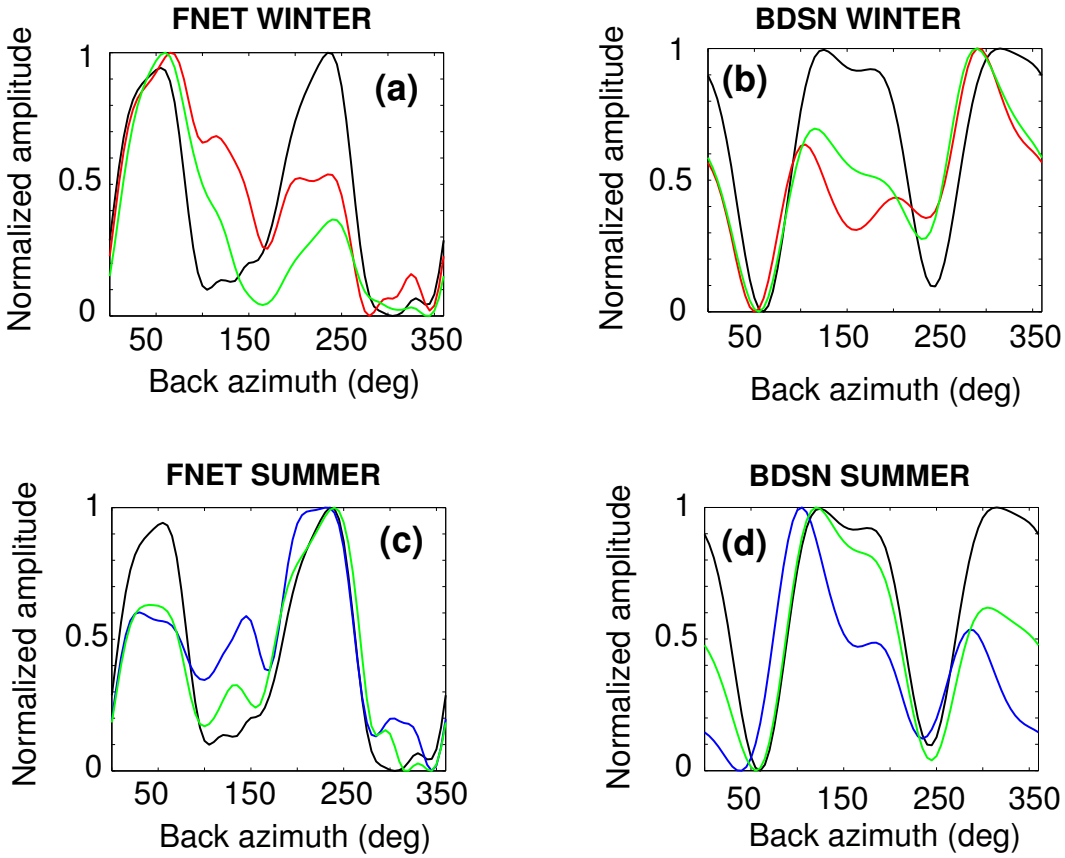

Figure 2.13: continued

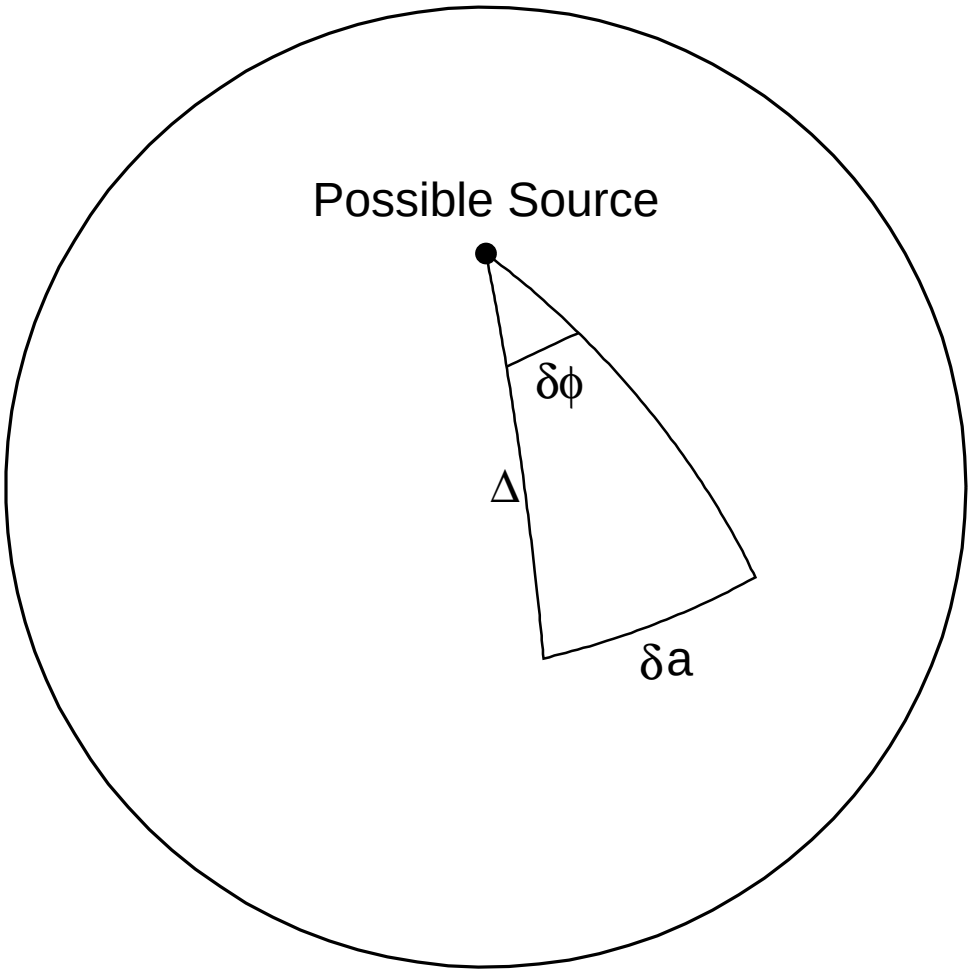

Figure 2.14: Definitions of some parameters used in the misfit function

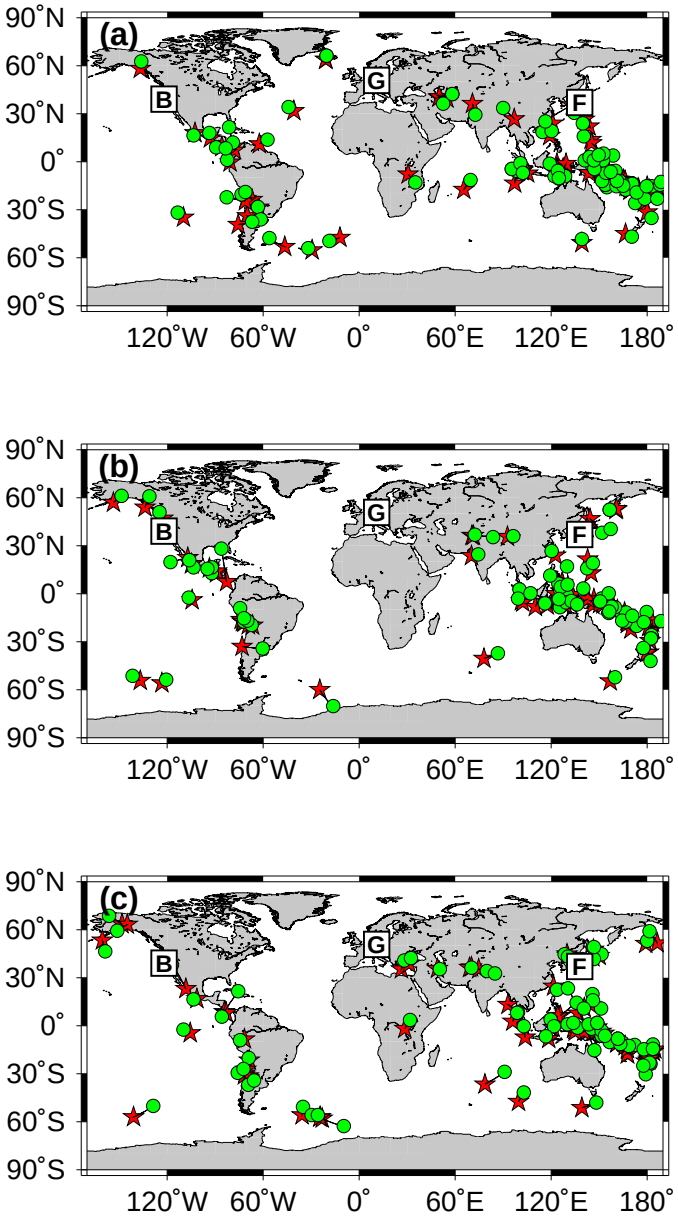

Figure 2.15: Comparison of catalogued (red asterisk) and estimated (green circle) locations of $M_w \geq 6$ events during the years 2000 (a), 2001 (b), and 2002 (c). F(F-net), B(BDSN), and G(GRSN) indicate three arrays used in the analysis.

Chapter 3

A study of the relationship between ocean storms and the Earth's hum

This chapter has been submitted to *Geochem. Geophys. Geosys.* [*Rhie and Romanowicz*, 2006a] under the title 'A study of the relation between ocean storms and the earth's hum'

Summary

Using data from very broadband regional seismic networks in California and Japan, we previously developed an array based method to locate the sources of the earth's low frequency "hum" and showed that it is generated primarily in the northern oceans during the northern hemisphere winter and in the southern oceans during the summer.

In order to gain further insight into the process that converts ocean storm energy into

elastic energy through coupling of ocean waves with the seafloor, we here investigate a four days long time window in the year 2000, which is free of large earthquakes. During this particular time interval, two large "hum" events are observed, which can be related to a storm system moving eastward across the north Pacific ocean. From a comparison of the time functions of these events and their relative arrival times at the two arrays, as well as observations of significant wave height recorded at ocean buoys near California and Japan, we infer that the generation of the "hum" events occurs close to shore and comprises three elements: 1) short period ocean waves interact non-linearly to produce infragravity waves as the storm-related swell reaches the coast of north America; 2) infragravity waves interact with the seafloor locally to generate long period Rayleigh waves, which can be followed as they propagate to seismic stations located across north America; 3) some free infragravity wave energy radiates out into the open ocean, propagates across the north Pacific basin, and couples to the seafloor when it reaches distant coasts north-east of Japan, giving rise to the corresponding low frequency seismic noise observed on the Japanese F-net array. The efficiency of conversion of ocean energy to elastic waves depends not only on the strength of the storm but also on its direction of approach to the coast, and results in directionality of the Rayleigh waves produced.

We also compare the yearly fluctuations in the amplitudes observed on the California and Japan arrays in the low frequency "hum" band (specifically at ~ 240 s) and in the microseismic band (2-25 s). The amplitude of microseismic noise fluctuates seasonally and correlates well with local buoy data throughout the year, indicating that the sources are primarily local, and are stronger in the winter. On the other hand, the amplitude of the "hum" can be as strong in the summer as in the winter, reflecting the fact that seismic waves in the "hum" band propagate efficiently to large distances, from the southern hemisphere where they are generated in the summer. During the winter, strong correlation between the amplitude fluctuations in the "hum" and microseismic bands at BDSN and weaker correlations at F-net is consistent with a common generation mechanism of both types of seismic noise from non-linear interaction of ocean waves near the west coast of North America.

3.1 Introduction

Since the discovery of the earth's "hum" [*Nawa et al.,* 1998], seismologists have tried to determine the source of the continuous background free oscillations observed in low frequency seismic spectra in the absence of earthquakes.

In the last decade, some key features of these background oscillations have been documented. First, their source needs to be close to the earth's surface, because the fundamental mode is preferentially excited [*Nawa et al.,* 1998; *Suda et al.,* 1998] and no clear evidence for higher mode excitation has yet been found. Second, these oscillations must be related to atmospheric processes, because annual [*Nishida et al.,* 2000] and seasonal [*Tanimoto and Um,* 1999; *Ekström,* 2001] variations in their amplitudes have been documented. Finally, they are not related to local atmospheric variations above a given seismic station, since correcting for the local barometric pressure fluctuations brings out the free oscillation signal in the seismic data more strongly [e.g., *Roult and Crawford*, 2000].

Early studies proposed that the "hum" could be due to turbulent atmospheric motions and showed that such a process could explain the corresponding energy level, equivalent to a M 5.8-6.0 earthquake every day [*Tanimoto and Um,* 1999; *Ekström,* 2001]. However, no observations of atmospheric convection at this scale are available to confirm this hypothesis. In the meantime, it was suggested that the oceans could play a role [*Watada and Masters*, 2001; *Rhie and Romanowicz*, 2003; *Tanimoto,* 2003].

Until recently, most studies of the "hum" have considered stacks of low frequency spectra for days "free" of large earthquakes. In order to gain resolution in time and space and determine whether the sources are distributed uniformly around the globe, as implied by the atmospheric turbulence model [e.g., *Nishida and Kobayashi*, 1999], or else have their origin in the oceans, it is necessary to adopt a time domain, propagating wave approach. In a recent study, using an array stacking method applied to two regional arrays of seismic stations equipped with very broadband STS-1 seis-

mometers [*Wielandt and Streckeisen*, 1982; *Wielandt and Steim*, 1985], we showed that the sources of the "hum" are primarily located in the northern Pacific ocean and in the southern oceans during the northern hemisphere winter and summer, respectively [*Rhie and Romanowicz*, 2004 hereafter referred to as RR04], following the seasonal variations in maximum significant wave heights over the globe, which switch from northern to southern oceans between winter and summer. We suggested that the generation of the hum involved a three stage atmosphere/ocean/seafloor coupling process: 1) conversion of atmospheric storm energy into short period ocean waves, 2) non-linear interaction of ocean waves producing longer period, infragravity waves; 3) coupling of infragravity waves to the seafloor, through a process involving irregularities in the ocean floor topography. However, the resolution of our study did not allow us to more specifically determine whether the generation of seismic waves occurred in the middle of ocean basins or close to shore [e.g., *Webb et al.*, 1991; *Webb*, 1998]. The preferential location of the sources of the earth's "hum" in the oceans has now been confirmed independently [*Nishida and Fukao*, 2004; *Ekström and Ekström*, 2005]. In a recent study, *Tanimoto* [2005] showed that the characteristic shape and level of the low frequency background noise spectrum could be reproduced if the generation process involved the action of ocean infragravity waves on the ocean floor, and suggested that typically, the area involved in the coupling to the ocean floor need not be larger than about $100 \times 100\ km^2$.

On the other hand, oceanographers have long studied the relation between infragravity waves and swell. Early studies have documented strong correlation between their energy levels, which indicate that infragravity waves are driven by swell [e.g., *Munk*, 1949; *Tucker*, 1950]. Theoretical studies have demonstrated that infragravity waves are second order forced waves excited by nonlinear difference frequency interactions of pairs of swell components [*Hasselmann*, 1962; *Longuet-Higgins and Steward*, 1962]. A question that generated some debate was whether the observed infragravity waves away from the coast are "forced" waves bound to the short carrier ocean surface waves and traveling with their group velocity, or "free" waves released in the surf zone and subsequently reflected from the beach which, under certain conditions, may radiate

into deep ocean basins [e.g., *Sutton et al.*, 1965; *Webb et al.*, 1991; *Okihiro et al.*, 1992; *Herbers et al.*, 1994, 1995a, 1995b]. In particular, *Webb et al.* [1991] found that infragravity wave energy observed on the seafloor away from the coast was correlated not with the local swell wave energy but with swell energy averaged over all coastlines within the line of sight of their experimental sites, in the north Atlantic Ocean and off-shore southern California.

Recently, we analyzed the relation between ocean storms off-shore California and infragravity wave noise observed on several broadband seafloor stations in California and Oregon [*Dolenc et al.*, 2005a]. We also found that the seismic noise observed in the infragravity wave band correlates with significant wave height as recorded on regional ocean buoys, and marks the passage of the storms over the buoy which is closest to the shore. More recent results based on data from an ocean floor station further away from shore [*Dolenc et al.*, 2005b] indicate that the increase in amplitude in the infragravity frequency band (50-200 s) associated with the passage of a storm occurs when the storm reaches the near coastal buoys, and not earlier, when the storm passes over the seismic station. This implies that pressure fluctuations in the ocean during the passage of the storm above the station can be ruled out as the direct cause of the low frequency seismic noise.

In this paper, we investigate these processes further in an attempt to better understand where the coupling between infragravity waves and ocean floor occurs, generating the seismic "hum". In particular, we describe in detail observations made during one particular time period of unusually high low frequency noise. We also present comparisons of the observed low frequency seismic "hum" with noise in the microseismic frequency band (2-25 s), and discuss the relation between the two phenomena.

3.2 Earthquake "free" interval 2000.031-034

In our previous study [RR04], we extracted time intervals which were not contaminated by earthquakes, using strict selection criteria based on event magnitude. This significantly limited the number of usable days in a given year. For example, only 64 days of "earthquake free" data were kept for the year 2000. Among these, we identified the time interval 2000.030 to 2000.034 (i.e., January 30 to February 3) as a particularly long interval free of large earthquakes, during which the background noise amplitude was unusually high, and during which two large noise events were observed, that could be studied in more detail.

As described in RR04, we considered data at two regional arrays of very broadband seismometers, BDSN (Berkeley Digital Seismic Network) in California, and F-net in Japan. For each array, we stacked narrow-band filtered time domain vertical component seismograms according to the dispersion and attenuation of Rayleigh waves, assuming plane wave propagation from an arbitrary azimuth. Here, we apply a 6 hour running average with a time step of 1 hour to the stacked data at BDSN and F-net respectively. At each time step, the stack amplitude has a maximum corresponding to a particular back-azimuth. We consider the resulting maximum stack amplitudes (MSA) as a function of time.

First, we estimate the background level of the low frequency seismic energy by determining a scaling factor between the observed peak amplitudes (from the MSA at 240 s), and the moment magnitudes of the corresponding earthquakes ($M_w > 6.0$), as listed in the Harvard CMT catalog [*Dziewonski and Woodhouse,* 1983]. Since we know the location of both the array and each earthquake, as well as the event origin time, we can calculate the theoretical onset time of the R1 train at the center of the array and select only those peaks that correspond to the arrival time of the R1 train. However, the selection of R1 peaks is made difficult by the presence of secondary peaks corresponding to later arriving Rayleigh wave trains from the previous larger earthquakes (R2,R3...). When such secondary peaks are present, the corresponding

seismic amplitude is significantly larger than estimated, on average, based on the magnitude of the earthquake considered. When estimating the scaling factor, and to reduce contamination due to large previous events, we therefore discard those peaks from the dataset that have relatively high amplitude for a given magnitude level. This means that, when applying this scaling factor, our estimate of the hum level is maximum (Figures 3.1a and 3.1b). Since we ignore the effects of geometrical spreading, attenuation during propagation, as well as radiation pattern, this is a very crude estimate. However, the estimated noise background level is consistent with what has been previously reported (Figures 3.1c and 3.1d) from the analysis of free oscillation data (e.g., M_w 5.75, *Ekström*, 2000; M 6.0, *Tanimoto and Um*, 1999).

We consider the 15 day period 2000.25 to 2000.40. In Figure 3.2, we plot the MSA as a function of time in four different period bands. We here use a linear scale for the MSA (different from Figure 3.1) to more clearly see the variations in amplitude of the background noise. We note the well defined signature of large earthquakes, which have a sharp onset, a slower decay and a relatively sharp end. At the time resolution considered here, this onset is practically coincident at both arrays. The duration of the earthquake signal increases with the size of the earthquake and is typically on the order of 0.5 day for M_w 6 and 1-1.5 day for M_w 7 earthquakes, after which the signal drops below the average background noise level. This is consistent with what one expects from the decay of earth circling mantle Rayleigh waves generated by large earthquakes.

Table 1 lists all earthquakes larger than M 5.0 during these 15 days, as reported in the NEIC catalog. During the time interval 2000.031 to 2000.034, there are no earthquakes larger than M 5.5, yet the background noise rises well above the noise floor, forming two particularly long events, with a very different signature from that of earthquakes: the rise time is longer, the decay very slow and the ratio of the duration of each event to its maximum amplitude, significantly larger. These two noise events are observed on both arrays (i.e., in California and in Japan), and there is a lag time of several hours between the two arrays. The second event is weaker at

the longest periods. We verify that the back-azimuth corresponding to the maximum amplitude is very stable during these two events, as illustrated in Figure 3.3, which also emphasizes the delay of about 8-10 hours between the main energy arrivals at BDSN and F-net. We will discuss these events in detail in what follows.

This particular "earthquake free window" is unique in that it lasts several days, and the noise events are large. However, noise events with similar characteristics are observed at other times as well. For example, Figure 3.4 shows a similar plot for the time period 2002.340 to 2002.355, in which we observe a noise event beginning on day 2002.349, showing similar time evolution as for the events in 2000 described above: a slow rise time and lag of $\sim 8-10$ hours between the two arrays. It is followed by a second noise event of similar characteristics, but partially hidden behind an earthquake of $M_w > 6$. In what follows, we return to the time period 2000.031-034 for further analysis.

The large noise events observed on days 2000.031 and 2000.033 after applying a smoothing moving average to the MSA, are the coalescence of multiple smaller events, which, as we showed previously, propagate across the two arrays with the dispersion characteristics of Rayleigh waves [see Figure 1 in RR04]. In order to locate the sources of these disturbances in RR04, we applied a back-projection grid-search method to the original time series, after band-pass filtering between 150-500 s, over a 6 hour period containing the maximum stack amplitude on day 2000.031. We showed that the sources of Rayleigh waves that best fit the amplitudes observed both at BDSN and F-net are located in the north Pacific ocean basin. We here apply the same back-projection method, but using a narrow band filter centered at 150 and 100 s respectively, and obtain a band of source locations which follows the north Pacific shoreline, as illustrated in Figure 3.5. This is particularly clear at 100 s.

In order to obtain a stable solution using the grid search method, it is necessary to process a time interval of length about 6 hours, indicating that many of the small events which compose the larger noise event on day 2000.031 are too small to be

studied individually, at least with this method. Here we show that the large "composite" event, obtained when using the 6 hour moving average, propagates west to east across the whole North American continent, with an amplitude decay consistent with the propagation of Rayleigh waves. Instead of stacking the noise data over an array of broadband seismic stations, we here consider five quiet broadband stations in north America, and, for each of them, we compute power spectral density (PSD) as a function of time, with a 6 hour moving window and a 1 hour lag (Figure 3.6). All five stations show an increase in background noise during days 31-32, and another one, with smaller amplitude and narrower frequency range, on day 33 (except for CCM for which data are not available on that day). Figure 3.7a compares the mean fourier amplitudes at stations CMB, TUC, ANMO and HRV, averaged over the period range 100-200 s and time range 2000.31,00:00 and 2000.32,06:00. We chose this period range, because at lower frequencies, the background noise is dominated by site effects at some of the stations. From the amplitude decay it is possible to obtain a very rough estimate of the location of the source of Rayleigh waves by forward amplitude modeling. The results are shown in Figure 3.7c, using CMB, TUC, ANMO and HRV. Because the available azimuth range is not very wide, there is a large uncertaintly in the longitude of the inferred source. However, it is compatible with a location near the west coast of North America. Figure 3.7b compares the observed and predicted average Fourier amplitudes at four stations. The amplitudes are normalized to those of the most western station (CMB) and the predicted amplitudes are computed assuming the Q model of PREM for Rayleigh waves [*Dziewonski and Anderson,* 1981] and accounting for geometric spreading.

3.3 Correlation with ocean buoy data

To further investigate the origin of the noise events on days 2000.031 and 2000.033, we now turn to a comparison with ocean buoy data. We collected significant wave height (SWH) data measured at buoys deployed in the north Pacific by the National Ocean and Atmospheric Administration (NOAA) and the Japan Meteorological Agency (JMA) and operational during those days. We compare SWH time series for this time period to the time evolution of the maximum stack amplitudes at BDSN and F-net for the same time interval. Figure 3.8 shows such a comparison for buoys located near Japan and near the California coast. The time series on all buoys closely resemble the "source signature" on the seismic stacks, shown here at a period of 240 s. This is the case for the event on 2000.031 as well as for the smaller one on 2000.033. The seismic noise events on BDSN lag those observed on buoy 46059 by about 10-12 hours, but are more or less coincident (to within 1 hour, which is the minimum resolution of these plots) with the events observed on the near shore buoys, indicating that the location of the coupling between ocean waves and the seafloor occurs somewhere between buoy 46059 and the shore, which is consistent with the results of Figure 3.7c. The ocean storm which generated the short period waves observed on buoys both near Japan and near the western US moved from east to west across the north Pacific basin. Unfortunately, we could not find any buoy data closer to the eastern coast of Japan, or in other parts of the western Pacific ocean. To further investigate the source of these waves, we therefore turn to wave models. Figure 3.9 shows snapshots of the evolution of wave height in the northern Pacific for day 2000.031, from the WAVEWATCH III model [*Tolman*, 1999]. During that day, a large storm arrives from the west towards the coast of California and Oregon. It reaches the coast, according to the model, between 6h and 12h on day 2000.031. It is followed by a smaller "tail", about 3000 km behind, which, in turn, according to the WAVEWATCH III model, reaches the coast between 0h and 6h on day 2000.033 (not shown). The following storm system, which forms in the western part of the north Pacific (around longitude 160°E on figure 3.9) on day 2000.031 develops into a stronger

storm over the next few days. This can be seen in the animation provided by NOAA at: http://ursus-marinus.ncep.noaa.gov/history/waves/nww3.hs.anim.200001.gif and http://ursus-marinus.ncep.noaa.gov/history/waves/nww3.hs.anim.200002.gif). This storm is not associated with any significantly increased seismic noise on BDSN or F-net (Figure 3.2). Notably however, in contrast to the previous one, this storm does not reach the California coast, but dissipates in the middle of the ocean. The distribution of wave heights on Figure 3.9, together with the observation of the significant delay in the stack energy at F-net with respect to the BDSN (see also Figure 3.3), leads us to propose the following sequence of events.

On day 2000.031, a large storm, which developed two days earlier in the middle of the north Pacific basin (according to wave models and buoy data) and moving eastwards towards north America, reaches the vicinity of the western United States coast. A second storm, weaker, but with similar characteristics, follows by about 2 days. The seismic background noise observed on the BDSN and F-net arrays has the same amplitude signature, as a function of time, as the storms. The process that converts the storm energy into seismic energy, which then propagates as Rayleigh waves, in particular through the north American continent, appears to involve several steps (Figure 3.10): when the storm approaches the US coast with its rough seafloor topography, short period ocean waves interact non-linearly to produce infragravity waves. Part of the infragravity wave energy then converts to seismic waves locally, to produce the background noise event observed on BDSN, and part is reflected back out to the ocean and travels across the Pacific basin, in agreement with oceanographic studies of the generation of infragravity waves [e.g., *Munk et al.*, 1964; *Elgar et al.*, 1992; *Herbers et al.*, 1995a, 1995b]. We estimate that, at $\sim$220 m/s, "free" infragravity waves propagate about 6000-8000 km in 8-10 hours. Consistent with the back-azimuth of the maximum arrival of energy, the conversion from infragravity waves to seismic waves detected on F-net primarily occurs in the vicinity of the western Aleutian arc. We note that the absolute level of MSA is larger at BDSN than at F-net (e.g., Figures 3.3 and 3.8), in agreement with the inference that the source for F-net should be comparatively more distant and also weaker.

We infer that free infragravity waves play a role in generating the seismic disturbances in Japan because of the 8-10 hour time delay between stack maxima on BDSN and F-net. This is consistent with observations of remotely generated infragravity waves [e.g., *Herbers et al.*, 1995a]. This time delay is too short for propagation of short period ocean waves (and also "bound" infragravity waves) from the center of the north Pacific basin, and much too long for propagation of seismic waves from a source near the US coast to Japan. An alternative scenario for the sources of seismic noise on F-net could involve the storm which forms on the Japan side of the Pacific in the middle of day 2000.031 (Figure 3.9). However, we rule this out, because this storm intensifies only later and reaches its peak around 03h on day 2000.032, which is much later than the long period seismic peak on F-net.

In summary, the seismic sources that form the composite events on days 2000.031 and 2000.033 are distributed around the Pacific, both in time and space, but have a common cause: a strong storm system which "hits" the north American coast broadside. A similar type of storm which reaches north America from the west, occurs on day 2002.349 (Figure 3.11), causing the disturbances observed on Figure 3.4. We infer that the efficiency of generation of seismic waves is particularly high for these storms, due to their direction of approach to the North American Coast, and the fact that these storms actually reach the coast. This is why we can observe these remarkable "noise events" on the stacks at BDSN and F-net so clearly. We have evidence of directionality of the process, in that station COL (Alaska) does not show any increase of seismic noise in the 70-250 s pass band during the same time period. At least, it is below detection level by our methodology involving PSD spectra, even though there is an indication, from the noise in the microseismic bandpass (2-25 s) of a storm reaching the Alaska coast nearby at the end of day 2000.031 (Figure 3.12). Such directionality would also explain why we can so clearly follow the particular seismic disturbance on day 2000.031 across North America.

Other north Pacific storms must also generate long period seismic noise, however, the corresponding noise "events" cannot often be identified as clearly because they are

either hidden behind large seismic events, or do not have sufficient amplitude levels to rise above the average noise level on the two seismic arrays considered. We note that many winter storms never reach the north American coast, or turn further north into the Gulf of Alaska. A systematic analysis of storm characteristics in the north Pacific in relation to the "hum" is beyond the scope of this paper and will be addressed in a further study.

3.4 Comparison with microseisms

We have shown that infragravity waves generated by winter storms in the north Pacific ocean contribute to the source of the low frequency "hum" events observed in California and Japan.

The non-linear wave interactions that give rise to infragravity waves are also responsible for the generation of double frequency microseisms [e.g., *Hasselmann*, 1962, 1963; *Longuet-Higgins*, 1950], which are themselves correlated with the wind wave spectrum [e.g., *Babcock et al.*, 1994; *Webb and Cox*, 1986; *Bromirski and Duennebier*, 2002], and are known to be generated primarily locally near the coast [e.g., *Haubrich and McCamy*, 1969; *Webb,* 1998; *Bromirski et al.*, 2005].

Therefore, we next investigate the relationship between microseisms, ocean storms and the low frequency "hum". Even though there are two types of microseisms, primary (at periods lower than 10 s) and secondary, or "double-frequency", at periods around 6-8 s, and their generation mechanisms are different [e.g., *Friedrich et al.*, 1998; *Webb*, 1998], the double frequency microseisms dominate the spectra and we will only consider those in the discussion that follows.

We first computed mean Fourier amplitudes in the microseismic period band (2 to 25

s) at individual stations of BDSN and F-net for the time interval 2000.031- 2000.035. We used moving windows of duration 30 mn, shifted by 10 mn. We removed mean and trend before computing Fourier amplitudes. We then compared them to near-by buoy data (Figures 3.13 and 3.14). Along the coast of California (Figure 3.13), the mean seismic amplitudes show the signatures of the two noise events already discussed at low frequency (on days 2000.031 and 2000.033), which are also well defined on the buoy data. The eastward moving storm arrives first in northern and central California, as seen by the slight delay in its waveheight signature at buoy 46062 compared to the other two buoys (see also the data from buoy 46059 on Figure 3.8). The timing of the peak of microseismic noise at the three stations and the fact that the amplitude at station ISA is smaller by about a factor of 3 than at BKS, indicate that the generation of the microseisms occurs closer to the central and northern California buoys.

Unfortunately, only data for three buoys are available around Japan for this time period. However, we note that the mean microseismic Fourier amplitudes at the three seismic broadband stations closest to the buoys show a good correlation with SWH data (Figure 3.14). We also note that, contrary to the observations in California, the timing and shape of the microseismic amplitude variations is different from that at "hum" frequencies, and varies significantly with location of the station in the array (Figure 3.15), indicating that, in Japan, the sources of the microseismic noise and of the hum are distinct: the low frequency noise is related to that observed on the eastern side of the Pacific (with a delay which we attribute to the propagation of infragravity waves across part of the Pacific ocean), whereas the microseismic noise maximum occurs significantly earlier (on day 2000.030). In fact, some groups of stations see two peaks, corresponding to local storms moving up and down the Japan coast.

To further investigate the relation between microseismic noise and the low frequency hum, we need to be able to compare amplitude levels in the two frequency bands for long time intervals (e.g., a whole year). To do so effectively, we developed a data processing method that avoids eliminating the numerous time windows that are contaminated by earthquakes.

In order to minimize the effect of earthquakes at low frequencies, we compute the minimum, as a function of time, of the scaled MSA time series, using a moving time window with a duration of 1.5 days and a 6 hour shift. This effectively removes some large amplitude peaks due to earthquakes, but not all. We then apply a low pass filter with a corner period of 1 day to the time series obtained in the previous step. This further removes most of the earthquake related peaks, except for those with the longest duration, corresponding to the largest earthquakes (Figures 3.16a, 3.16b, and 3.16c). We also compute the mean Fourier amplitude in the microseismic band (2-25 s) for seven BDSN stations. Here the contamination by large earthquakes is not as severe and we only remove those points which correspond to large temporal gradients. To do so, we empirically determined a gradient threshold between two consecutive points in the amplitude time series: if the measured gradient is higher than the threshold, we remove the end point and test the gradient value for successive end points, until the gradient drops below the threshold. Finally, we low pass filter the amplitude time series with a corner period of 1 day (Figures 3.16d, 3.16e, and 3.16f). This effectively removes most of the earthquake signals.

We compare the filtered "hum" and microseism amplitude time series over a period of one year, for each array. In the case of California (BDSN), the level of low frequency noise does not vary systematically with time (Figure 3.17a), but there is a seasonal variation in the microseismic amplitude, with a minimum during northern hemisphere summer time, as is also seen in the ocean wave height data (Figure 3.17b). This indicates that the sources of energy for the long period and short period noise are different during the summer. The variation in microseismic amplitude at BDSN stations is clearly related with ocean wave height measured by local buoys (Figure 3.17b). We can see a similar trend for F-net, but the correlation of the variation in short period amplitudes and ocean wave data is weaker than in the case of BDSN (Figures 3.17c and 3.17d).

Removing the time periods contaminated by the largest events, and restricting our analysis to northern hemisphere winter (January to March and October to Decem-

ber), we compute the correlation coefficients between the low frequency and high frequency filtered noise time series, for three consecutive years, at BDSN. Correlation coefficients are significant, between 0.39 and 0.60 (Figure 3.18). This indicates that in the winter, both the low frequency hum and the microseismic noise observed at BDSN are generated locally. On the other hand, the corresponding correlation coefficients for F-net are generally much lower: for the first 3 months of each year, respectively: -0.11, (N/A) and 0.21; for the last 3 months of each year, respectively: 0.22,-0.02, 0.30.

The correlation between the hum and microseismic noise at BDSN during the winter is compatible with a common generation mechanism for both types of seismic noise, involving non-linear interactions between surface ocean waves giving rise, on the one hand, to double frequency microseisms, and on the other, to infragravity waves [e.g., *Hasselmann,* 1962]. The fact that the correlation is somewhat weaker at F-net is in agreement with our proposed scenario, in which the dominant effect is that of storms moving from West to East across the Pacific and reaching the west coast of North America to produce low frequency seismic "hum".

3.5 Conclusion

We have made progress in clarifying the mechanism of generation of continuous free oscillations, based on the observations for a time interval free of earthquakes during which two large long period noise events are present in the MSA at BDSN and F-net. We have shown that these events can be related to a particular winter storm system.

A perturbation in the atmosphere, typically a winter storm moving eastward across the north Pacific basin, generates short period ocean waves. As the storm reaches the north-American coast, the non-linear interaction between ocean waves generates

long period infragravity waves, some of which convert locally to long period seismic energy, and others propagate long distance across the ocean basin and couple to the seafloor near northeastern coasts. The resulting long period seismic waves propagate over the globe and give rise to the "hum". In particular, we were able to track the seismic energy generated off-shore California by the storm considered on day 2000.031, throughout the north American continent.

The directionality of the "hum" radiation suggested by our data needs to be further characterized, in particular for the benefit of studies of structure based on the analysis of noise cross-correlations [e.g. *Shapiro et al.*, 2005], at least at low frequencies. Indeed, the sources of low frequency seismic noise can no longer be considered as uniformly distributed either in time, or in space.

The annual fluctuations of long (hum band) and short (microseism band) period seismic amplitudes at BDSN and F-net show quite different features. We can clearly see the seasonal change in amplitude in the microseism band (2-25 s) with a minimum during northern hemisphere summer, whereas the amplitude in the hum band (here considered at $\sim$ 240s) does not show clear seasonal variations. We also observed a significant correlation between seismic amplitudes at BDSN in the microseism and hum bands during northern hemisphere winter. We had previously documented that the source of the hum observed at BDSN and F-net shifts from the northern Pacific to the southern oceans between winter and summer, so that the sources are more "local" in the winter than in the summer. In contrast, microseisms propagate less efficiently at large distances, so the source is primarily local. These observations are in agreement with a common mechanism for the simultaneous generation of short and long period seismic noise near the California coast, as inferred from theoretical studies.

Date	Time	Latitude	Longitude	Depth	Mag.
2000/01/25	16:43:22.95	27.6630	92.6310	33.0	5.20
2000/01/26	13:26:50.00	-17.2720	-174.0020	33.00	6.30
2000/01/26	21:37:57.77	30.9730	95.5020	33.00	5.20
2000/01/26	23:00:19.94	40.0210	52.9010	33.00	5.30
2000/01/26	23:34:04.50	-23.7220	-66.4770	221.60	5.00
2000/01/27	02:49:44.91	-34.8070	-105.4590	10.00	5.40
2000/01/27	10:10:57.25	31.6780	141.6860	33.00	5.30
2000/01/28	08:49:30.87	7.4570	-77.8500	21.40	5.40
2000/01/28	13:17:52.87	-7.4850	122.6780	574.90	5.50
2000/01/28	14:21:07.34	43.0460	146.8370	61.10	6.80
2000/01/28	16:39:24.28	26.0760	124.4960	193.90	6.00
2000/01/28	17:57:00.55	14.4350	146.4620	45.20	5.20
2000/01/28	22:42:26.25	-1.3470	89.0830	10.00	5.50
2000/01/28	22:57:51.70	-9.6910	118.7640	83.40	5.60
2000/01/29	02:53:54.89	4.8570	126.2590	100.00	5.10
2000/01/29	05:48:10.77	-20.5630	-178.2880	562.90	5.00
2000/01/29	08:13:10.73	-8.6330	111.1370	60.70	5.40
2000/01/31	07:25:59.74	38.1140	88.6040	33.00	5.40
2000/02/01	00:01:05.42	-4.3580	151.9070	189.00	5.20
2000/02/01	02:00:10.68	13.0100	-88.8470	55.00	5.20
2000/02/02	12:25:21.92	-49.0240	124.9790	10.00	5.40
2000/02/02	21:58:49.71	-5.7300	148.9320	112.80	5.30
2000/02/02	22:58:01.55	35.2880	58.2180	33.00	5.30
2000/02/03	10:24:57.77	65.0087	-154.2390	10.00	5.98
2000/02/03	13:42:25.04	13.5720	121.5460	33.00	5.50
2000/02/03	15:53:12.96	75.2710	10.1950	10.00	5.50
2000/02/04	07:02:11.39	-40.6310	-85.9180	10.00	5.30
2000/01/25	16:43:22.95	27.6630	92.6310	33.0	5.20
2000/02/06	02:08:07.14	1.2950	126.2720	33.00	5.50
2000/02/06	11:33:52.28	-5.8440	150.8760	33.00	6.60
2000/02/07	06:34:49.67	43.3680	147.4330	61.50	5.20
2000/02/07	16:41:04.58	31.0370	141.6940	33.00	5.40
2000/02/08	18:01:27.18	-21.9360	170.0680	33.00	5.40
2000/02/09	04:28:00.48	-16.6660	-172.6960	33.00	5.20
2000/02/09	09:33:54.05	-30.1050	-178.1130	56.70	5.00
2000/02/09	18:40:37.83	-27.6220	65.7240	10.00	5.10

Table 3.1: Earthquake catalog ($M_w > 5.0$) from Jan. 25 to Feb. 9 in 2000 from NEIC

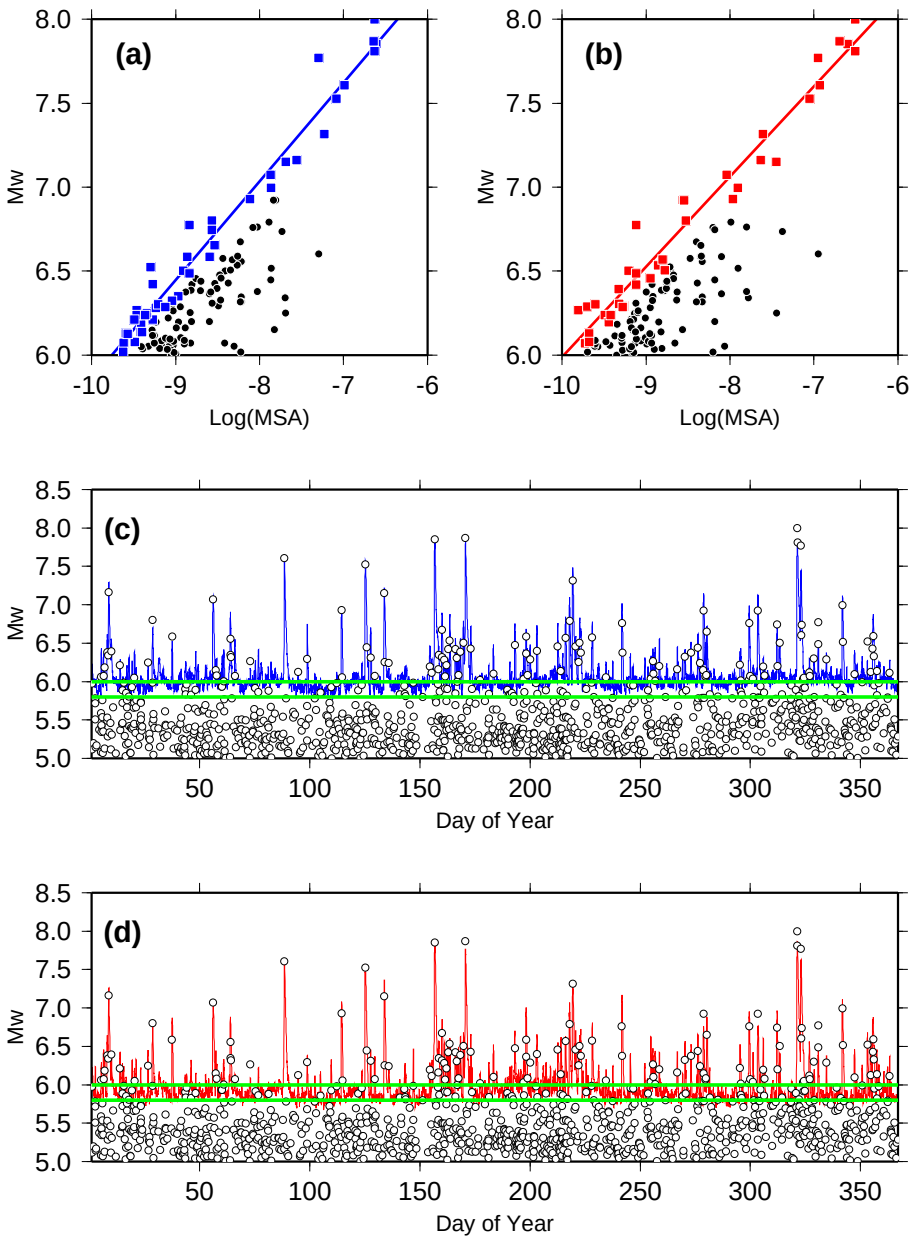

Figure 3.1: Estimation of the level of low frequency background noise (i.e., the hum). (a) Moment magnitudes versus associated maxima in MSA for BDSN. The MSA shown is after applying a moving average over a window of 6 hours with 1 hour offset. Results do not significantly change if no moving average is applied. Black dots indicate all seismic events during the year and solid squares indicate selected maxima which may not be contaminated by later Rayleigh wave trains from other large events. The best fitting line is computed using only the data indicated by blue squares. (b) Same as (a) for F-net. Red squares are selected maxima. (c) Scaled MSA (blue) for BDSN for the year 2000. Open circles represent all large events during 2000. The levels corresponding to M_w 5.75 and M_w 6 are highlighted with green lines. (d) same as (c) for F-net (red).

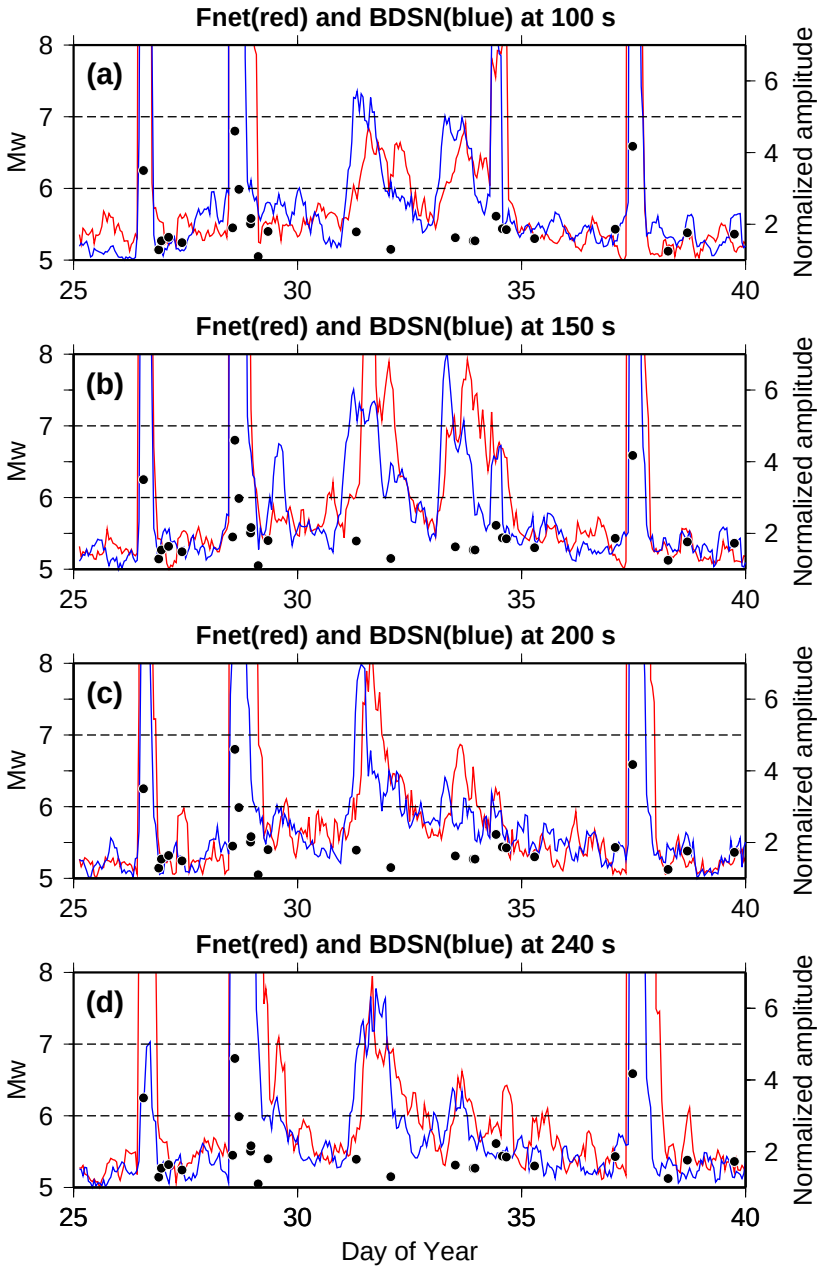

Figure 3.2: (a) Maximum stack amplitude (MSA) filtered by gaussian filter with center period of 100 s for BDSN (blue) and F-net (red) normalized by minimum value. Black dots represent earthquakes which occurred during the period considered. (b-d) Same as (a) for 150, 200 and 240 s.

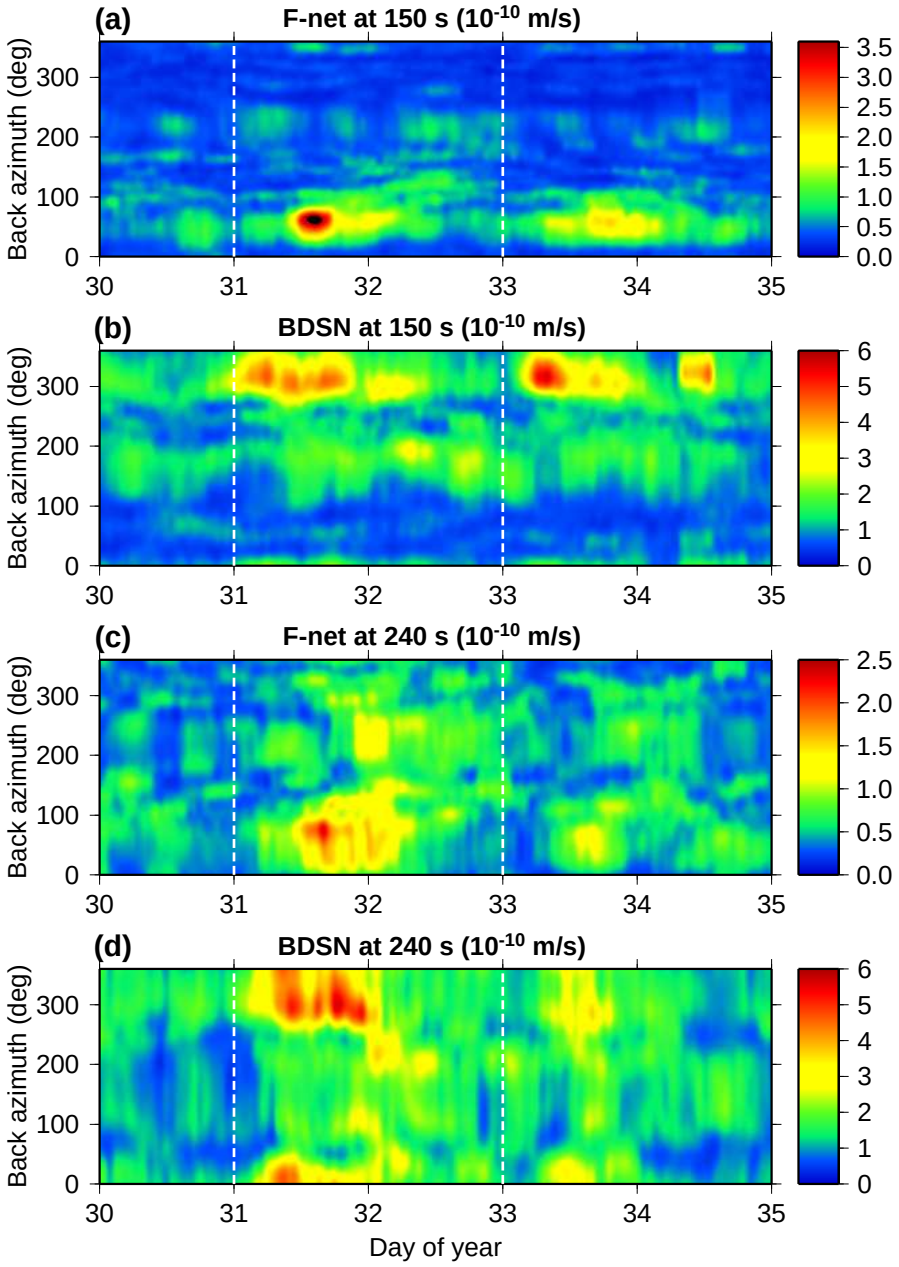

Figure 3.3: (a) Mean stack amplitude with 6 hour time window lagged by 1 hour as a function of time and back azimuth for F-net. A Gaussian filter with center period of 150 s was applied before stacking. (b) Same as (a) for BDSN. (c) Same as (a) for center period of 240 s. (d) Same as (c) for BDSN. The time difference between corresponding energy arrivals at the two arrays on day 31 is about 8-10 hours, with F-net lagging behind BDSN. This is more clearly seen in the shorter period plot.

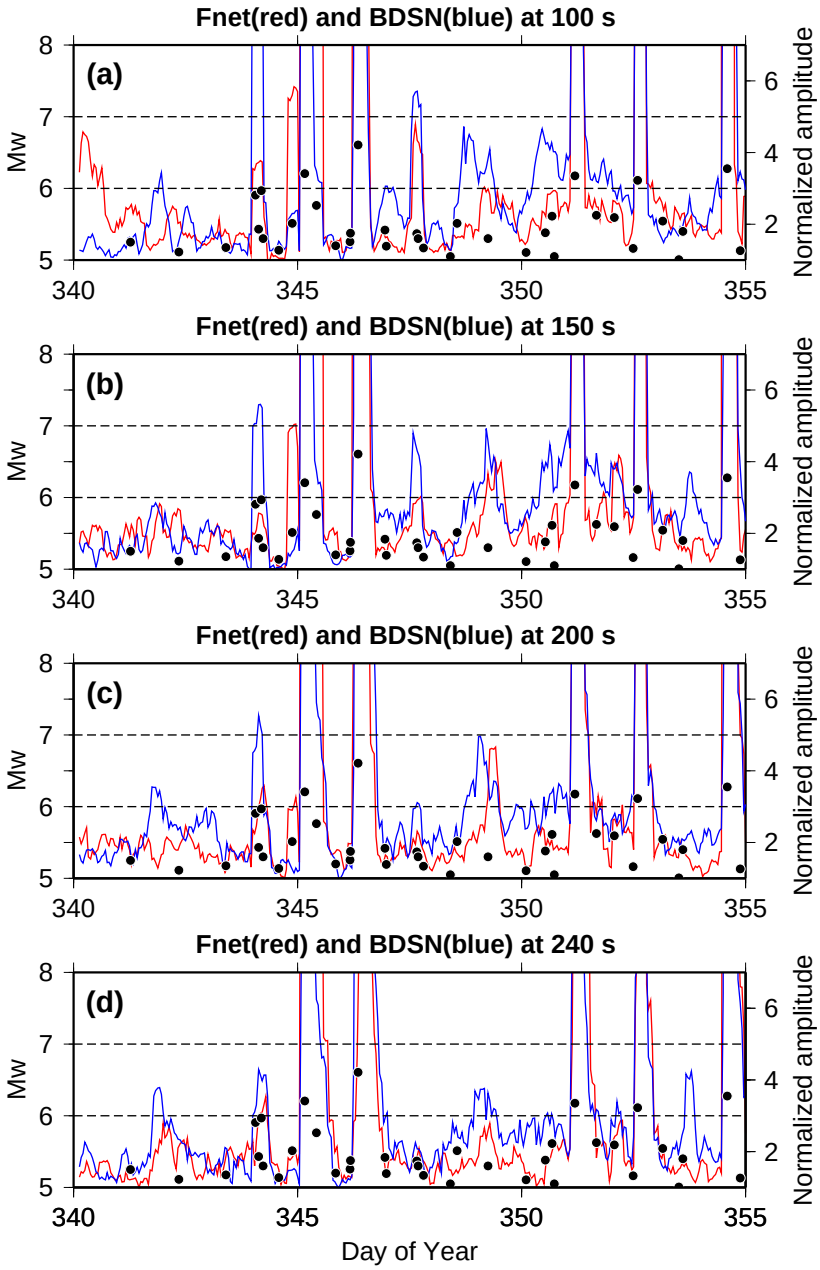

Figure 3.4: Same as Figure 3.2 for days from 340 to 355 in 2002.

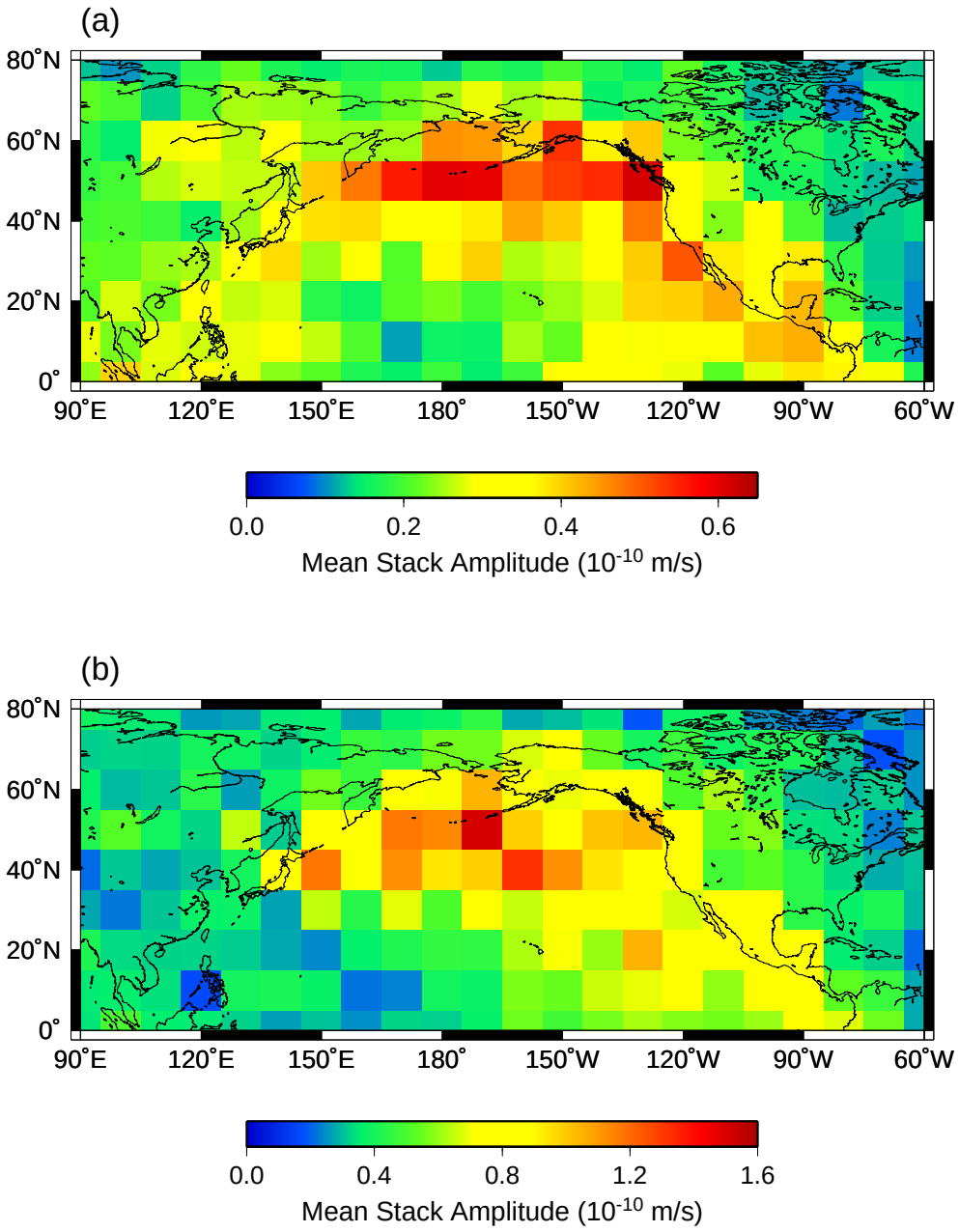

Figure 3.5: (a) Results of grid search method to locate the source of continuous long period Rayleigh waves on Jan 31, 2000. 6 hour waveforms gaussian filtered with center period of 100 s from F-net, BDSN and 10 european stations are used. Color indicates the mean stack amplitude over a 6 hour time window (2000.031,14:00 - 2000.031,20:00 UTC) after correcting waveforms at individual stations for attenuation and dispersion. (b) Same as (a) for 150 s

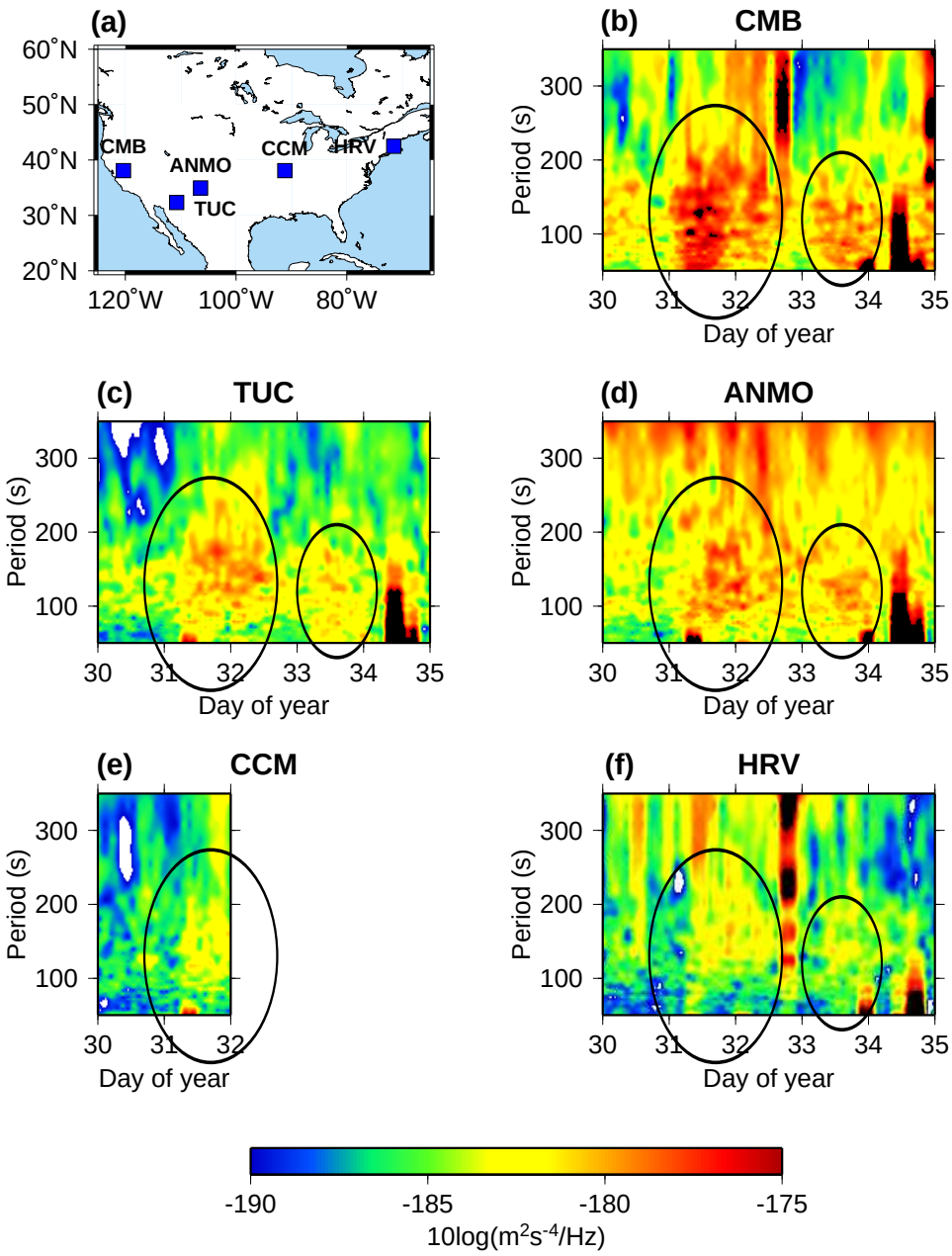

Figure 3.6: (a) Location of five quiet seismic stations in North America. (b) Power spectral density (PSD) at CMB. It is clear that two large seismic energy arrivals (highlighted with black circles) are present on days 031 and 033. (c-f) Same as (b) for TUC, ANMO, CCM, and HRV, respectively. For CCM, the data are missing after day 33 through day 35. Large amplitude signals for periods < 120 s on days 34 and 35 correspond to earthquakes (see Table 5.1).

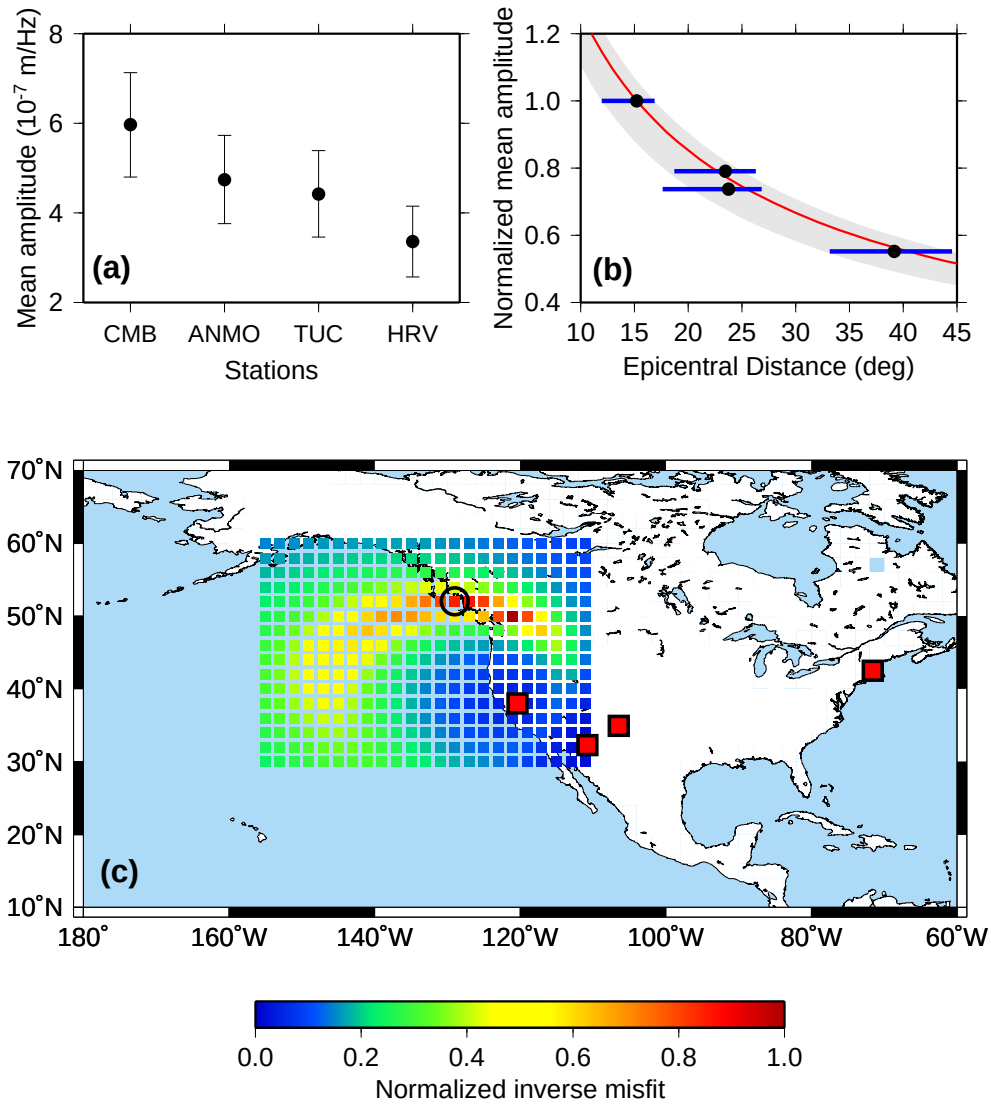

Figure 3.7: (a) Mean amplitude estimates and corresponding errors at stations considered in Figure 3.6. Error is estimated by random perturbation of time (± 6 hour) and period (± 30 s) window used for averaging. (b) Normalized observed mean amplitudes (black dots) and the theoretical attenuation curve (red) for the seismic source location indicated by a circle in (c). Grey shaded region and horizontal blue bars indicate the possible range of theoretical attenuation curves and epicenters from stations to possible source locations giving the good fit (i.e., normalized inverse misfit > 0.7). (c) Results of grid search for the location of the source of PSD noise highlighted in Figure 3.6. The PSD amplitudes were corrected for attenuation and geometrical spreading. The color scale represents the normalized inverse of the misfit between observed and predicted amplitudes (this way, the minimum misfit is always equal to 1). The circle indicates the off-shore location with small misfit.

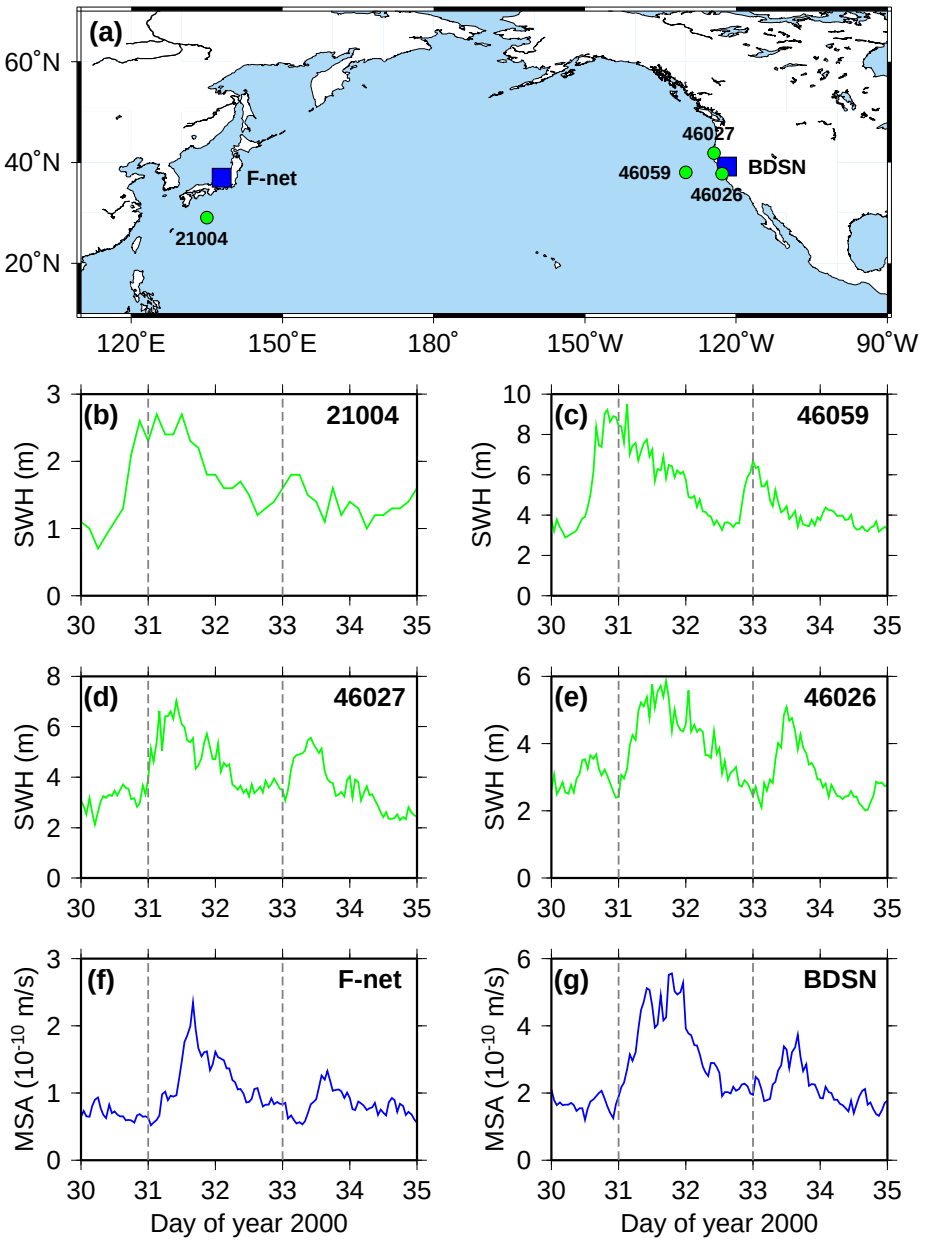

Figure 3.8: (a) Location of the two seismic arrays (blue squares) and ocean buoys (green dots). (b) Significant wave height recorded at buoy 21004. (c-e) Same as (b) for buoys 44059, 46027, and 46026. (f) Maximum stack amplitude (MSA) gaussian filtered with center period of 240 s recorded at F-net. (g) Same as (f) for BDSN. Peaks in ocean wave data at off-shore buoys (21004 and 46059) arrive earlier than seismic peaks. Arrival times of seismic energy are closer to those of the ocean wave peaks at buoys near the coast (46027 and 46026) for BDSN.

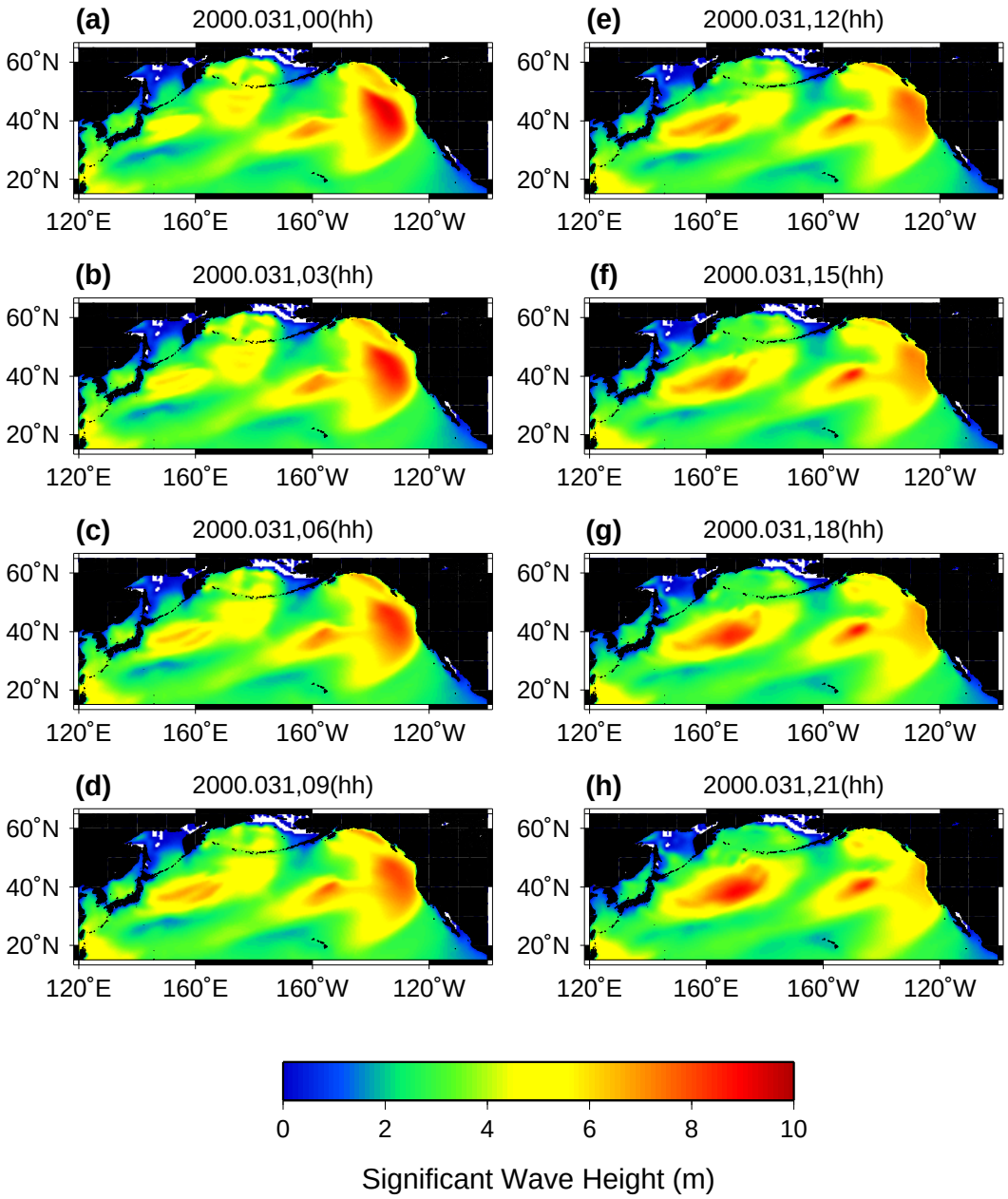

Figure 3.9: Significant wave height map on Jan. 31 in 2000 for the north Pacific ocean, based on WAVEWATCH III.(a-h) different time windows from 0 to 21 hour with 3 hour interval.

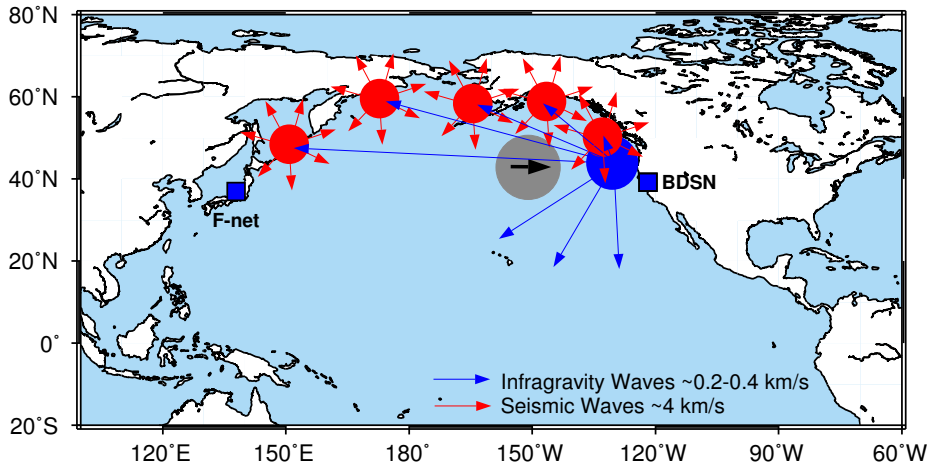

Figure 3.10: A schematic plot of the mechanism of conversion of energy from storm related ocean surface waves to seismic waves. Gray circle indicates the moving storm and blue and red circles (arrows) represent the source regions (radiation) of infragravity and seismic waves, respectively.

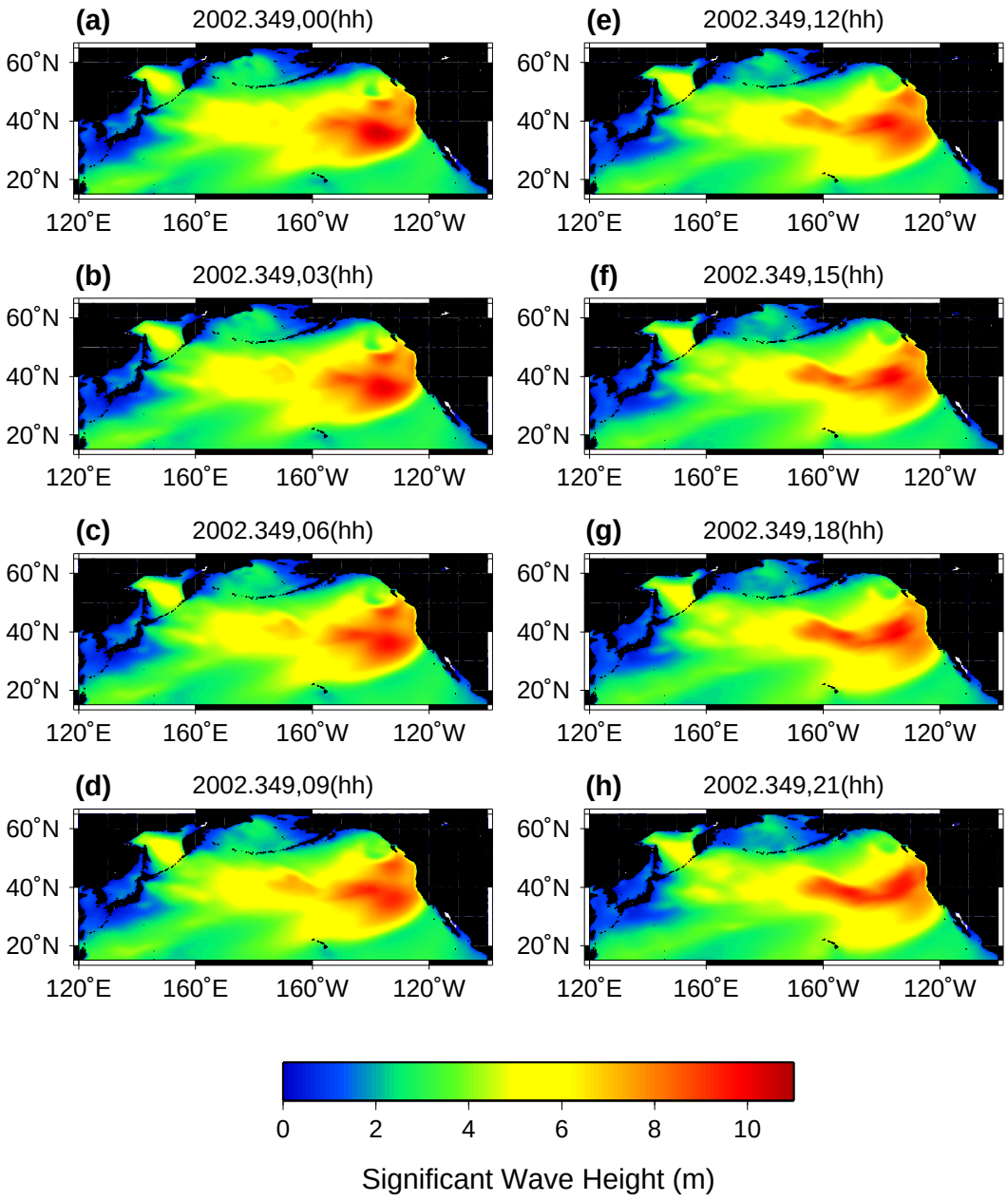

Figure 3.11: Significant wave height map on Dec. 15 in 2002 based on WAVEWATCH III.(a-h) different time windows from 0 to 21 hour with 3 hour interval.

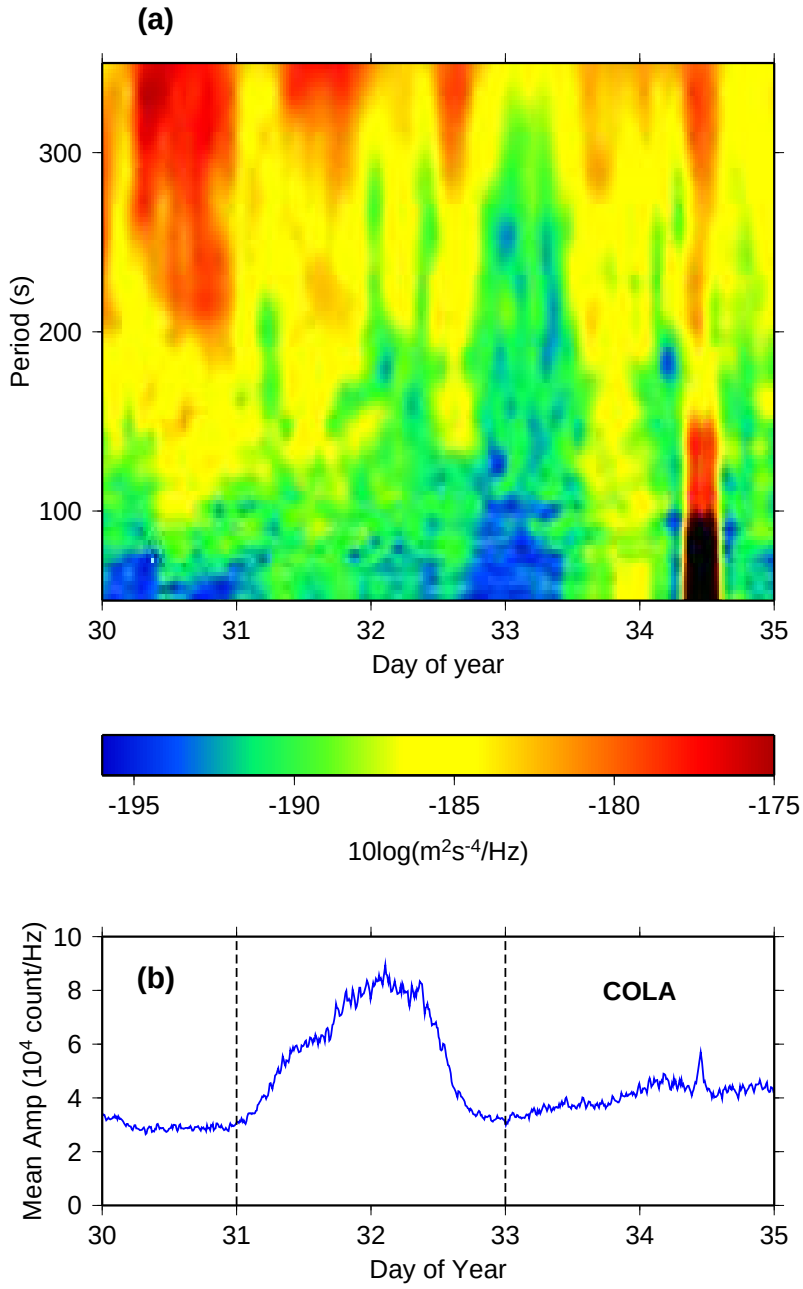

Figure 3.12: (a) Power spectral density (PSD) at COLA in Alaska. (b) Mean fourier amplitude in the period 2-25 s for COLA.

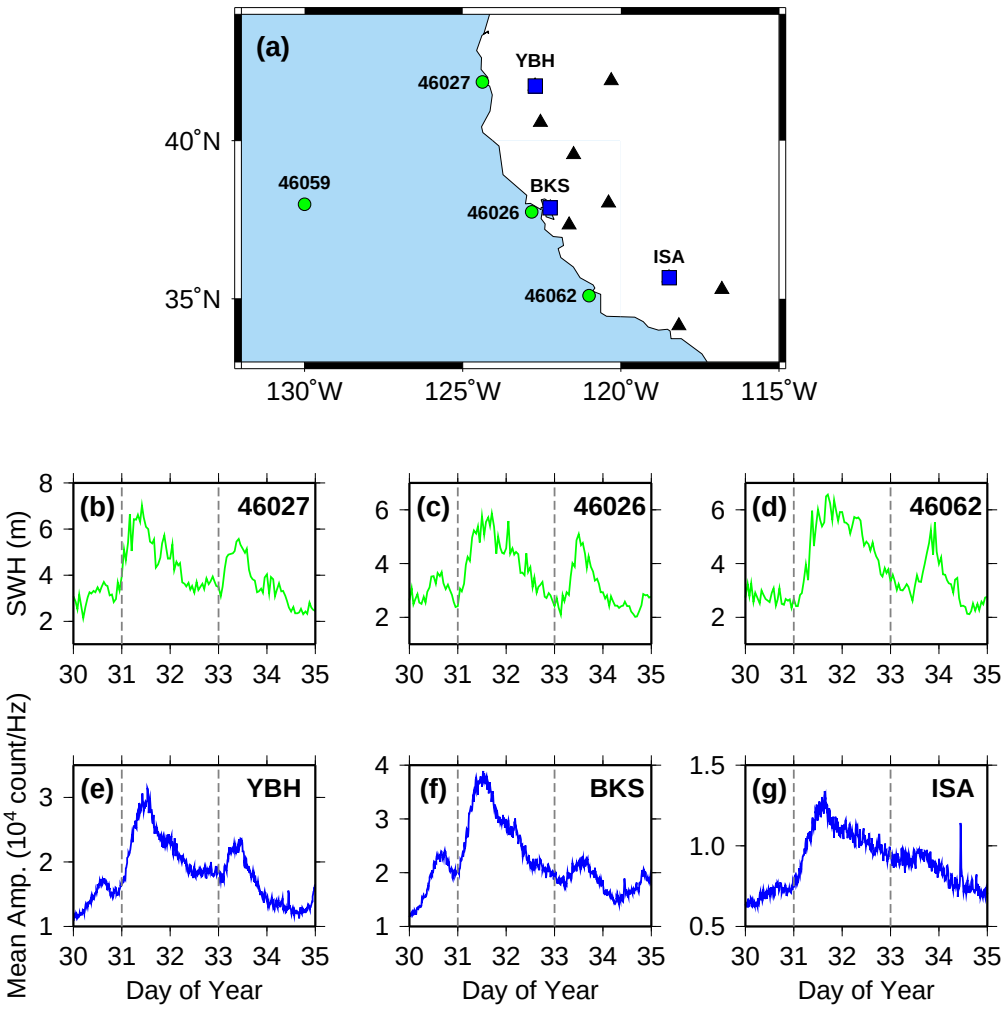

Figure 3.13: (a) Location map of BDSN and TerraScope stations (black triangle and blue squares) and buoys (green dots). Blue squares are seismic stations closest to the corresponding buoys. (b-d) Significant wave heights measured at buoy 46027, 46026, and 46052, respectively. (e-g) Mean Fourier amplitude (count/Hz) over period range 2-25 s for YBH, BKS, and ISA.

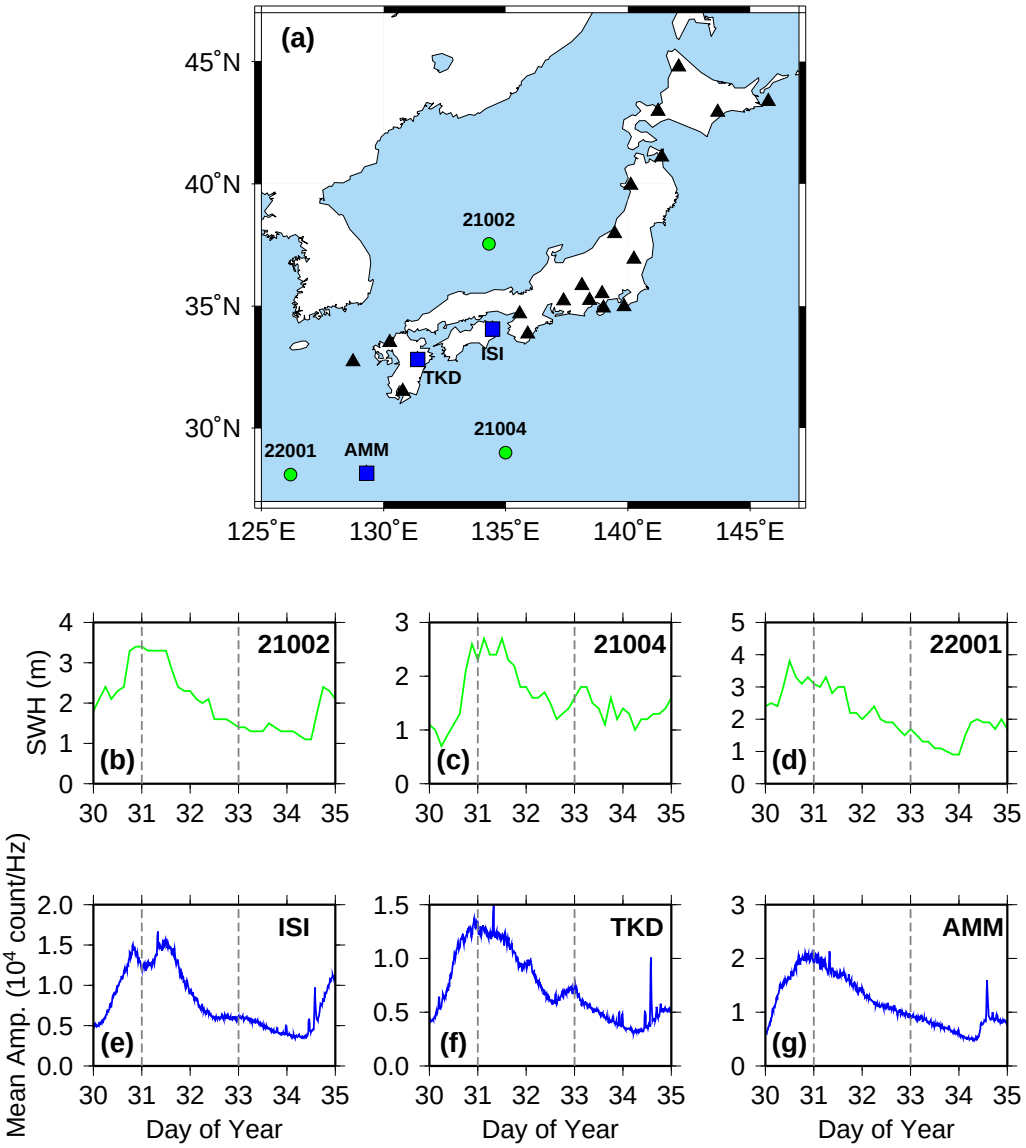

Figure 3.14: (a) Same as Figure 3.13 for F-net. (b-d) Same as Figures 3.13b, 3.13c, and 3.13d for 21002, 21004, and 22001, respectively. (e-g) Same as Figures 3.13e, 3.13f, and 3.13g for ISI, TKD, and AMM.

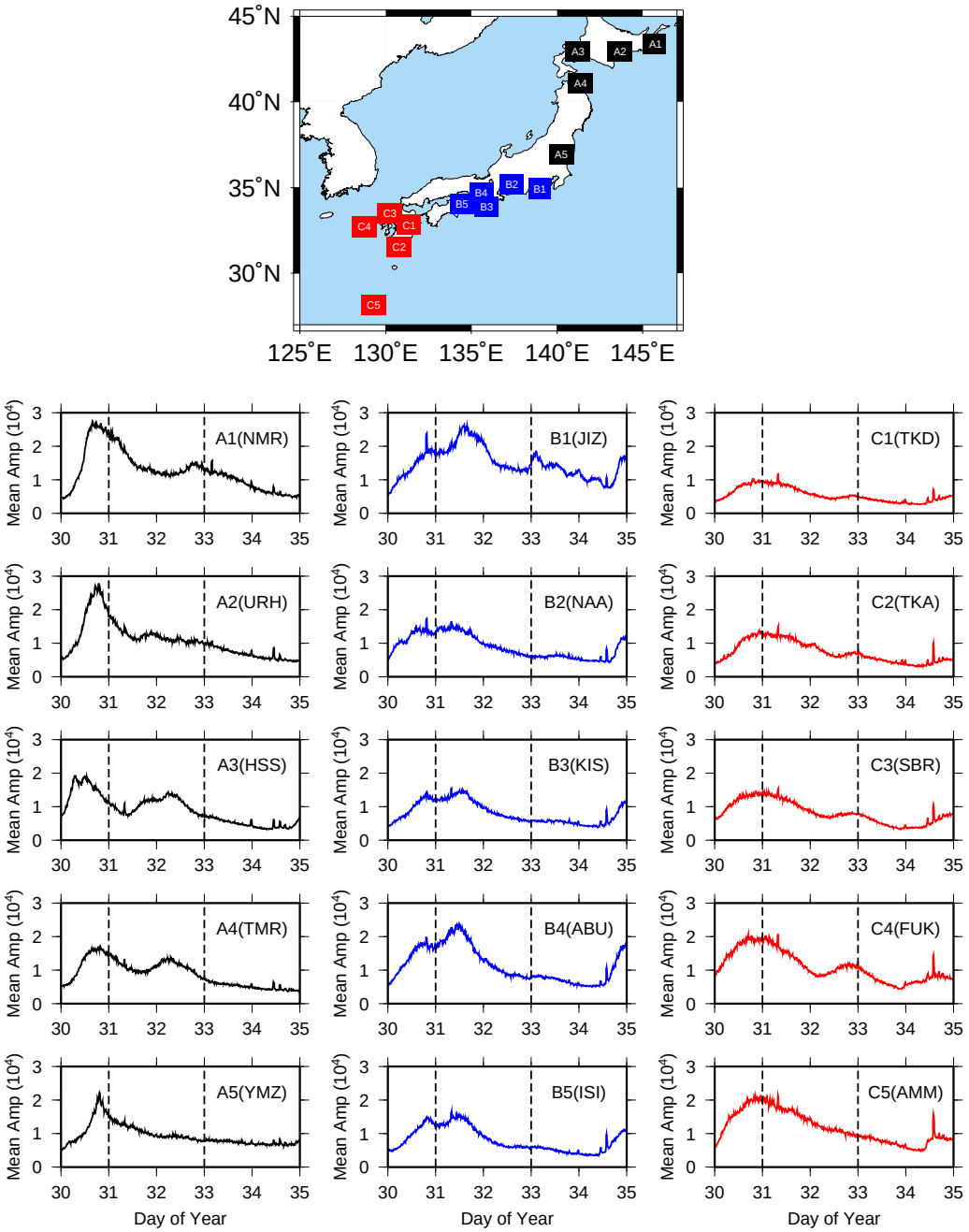

Figure 3.15: Location map of seismic stations grouped by their locations in F-net. (Top). Mean Fourier amplitude (count/Hz) over the period range 2-25 s for five stations shown on the map at the top in black (left column), in blue (middle column) and in red (right column).

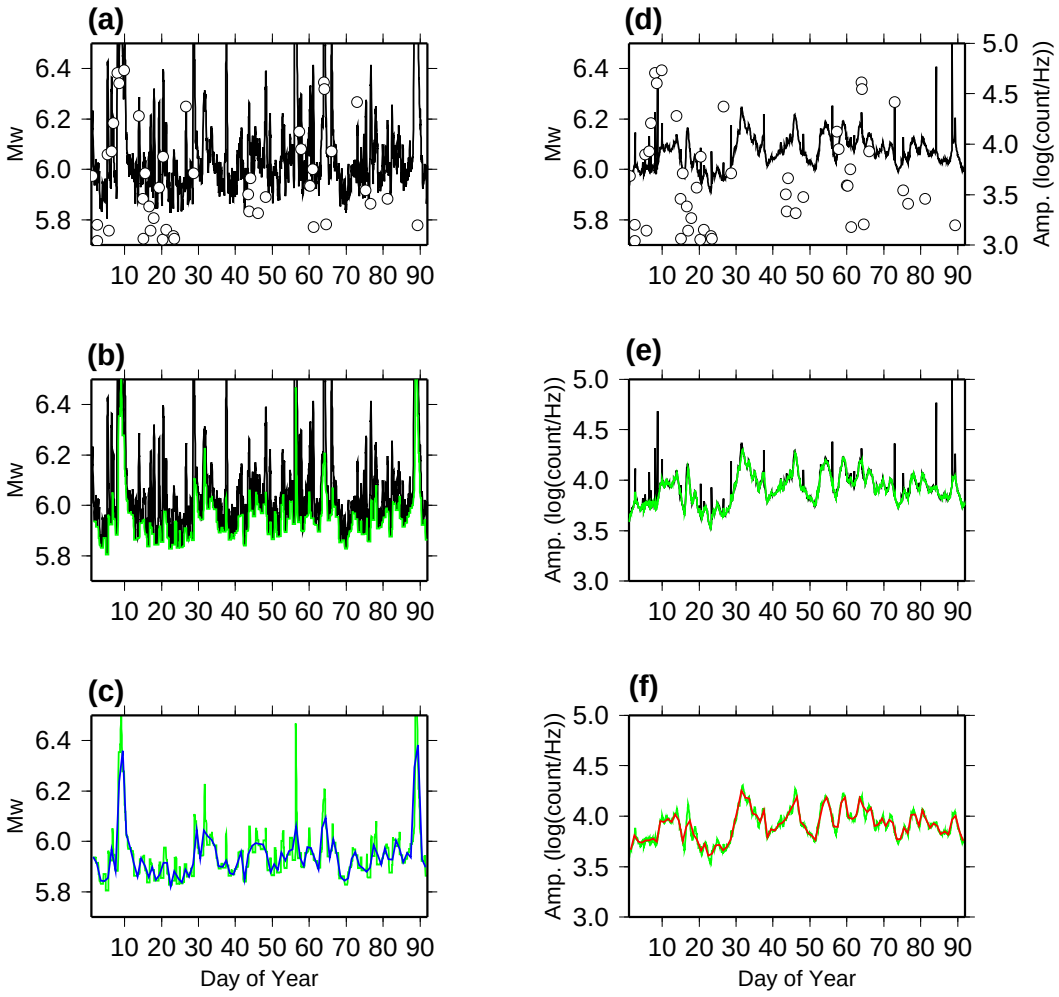

Figure 3.16: (a) Scaled long period MSA, gaussian filtered with center period of 240 s (black curve) for BDSN. Circles indicate earthquakes. (b) Black curve: same as in (a). Green curve: minimum obtained after applying moving time window with duration of 1.5 days and 6 hour shift. (c) Green curve: same as in (b). Blue curve: after low pass filtering with corner period of 1 day. (d) Mean Fourier amplitude over the microseismic band (2-25 s) averaged over 7 BDSN stations (black curve). Dots are earthquakes as in (a). (e) Black curve: same as in (d); Green curve: after removing large gradient peaks. (f) Green curve: same as in (e); red curve: low pass filtered with corner period of 1 day.

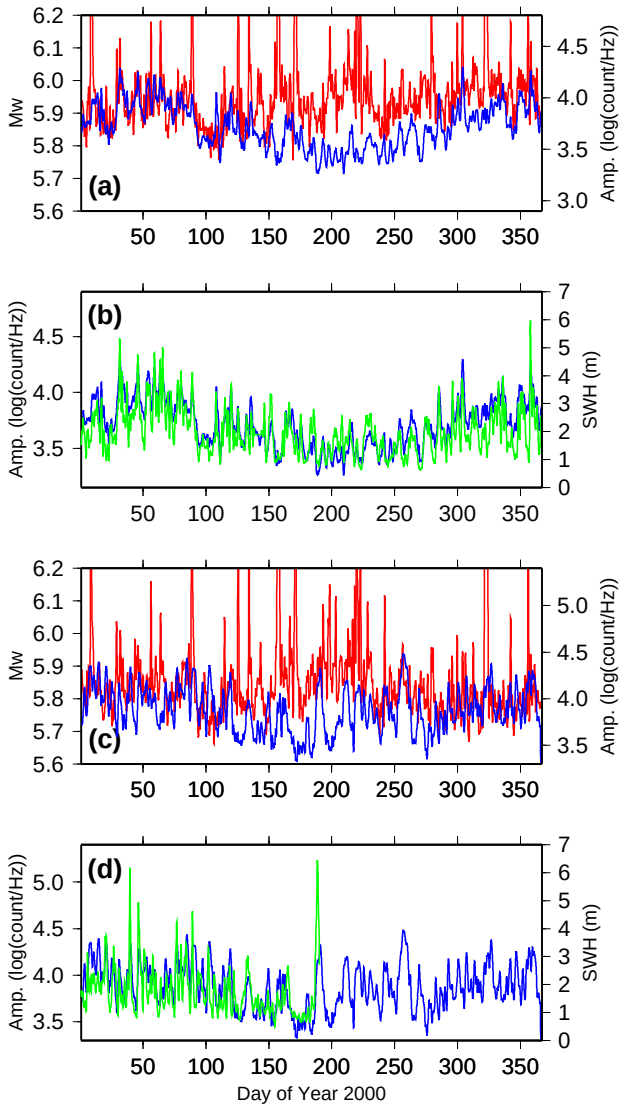

Figure 3.17: (a) Scaled long period MSA (red) and short period Fourier amplitude (blue), preprocessed as shown in Figure 3.16, for BDSN. The short period mean Fourier amplitude was computed from 7 BDSN stations (BKS, CMB, MHC, MOD, ORV, WDC and YBH). (b) Preprocessed short period mean Fourier amplitudes (blue) for BDSN and significant wave height measured at buoy 46026 (green). The correlation coefficient between the two curves is 0.81. (c) Same as (a) for 5 F-net stations near the eastern coast of Japan (AMM, ISI, NMR, TKD, and TMR). (d) Same as (b) for F-net. Significant wave height data measured at buoy 21004 (green) is not available after day 190 in 2000. Large peaks in short period mean Fourier amplitude and ocean waves during summer may be coming from the typhoon. The correlation coefficient between the two curves for the first part of the year is 0.58

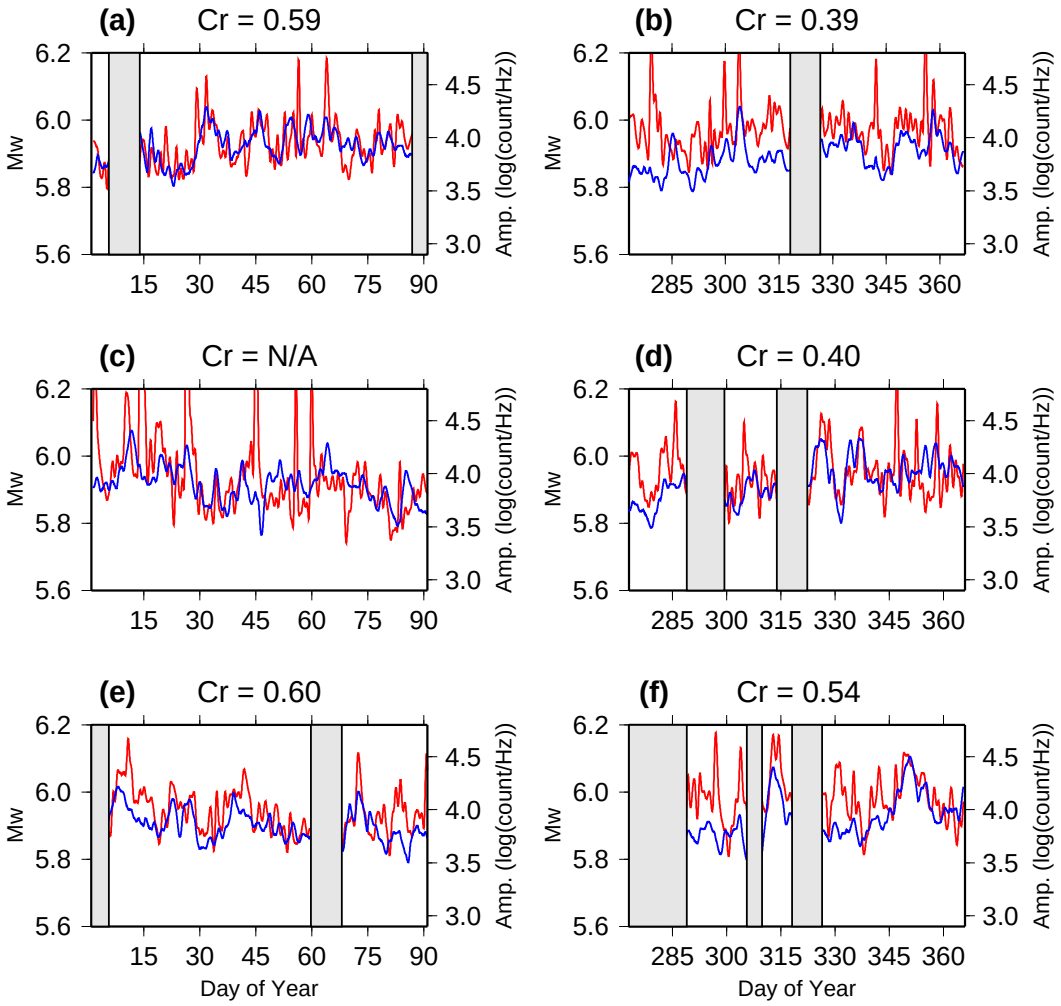

Figure 3.18: (a) Comparison between preprocessed scaled long period MSA (red) and short period mean Fourier amplitudes (blue) for the first three months of 2000. Time windows strongly contaminated by earthquakes are shaded in gray. Corresponding correlation coefficient is shown in the plot. (b) Same as (a) for the last three months in 2000. (c-d) Same as (a) and (b) for 2001. For (c), Correlation coefficient is not computed because of significant contamination from earthquakes throughout the time period considered. (e-f) Same as (a) and (b) for 2002.

Chapter 4

Joint slip inversion of the 2004 Sumatra-Andaman earthquake from long period global seismic waveforms and GPS static offsets

This chapter has been submitted to *Bull. Seismol. Soc. Am.* [*Rhie et al.*, 2006b] under the title 'Joint slip inversion of the 2004 Sumatra-Andaman earthquake from long period global seismic waveforms and GPS static offsets.'

Summary

The December 26, 2004 Great Sumatra-Andaman, earthquake opened a new era for seismologists to understand the complex source process of a great earthquake. This is the first event with moment magnitude greater than 9 since the deployment of high dynamic range broadband seismic and GPS sensors around the globe. This study

presents a thorough analysis of the ruptured fault plane geometry and slip distribution using long-period teleseismic data and GPS-measured static surface displacements near the fault plane. We employ a rupture geometry with six along-strike segments with and without a steeper down-dip extension, to simultaneously invert the global long-period (100-500s) seismic measurements and GPS deformation observations. The fault segments are further sub-divided into a total of 201 $\sim 30 \times 30$ km fault patches. Sensitivity tests of fault plane geometry and the variation in rupture velocity indicate that the dip and curvature of the fault plane are not well resolved from the given data set and the rupture velocity is constrained between 1.8 and 2.6 km/s. Error estimations of the slip distribution using a Jack-knife test of seismic station subsets illustrate that slip is well resolved along the whole rupture and slip uncertainties are less than 23 %. While it is possible that near-field GPS data include contributions from additional postseismic transient deformation, our preferred model suggests that the Sumatra-Andaman earthquake had a magnitude of M_w 9.25 +0.022 / -0.024.

4.1 Introduction

The great M_w 9.0 Sumatra-Andaman earthquake occurred on 26 December, 2004 in the subduction zone west of the island of Sumatra in Indonesia rupturing northward for about 1500 km along the Nicobar -Andaman island chain. This event is the third largest of the four $M_w > 9$ events since 1900. It is the first great event with data sufficient to allow for a detailed analysis of its complex source rupture process. For the first time, global very broadband seismic and geodetic measurements are available. Several slip and rupture propagation models have been estimated from short period P waveforms [*Ishii et al.*, 2005; *Krüger and Ohrnberger*, 2005; *Lomax*, 2005; *Ni et al.*, 2005], hydroacoustic T-phase data [*de Groot-Hedlin*, 2005; *Tolstoy and Bohnenstiehl*, 2005], long-period normal modes [*Park et al.*, 2005; *Stein and Okal*, 2005], long period

waveforms [*Tsai et al.*, 2005], broad band seismic waveforms [*Ammon et al.*, 2005; *Lay et al.*, 2005] and geodetic data [*Banerjee et al.*, 2005; *Subarya et al.*, 2006; *Vigny et al.*, 2005]. In this paper we jointly invert the long-period teleseismic waveform data and horizontal static surface offsets from campaign-mode and continuous GPS observations in the near-field region of the event for the coseismic slip distribution and perform a thorough sensitivity and error analysis of fault geometry, slip distribution, and kinematic rupture parameters.

4.2 Data and inversion method

We considered 30 displacement waveforms recorded at 10 stations (Figure 4.1). The epicentral distances, measured from the USGS epicenter (95.96E, 3.30N) to the 10 stations range from 43.6° (AAK) to 65.2° (TAU). The 10 stations were selected by considering signal-to-noise and azimuthal coverage qualities of three-component waveforms for a 15000 s time window from the origin time. The data and theoretical Green's functions were bandpass filtered between 100 and 500 sec. We computed theoretical Green's functions for 0.2° intervals in distance and 5 km intervals in depth by the normal mode summation method for model PREM [*Dziewonski and Anderson,* 1981]. Since PREM is a very good average 1D model for long-period seismic waveforms, we didn't take into account any 3D wave propagation effects on our Green's function computation.

The GPS data used for the inversion represent a 38-station near-field subset of the 142 coseismic surface displacements measured by continuous and campaign-mode GPS stations reported by *Banerjee et al.* [2006]. We focus on the near-field horizontal geodetic data, including campaign and continuous GPS measurements on the Sumatra, Nicobar and Andaman Islands from within 300 km of the trench and between 4°N to 14°N. In this dataset the offset estimates for near-field campaign-mode GPS sites

were adjusted using an after-slip model to account for several weeks of postseismic deformation prior to reoccupation of the GPS stations [*Banerjee et al.*, 2006; their Tables S-3 and S-4].

To invert data for the slip distribution, we use a non-negative, least-squares inversion method, which has been widely applied for source studies using local or regional seismic and/or geodetic data set [e.g., *Hartzell and Heaton*, 1983; *Dreger and Kaverina*, 2000; *Kaverina et al.*, 2002]. We invert for seismic moment over a grid of point sources predefined over fixed fault planes and then the slip distribution is derived from the obtained moment distribution by dividing by the area of the corresponding sub-faults and the elastic rigidity derived from an average of the PREM model from the surface to 30 km depth (4.0×10^{11} $dyne/cm^2$). Since we are inverting long-period data, the detailed variation in slip rise time of each grid point is ignored. At the periods used the slip rise time is essentially an impulse. The trigger time of each grid point is defined by the passage of the circular rupture front with constant rupture velocity over one fault segment. There is a broad range (1.8 - 2.6 km/s) of rupture velocity that fits the seismic waveform data we used. We choose the value of 2.5 km/s as it is consistent with the T-phase [*Tolstoy and Bohnenstiehl*, 2005] and short-period P-wave observations [*Ni et al.*, 2005; *Krüger and Ohrnberger*, 2005]. For multiple-segment fault models, initial points of the rupture front on each segment account for the transit times across previous segments with respect to the origin time. For the current geodetic inversion, we assume a half-space model and use Okada's dislocation formula [*Okada*, 1985] for the static-offset Green's function.

Banerjee et al. (2005) find that both the Earth's spherical structure and depth-varying rigidity structure can greatly affect predicted surface displacements from an event of the magnitude and dimension of the Sumatra earthquake, putting into question the use of commonly employed half-space models. The resultant bias is greatest at large (> 500 km) distances (see Figure 11 in *Banerjee et al.*, 2006), but effects of sphericity and layering partly cancel each other at even greater distances. By using only near-field displacements and a homogeneous half-space model we limit the im-

pact of these assumptions on our inversions. A Laplacian-smoothing operator and slip positivity constraint are applied in all of the inversions. For the joint inversion, a weighting factor is applied to give relative weights to geodetic and seismic data sets.

4.3 Distributed slip models inverted from seismic and geodetic data

We test two fault geometry models. Geometry Model A is obtained from the previous study of *Banerjee et al.*, [2005] and Model B is slightly modified from Model A in which the deeper, steeper segments of the fault were removed (small panels in Figure 4.2a and 4.2b). Model A consists of 12 fault segments with 6 segments along the trench-parallel direction and 2 down-dip segments. This fault geometry takes increasing dip angles with depth into consideration. Geometry Model B consists of 6 segments. Each segment in this model has the same upper-edge location, strike, dip and length parameters as the upper segments of Model A, but the down-dip width is increased by 20 to 33 % to maintain the total width of Model A. Thus, the dip angles of the segments are constant with depth for Model B. Each segment of the fault model is divided into many sub-faults with length and width of around 30 km for the inversion. The total number of sub-faults is 201. This level of sub-fault discretization corresponds to the lower cutoff period of the seismic waveform data with respect to seismic wave velocity and the range of rupture velocity. It also produces a smooth kinematic rupture model in the passband employed. The rake is allowed to vary within the range from 40° to 150° with respect to the strike.

We invert seismic waveforms for the slip distribution on the two geometry models by using the inversion method described in the previous section. We name the slip models depending on the choice of fault geometry and inclusion of the seismic and/or

GPS data. Slip model AS refers to the model inverted from seismic data only over geometry A, the slip model on geometry A from only GPS data is model AG, and model BJ indicates a slip model for geometry model B derived from the joint inversion of seismic and GPS data.

We find that the slip distributions on the two different fault geometries, using only long-period seismic waveform data (slip models AS and BS), are very similar (Figure 4.2). In Figure 4.2, both slip models AS and BS show large slip patches at around 4°N and a high-slip region with slip larger than 5 m is extending only up to 10°N. There is no evidence of substantial slip on the northern fault segments. Slip near the hypocenter is small compared to the largest slip further to the north. The rake changes from south to north. On the southern segment (2°N - 5°N), the slip direction is nearly pure dip slip. However, it becomes more oblique (reverse plus right-lateral) on the next two northern segments (5°N - 10°N). The primary difference between the two slip models is the smaller slip on the deeper, steeper segments of slip model A. The moment magnitudes of slip model A and B are 9.05 (4.636×10^{29} dyne-cm) and 9.09 (5.355×10^{29} dyne-cm), respectively.

The seismic variance reductions for the given slip models show that the vertical and radial components are more or less constant with azimuth (different stations), but tangential variance reductions vary significantly with azimuth. The comparison between the trend of tangential variance reduction and the SH radiation pattern based on the Harvard CMT solution shows a correlation with minima in CMT SH radiation and level of fit to the waveforms from the finite-source rupture models (Figure 4.2c and 4.2d). This indicates that the observed waveforms at stations located near radiation nodes contain significant 3D wave propagation effects due to heterogeneity, focusing and defocusing. The comparison of synthetic and observed seismic waveforms show that synthetic waveforms underestimate observed waveforms near SH nodes (e.g., KIV, CAN, and TAU) for the tangential component, whereas the synthetics for radial and vertical components fit the corresponding observations well (Figure 4.3).

To better constrain the slip distribution we added geodetic static offset data. To combine the two data sets we performed a sensitivity analysis of the relative weight of the two with respect to the level of fit. An optimal weight was found that resulted in nearly maximum levels of fit to the two independent data sets. This process is illustrated in Figure 4.4. For the joint inversion of seismic waveforms and GPS, the trends of the two variance-reduction curves clearly show trade-offs. As we increase the weighting to GPS data, the seismic variance reduction decreases and GPS variance reduction increases. From the tradeoff curves (Figure 4.4), we choose a weighting factor of 4.0×10^{-9} having large variance reductions of seismic and GPS for both geometries and then take those slip models as the joint-inversion models AJ and BJ. It is possible to perform inversions with relative data weighting that maximize the fit to the GPS data the weighting factor was increased by a factor of 25. For the given weighting factor, the GPS variance reductions for model AG and BG are 99.8 and 99.9 % and the seismic variance reductions are -30.8 and -9.6%. Seismic moments for slip model AJ, BJ, AG and BG are 8.905×10^{29}, 8.808×10^{29}, 1.003×10^{30}, and 9.668×10^{29} dyne-cm, respectively. These values are larger than the corresponding moments from models using only seismic data by a factor of nearly two.

To evaluate the differences among slip models from the different datasets we plot changes in moment density with latitude (Figure 4.5a and 4.6a). Moment density is defined as released moment per km along strike from south to north. The trends of moment density for model AJ and BJ are similar to the seismic slip models but the magnitudes of joint slip models are substantially higher than the seismic models. The joint slip models and slip models from GPS only show significant moment release around the epicenter. The joint and GPS slip models differ in that GPS model show larger moment released on the southern (around 2°N), central (5° - 10°N) and northern most (around 12.5°N) part of the fault but less moment release near the maximum found in the joint inversions (3° - 5°N) (Figures 4.5a and 4.6a). The total seismic variance reductions are 55.10 (slip model AJ) and 57.90 (slip model BJ), which are decreased by 11.1 and 8.8 % from those obtained in the seismic-waveform-only inversions (Figure 4.5b and 4.6b). However their GPS variance reductions are 94.14

and 95.95 %, which are increased by 40.35 and 32.5 % from GPS variance reductions computed from slip model AS and BS, respectively. The detailed variation in seismic variance reductions for the three components show that, for the radial and vertical components, the variance reductions are more or less consistent with those for slip models AS and BS but the tangential variance reduction has more significant minima near the two SH nodes at around 140 and 320 deg. This appears reasonable because waveforms close to the radiation node are more sensitive to the small change in slip distribution. The modeled GPS offsets for slip models AJ and BJ underestimate the GPS offsets over the fault plane but slightly overestimate GPS measurements over northern Sumatra (Figure 4.5c-d and 4.6c-d).

4.4 Sensitivity tests for dip angle and rupture velocity

To constrain key model parameters, we consider sensitivity tests for dip angle and rupture velocity. Both parameters are important in the estimation of moment magnitude and final slip distribution. First, we test a series of dip angles that were jointly varied for all segments in geometry model B. Repeated inversions with changes in dip over a range of +/- 8° from the starting model show that the variance reduction is slowly decreasing as dip angles are increasing (Figure 4.7a). However, we find a systematic increase in moment magnitude with decreasing dip as had been previously documented (Figure 4.7b) [*Banerjee et al.*, 2005]. Although the sensitivity test for dip angle indicates that a shallower rupture plane leads to an improved fit of the teleseismic waveforms when it is jointly constrained with near horizontal static offsets, we still prefer the fault geometry model with unperturbed dip angles because this fault geometry is compatible with the distribution of aftershocks [*Lay et al.*, 2005; *Bilham et al.*, 2005; Their figure 6].

Second, we test seismic and GPS variance reduction as a function of rupture velocity (Figures 4.7c and 4.7d). We consider joint inversions of the three-component seismic waveforms and the GPS data and seismic-only inversions for geometry model A and B. For both geometries, variations in seismic variance reductions show high values over the range from 1.8 to 2.8 km/s. The GPS variances are nearly flat over the range of 1.0 to 2.8 km/s, but drop off to slightly lower values as higher rupture velocities are chosen in the joint inversion. This suggests that the data set we used is not very sensitive to the rupture velocity over the fault plane. The seismic variance reduction from seismic-only inversions show a similar trend as for the joint inversion, whereas the forward prediction of GPS variance reductions from the seismic-only inversion have a relatively sharp peak at around 2.5 km/s (Figure 4.7d). This indicates that the slip distribution obtained from seismic data using a 2.5 km/s rupture velocity can explain the near-field static offsets relatively well. Although our sensitivity test did not give us an optimal rupture velocity, we believe that 2.5 km/s rupture velocity is reasonable based on forward GPS computation and also independent previous estimations based on different datasets [*Ammon et al.*, 2005; *Krüger and Ohrnberger*, 2005; *Ni et al.*, 2005; *Tolstoy and Bohnenstiehl*, 2005]. As the seismic and geodetic data we consider do not provide good constraints on either the dip or the propagation velocity of the rupture, it is important to incorporate independent determinations of these parameters from other studies [e.g., *Bilham et al.*, 2005; *Ishii et al.*, 2005; *Tolstoy et al.*, 2005]

4.5 Error analysis using Jackknife method

A proper estimate of model error is as important as getting a very detailed slip distribution. However, it is not easy to conduct a complete error analysis for slip distribution models since many factors contribute, such as the assumed velocity model or the station geometry. Here we investigate the variability in recovered slip due to

the choice of which stations are used in the inversion. In this Jackknife method [*Efron and Tibshirani*, 1993] we select all possible subsets of 8 seismic stations (24 waveforms) out of 10 stations and invert them for slip distribution with the fixed geodetic constraints. By doing this, we obtain 45 slip distribution models from which the mean and standard deviation of the slip was computed (Figures 4.8 and 4.9). The mean slip distributions are very close to the corresponding slip models from all seismic waveforms and the GPS data. The estimates of seismic moment (M0) and 1 standard deviation errors are $8.924 \pm 0.098 \times 10^{29}$ (M_w = 9.24 -0.003/+0.003) and $8.793 \pm 0.085 \times 10^{29}$ (M_w 9.23 -0.003/+0.003) for slip model AJ and BJ, respectively. The uncertainty of slip at each sub-fault is computed by taking 1 standard deviation in percentage. Here, small slip (less than 20 % of maximum slip) is ignored in the computation of slip uncertainty. The maximum and mean slip errors for model AJ and BJ are about 23 % and 6 %. This indicates that our slip distribution is very stable with respect to the choice of seismic stations. For both slip model AJ and BJ, maximum uncertainty occurs near the surface of southern segments near 3°N.

4.6 Discussion and conclusions

We invert long-period global seismic waveforms and static horizontal GPS offsets for the slip distribution of the 2004 Sumatra-Andaman event. The results show the mean total seismic moment inferred from the joint inversion of long-period seismic waveforms and near-field static offsets from GPS observations on the Sumatra, Nicobar, and Andaman islands is 9.25 (from model AJ, BJ, AG and BG), significantly larger than the estimate from seismic data alone, by 0.15 or 0.2 magnitude units depending on the fault geometry. The estimate of M_w 9.2 for this model is consistent with that obtained by *Banerjee et al.*, [2005], *Banerjee et al.*, [2006], and *Vigny et al.*, [2005] using only GPS data. The discrepancy between models using seismic only and joint

data sets indicates that there may be significant slip that cannot be detected from the seismic waveforms in the period range between 100 and 500 sec. To explain this moment magnitude difference, we need approximately 3-4 meter of additional slip on nearly the whole fault surface, which corresponds to an increase of 56% of the average slip of the seismic-only models. The near-field coseismic GPS offset estimates of *Banerjee et al.* [2006] include a correction for afterslip based on an inversion of available continuous GPS displacements from between the time of the earthquake and the GPS campaign observations. However, it is possible that some additional afterslip affecting some of the near-field sites is not captured in this model. *Vigny et al.* [2005] show from epoch-by-epoch analysis of the first few hours of GPS time series, that the event did not involve significant continued slow slip, which had been suggested by *Stein and Okal* [2005] to explain systematic increases of moment estimates with period considered.

We compare predicted static offsets from the forward computations of the slip models we derived (Figure 4.10). Since our GPS subset is restricted to near-field stations, we test if our slip model can explain relatively far-field GPS offsets on the Malaysian Peninsula, which are used in previous geodetic slip inversions [*Subarya et al.*, 2006; *Vigny et al.*, 2005]. *Subarya et al.* [2005] examined both layered and homogeneous half-space models, whereas Vigny et al. [2005] relied on elastic half-space calculations. The forward GPS prediction for model AS (not in figure) and BS, which significantly underestimate the near-field GPS observations (Figure 4.10a), fit the far-field offsets, whereas Model AJ and AG, which are optimized to fit the near-field GPS offsets (Figures 4.5c, 4.5e, 4.6c, and 4.6e), clearly overestimate the GPS observations over the Malaysian Peninsula (Figures 4.10c and 4.10d). This discrepancy mainly comes from our use of the over-simplified half-space model [*Banerjee et al.*, 2006, see their Figure 11]. *Banerjee et al.* [2006] showed that a half-space model would overestimate the GPS offsets on the Malaysian Peninsula by a factor of 2 for a given Sumatra slip model. It is important to note however, that many of the GPS measurements we utilize are located very close to the fault plane, and could contain significant residual amounts of post-seismic displacement (or slip related to processes with durations

longer than the seismic period used in this study) and may also be sensitive to slip and geometric heterogeneities not captured by our models.

We test two different fault geometry models with varying and constant dip angles. The results of this test indicate that the frequency range of our data set is too low to independently resolve the increasing dip of the plate interface with depth. *Banerjee et al.* [2005, 2006] find that slip on steeper dipping segments at depth below portions of the rupture improve the fit to the GPS deformation data, especially in the vertical component. Our investigation of the sensitivity of the obtained slip models to geometry, rupture velocity, as well as seismic station distribution (Jackknife) methods indicate that the joint-inversion models for the two possible fault geometries are well constrained, where maximum deviations are on average less than 6% of mean sub-fault slip. The maximum slip is near 4°N and the high-slip region extends up to 10°N. Over this length of the fault the standard deviation of sub-fault slip is also in the 6% range, and this slip was found to largely control the fit to the seismic waveform data. The largest slip patch, just west of the northern tip of Sumatra is consistent with one of the tsunami source regions found by *Fine et al.* [2005], and the northward extent of significant slip in our joint-inversion models is consistent with the tsunamigenic regions proposed by *Lay et al.* [2005]. The general similarity of the GPS and seismic inversion results and the low level of model variance with station distribution indicates that if done rapidly finite-source inversions could contribute to tsunamic hazard estimation.

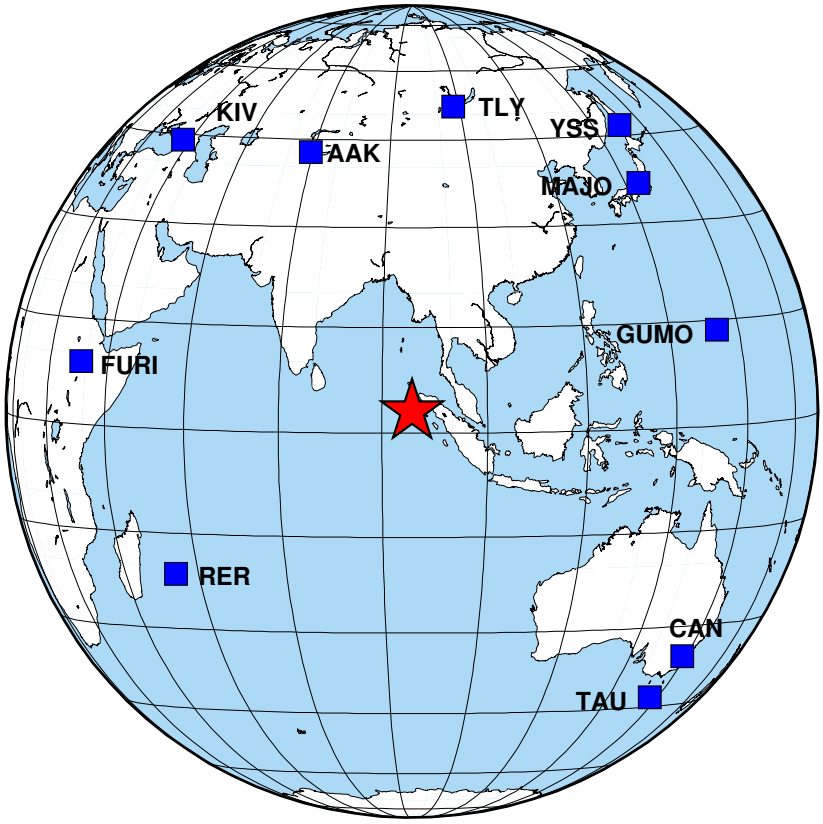

Figure 4.1: Location of seismic stations included in inversion. Epicenter is indicated with star.

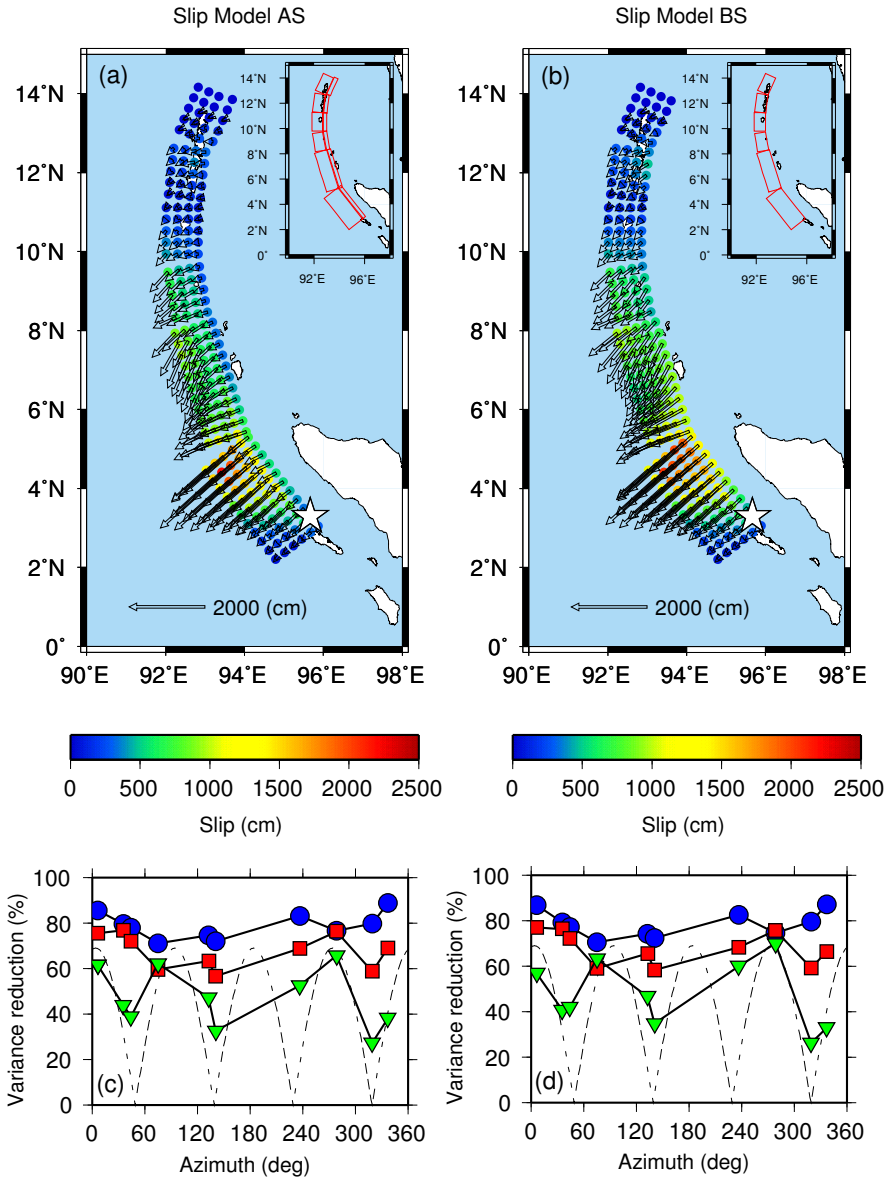

Figure 4.2: (a) Slip-distributed model from seismic inversion only (Model AS) over fault geometry model A. The fault geometry A (small panel) is obtained form previous work [*Banerjee et al.*, 2006]. A white star indicates the epicenter. Color represents total slip on sub-fault and corresponding arrow indicates the slip vector. (b) Same as (a) for fault geometry model B. The geometry of model B (small panel) is modified from model A and does not allow for changes in dip with depth. (c) Variance reduction at 10 seismic stations ordered by azimuth for slip model A. Vertical, radial and tangential variance reductions are plotted with blue circles, red squares, and green triangles, respectively. Dotted line show SH radiation pattern for Harvard CMT solution. Total variance reduction is 66.16%. (d) Same as (c) for slip model B. Total variance reduction is 66.69%.

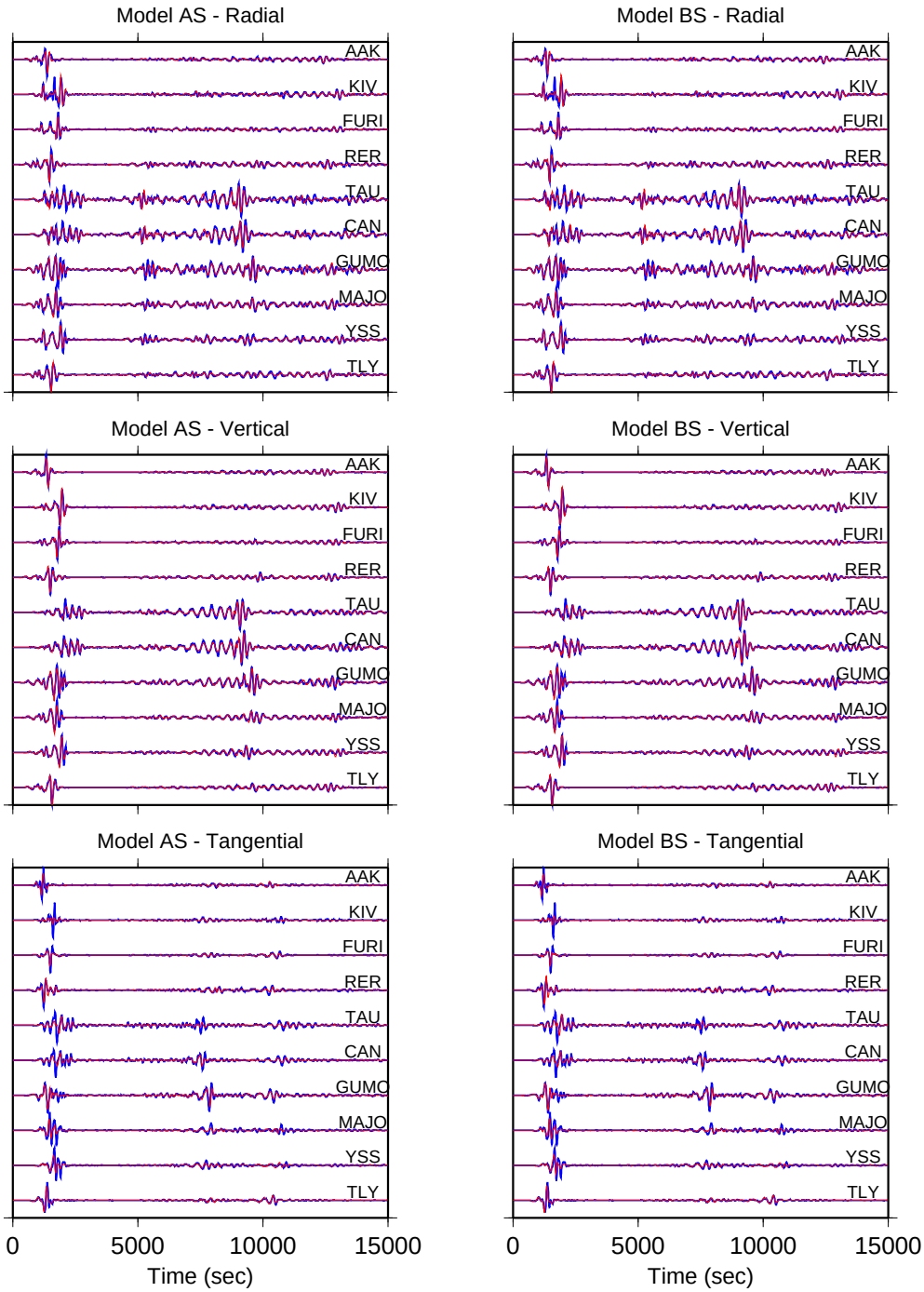

Figure 4.3: Comparison of 3 components synthetic (red) and observed (blue) seismic waveforms for 10 stations. Seismic waveforms are plotted in the order of azimuth from bottom to top.

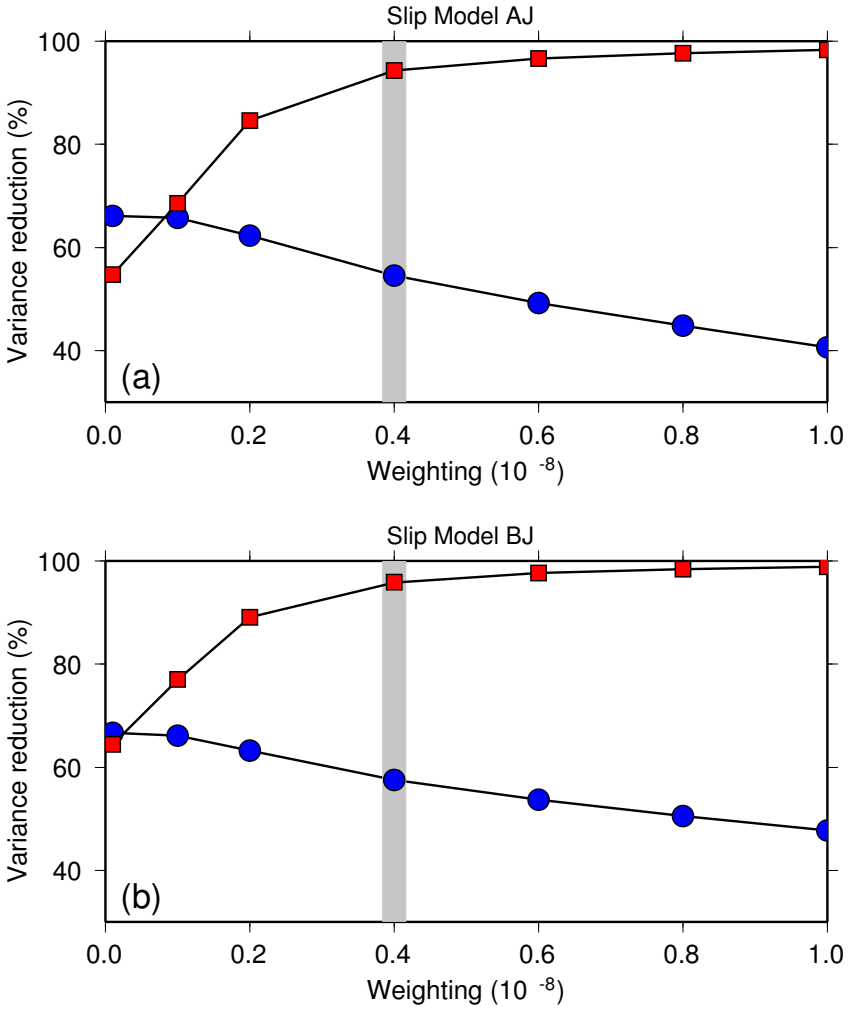

Figure 4.4: Weighting factor for seismic and geodetic joint inversion. Since the data sets are not individually normalized the relative weighting factor is a factor of 10^{-8}. The following tradeoff plots show that an optimum value can be found. (a) Variance reduction of seismic waveforms (circles) and GPS (squares) with weighting factor to GPS weighting for slip model AJ. The preferred weighting factor is highlighted with grey bar. (b) Same as (a) for slip model BJ.

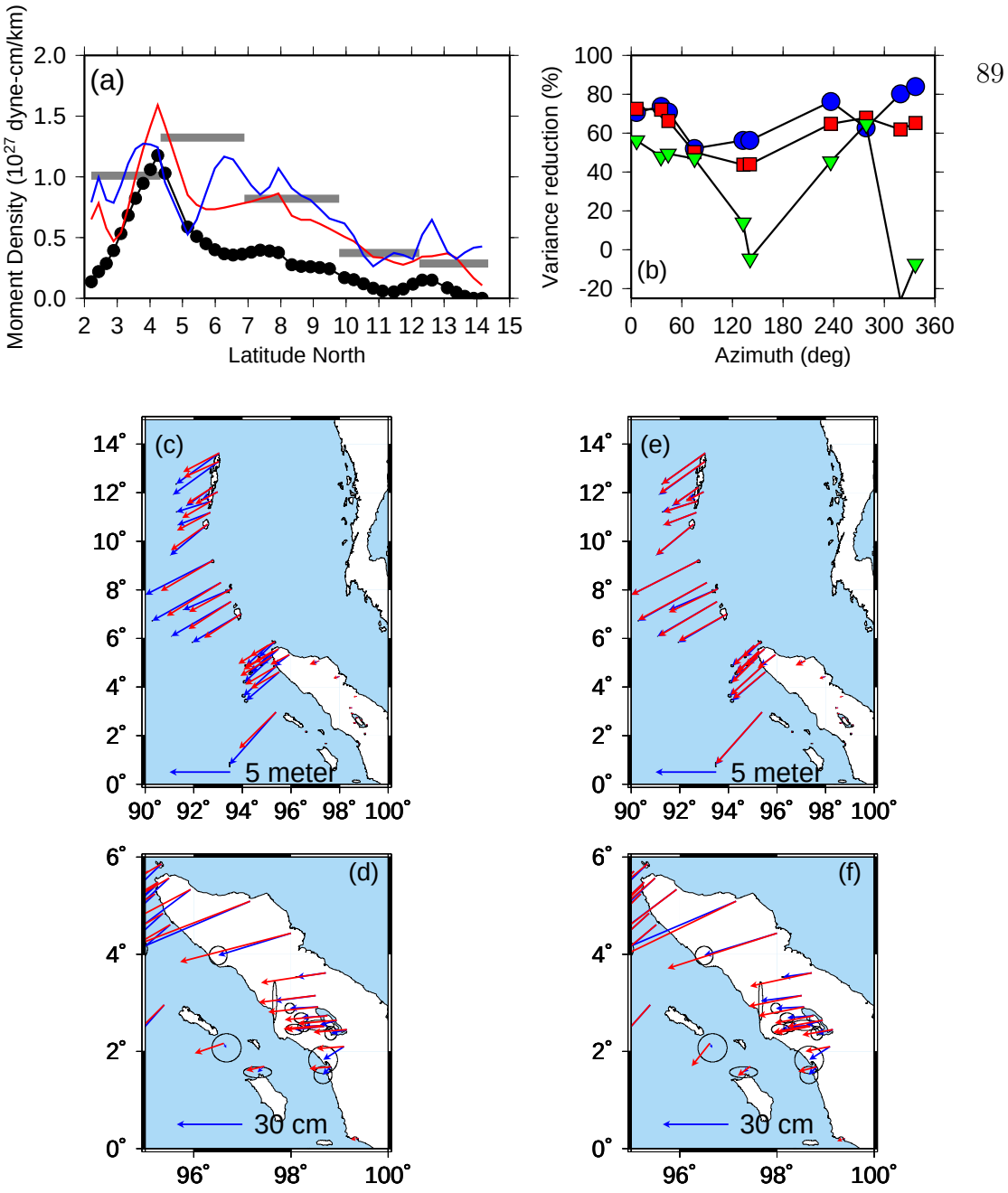

Figure 4.5: (a) Moment density with latitude north for Model AS (black line with black circle), AJ (red), and AG (Blue). Here, black dots indicate latitude of upper most sub-faults. For reference, moment density from multiple CMT solution [*Tsai et al.*, 2005] is plotted with grey bars. Since the multiple CMT sources have the gentler dip angles than our fault plane models, the moment density for the multiple CMT solution is larger than that obtained from only seismic waveforms in this study. (see Figure 4.7b). (b) Variance reductions of vertical (blue circles), radial (red squares), and tangential (green triangles) at stations. Total seismic variance reduction is 55.10%. (c) Comparison of observed (blue) and best fitting GPS vectors for model AJ. Total GPS variance reduction is 94.14% (d) same as (c) for different geographic region. (e) same as (c) for slip model AG. (f) same as (d) for slip model AG. Total GPS variance reduction is 99.82%

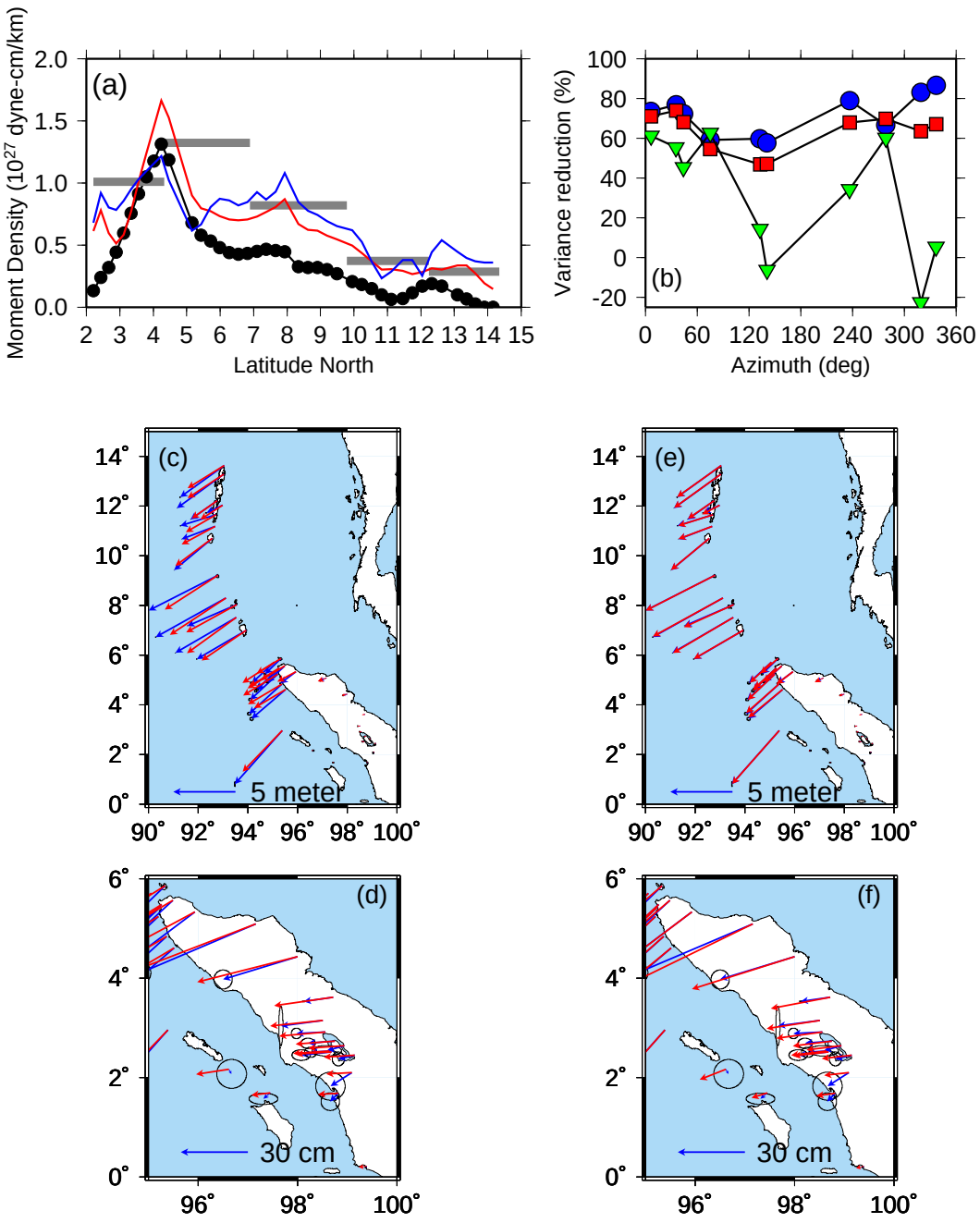

Figure 4.6: Same as Figure 5 for slip model BS, BJ, and BG. Total seismic variance reduction for model BJ is 57.90% and total GPS variance reductions for model BJ and BG are 95.95 and 99.92%, respectively.

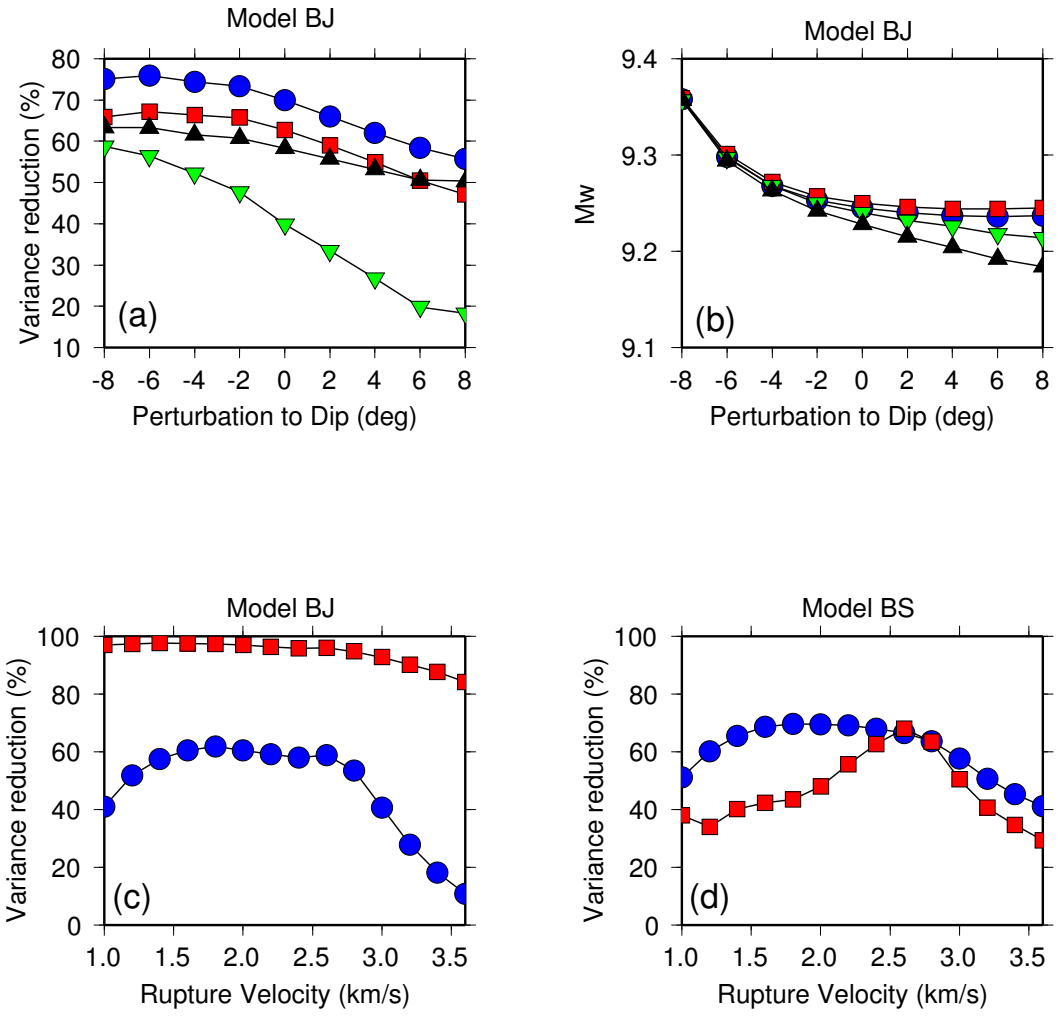

Figure 4.7: (a) Variation in seismic variance reduction with perturbation to the dip angle from geometry model B. Variance reductions are computed from slip models inverted from vertical (blue circles), radial (red squares), tangential (green triangles) and all 3 components (black triangles) with GPS static offsets. (b) Same as (a) for moment magnitude instead of variance reduction. (c) GPS (squares) and seismic (circle) variance reduction with rupture velocity for geometry model B. (d) Same as (c) for geometry model B and seismic-data-only inversion. The rupture velocity sensitivity tests for geometry model A show very similar results.

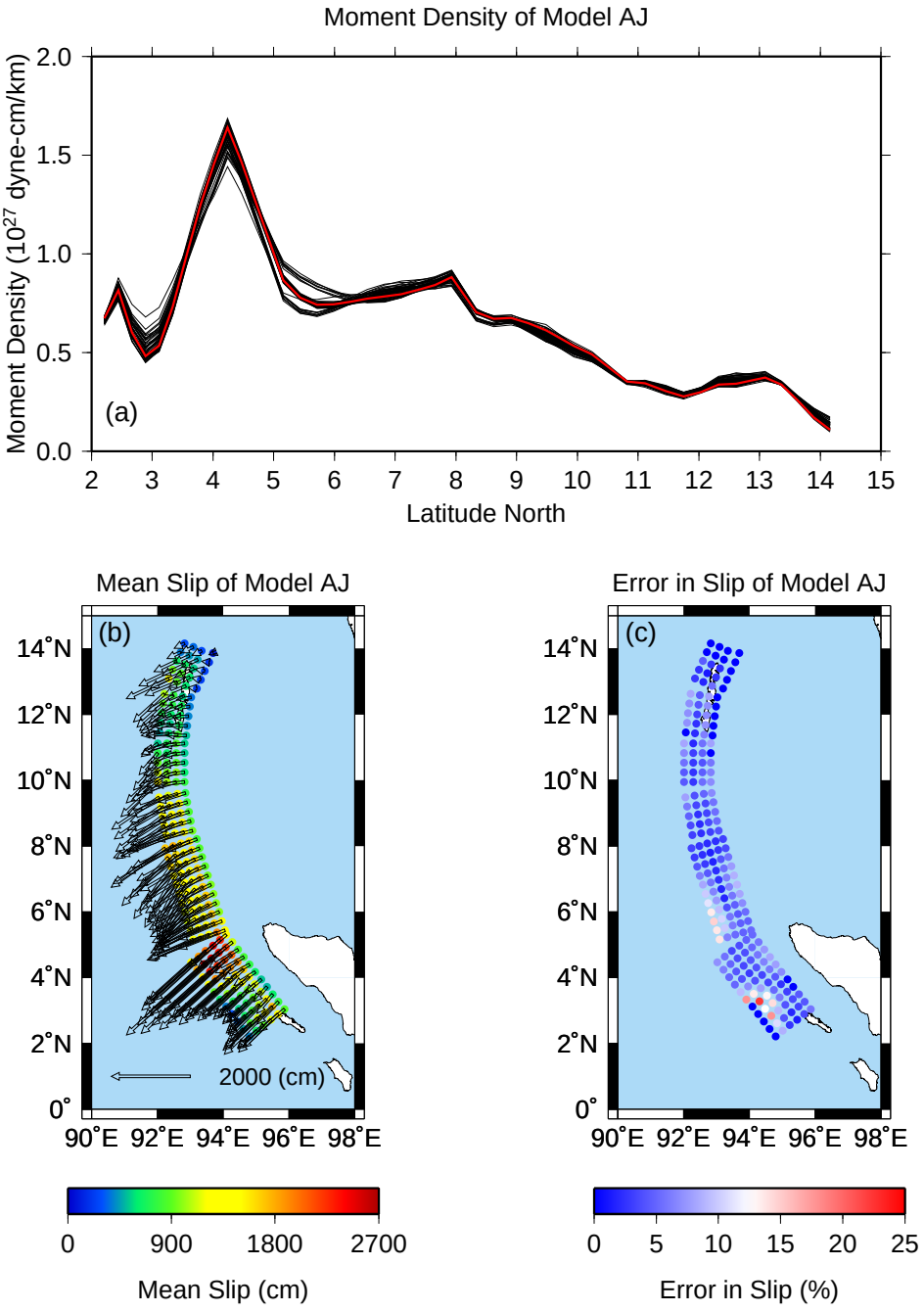

Figure 4.8: (a) Moment density obtained from jackknife method on geometry model A. Black curves indicate moment density inverted from each seismic subset of 8 stations and GPS static offsets. Thick red curve represents the mean of 45 moment density curves. (b) Mean slip distribution on geometry model A obtained from Jackknife method of inverted slip models from seismic and GPS subset A. (c) One standard deviation of (b) in percent. Small mean slip less than 20% of maximum slip is ignored to compute standard deviation.

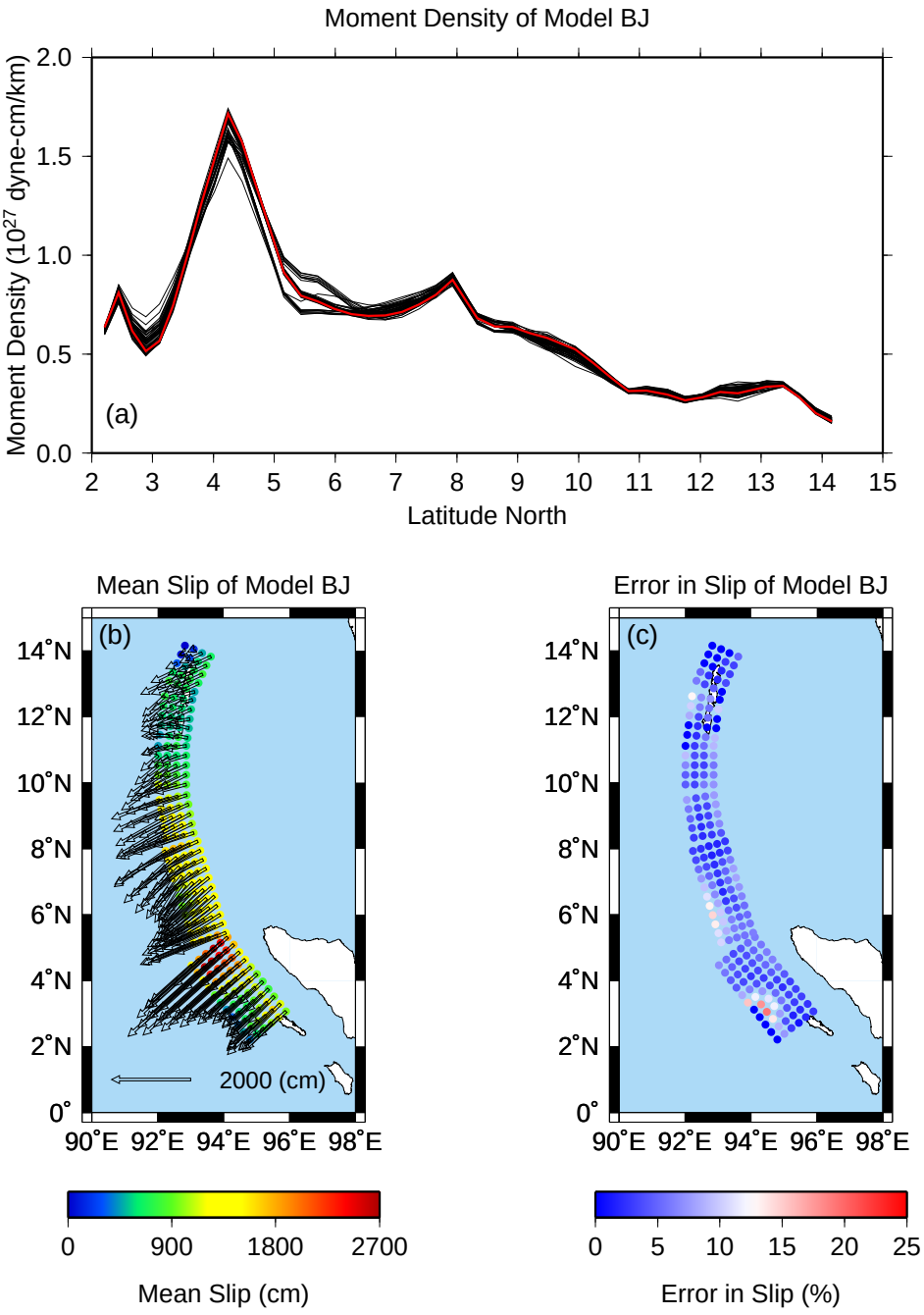

Figure 4.9: Same as figure 4.8 for geometry model B.

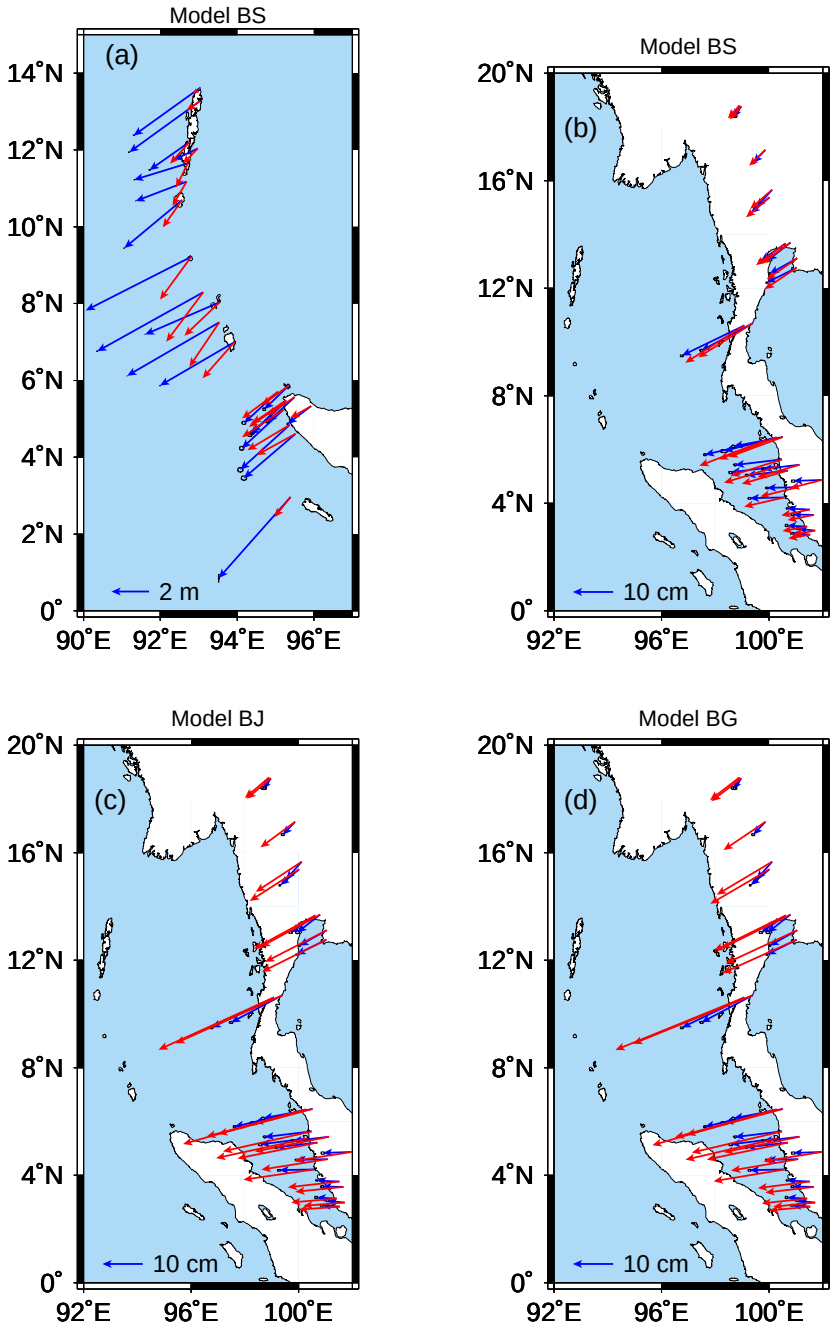

Figure 4.10: (a) Comparison between observed (red) and synthetic GPS vectors for slip model BS (inversion of seismic data on uniform dip rupture). Modeled GPS vectors underestimate the observations. (b) Same as (a) for GPS sites on the Malaysian peninsula located at larger distances from the rupture, which were not used in any of our inversions. (c) Same as (a) for slip model from the joint inversion BJ. (d) Same as (b) for slip model BG inverted from the near-field GPS data. The severe overprediction of static displacements at larger distances from models derived from the near-field GPS data is due to the half-space approximation of the Earth. See text for discussion.

Chapter 5

Conclusions

We used long period surface waves to study the very weak and continuous seismic sources (the hum of the Earth) as well as very large and transient source (the 2004 Sumatra-Andaman event). Here we briefly summarize the findings and inferences of these studies.

We developed an array-based method and detected and located the sources of the hum of the Earth using two regional seismic networks equipped with very broadband high dynamic range seismometers in California and Japan. After removing effects due to the elongated configuration of the array, we found that the incoming directions of the long period Rayleigh waves are stable during seasons at both arrays and show seasonal changes in directions. Maximum directions at both arrays point to north Pacific ocean and southern oceans during northern hemisphere winter and summer, respectively. Forward computation of an average stack amplitude for winter and summer by perturbing source excitations in space from uniformly distributed Rayleigh wave sources confirms that the source should be in the oceans not in the continents. Based on this observation, we suggest a possible mechanism of the excitation of the hum by atmosphere-ocean-seafloor coupling: 1) atmospheric storm energy converts into short period ocean waves, 2) longer ocean waves (e.g., infragravity wave) are generated by

non-linear interaction of short period waves; 3) elastic waves are generated by coupling of infragravity waves to the seafloor, through a process involving irregularities in the ocean floor topography.

The close inspection of the variations in long period seismic wave amplitudes at two arrays shows significant time delay of the hum signals at two arrays with BDSN leading by $\sim$ 8 hours. This observation indicates that the Rayleigh wave sources for BDSN and F-net are likely different, because an 8 hour time difference is difficult to explain by seismic wave propagation. However, the long term correlation of the seismic amplitude variations at two arrays shows that seismic sources for both arrays should be initiated by the same source. Therefore, we suggest a detailed non-linear conversion process, which is consisting of three steps: 1) non-linear interaction of short period ocean waves generates infragravity waves as the storm-related swell reaches the coast of north America; 2) non-linear coupling of the infragravity waves to the seafloor generates long period Rayleigh waves; 3) some free infragravity wave energy radiates out into the open ocean, propagates across the north Pacific basin, and couples to the seafloor when it reaches distant coasts north-east of Japan. The comparison of long period ($\sim$ 240 s) and short period (2-25 s) seismic amplitudes at BDSN, after removing effects due to earthquakes, shows very good correlation during northern hemisphere winter, but negligible correlation during summer. For F-net, we can see similar characteristics, but the correlation coefficient is quite smaller than in the case of BDSN. We also observe that the trend of seismic amplitudes at short periods shows significant annual changes with minimum occurring during summer. However, the amplitude is nearly constant for long period seismic amplitude. These observations indicate that the dominant sources of long and short period seismic energy should be the same and local during the winter, but more long period seismic energy is coming from other places (e.g., southern oceans) during the summer.

The detailed source process of a great earthquake, such as 2004 Sumatra-Andaman event, is very difficult to study because it shows different characteristics for different frequency contents. As of this writing (to our knowledge), we, for the first time,

jointly inverted global long period seismic waveforms and near field static offsets for slip distribution over the fault plane. The detailed fault geometry and rupture velocity are not well resolved from the given data set. However, error analysis shows that slip distribution is well constrained over the fault plane. Although it is still possible that our GPS static offsets are contaminated by post-seismic deformation, the moment magnitude constrained by joint inversion is 9.25. Our preferred slip model shows the maximum slip region is near 4° north, which is about 2° north from the epicenter, and the high slip region extends up to 10°N. The northern extension of the large slip region in our model is consistent with the tsunamigenic region based on back-projection of tsunami waves [*Lay et al.*, 2005].

Many different related investigations are still needed in order to understand the complex source processes of both sources studied in this dissertation. To better understand the complex conversion process from the ocean to the solid Earth, we need to compare all hum related signals and physical ocean parameters that may be related to the conversion of seismic energy from ocean wave, such as the direction of the ocean waves for various spectral contents, and also develop a method to locate the source regions more precisely. For the Sumatra-Andaman earthquake, we need to include the effect of sphericity and layering of the Earth into forward computation of the geodetic green's functions. By doing this, we can include far-field static offsets in our inversion, and can better constrain co-seismic slip on the fault plane.

Bibliography

Ammon, C. J., C. Ji, H.-K. Thio, D. Robinson, S. Ni, V. Hrorleifsdottir, H. Kanamori, T. Lay, S. Das, D. Helmberger, G. Ichinose, J. Polet, D. Wald, Rupture Process of the 2004 Sumatra-Andaman Earthquake, *Science*, **308**, 1133-1139, 2005.

Agnew, D. C., J. Berger, W. E. Farrell, F. Gilbert, G. Masters, and D. Miller, Project IDA: A decade in review, *Eos Trans. AGU*, **67**, 203-212, 1986.

Aki, K. and P.G. Richards, *Quantitative Seismology: Theory and Methods,* W. H. Freeman, New York, 1980.

Babcock, J. M. , B. A. Kirkendall, and J. A. Orcutt, Relationships between ocean bottom noise and the environment, *Bull. Seismol. Soc. Am.*, **84**, 1991-2007, 1994.

Banerjee, P., F. Pollitz, and R. Bürgmann, The Size and Duration of the Sumatra-Andaman Earthquake from Far-Field Static Offsets, *Science*, **308**, 1769-1772, 2005.

Banerjee, P., F. Pollitz, B. Nagarajan, and R. Bürgmann, Coseismic slip distribution of the 26 December 2004 Sumatra-Andaman and 28 March 2005 Nias earthquakes from GPS static offsets, *Bull. Seismol. Soc. Am.*, (submitted), 2006.

Benioff, H., F. Press, and S. Smith, Excitation of the free oscillations of hte Earth by earthquakes, *J. Geophys. Res.*, **66**, 605-619, 1961.

Beroza, G. and T. Jordan, Searching for slow and silent earthquakes using free oscillations, *J. Geophys. Res.*, **95**, 2485-2510, 1990.

Bilham, R., R. Engdahl, N. Feldi, and S. P. Satyabala, Partial and Complete Rupture of the Indo-Andaman Plate Boundary 1847-2004, *Seismol. Res. Lett.*, **76**, 299-311, 2005.

Bromirski, P. D., and F. K. Duennebier, The near-coastal microseism spectrum: spatial and temporal wave climate relationships, *J. Geophys. Res.*, **107**(B8), 2116, doi:10.1029/2001JB000265, 2002.

Bromirski, P. D., F. Duennebier, and R. A. Stephen, Mid-ocean microseisms, *Geochem. Geophys. Geosyst.*, **6**, Q04009, doi:10.1029/2004GC000768, 2005.

de Groot-Hedlin, C. D., Estimation of the rupture length and velocity of the Great Sumatra earthquake of Dec 26, 2004 using hydroacoustic signals, *Geophys. Res. Lett*, **32**, L11303, doi:10.1029/2005GL022695, 2005.

Dolenc, D., B. Romanowicz, D. Stakes, P. McGill, and D. Neuhauser, Observations of infragravity waves at the Monterey ocean bottom broadband station (MOBB), *Geochem. Geophys. Geosyst.*, **6**, Q09002, doi:10.1029/2005GC000988, 2005a.

Dolenc, D., B. Romanowicz, D. Stakes, P. McGill, and D. Neuhauser, Observations of Infragravity Waves at the Monterey Ocean Bottom Broadband Station (MOBB), *Eos Trans, AGU*, **85**(52), Fall Meet. Suppl., Abstract S34B-05, 2005b.

Dreger, D., and A. Kaverina, Seismic remote sensing for the earthquake source process and near-source strong shaking: A case of the October 16, 1999 Hector Mine earthquake, *Geophys. Res. Lett.*, **27**, 1941-1944, 2000.

Dreger, D., R. Uhrhammer, M. Pasyanos, J. Franck, and B. Romanowicz, Regional and far-regional earthquake locations and source parameters using sparse broadband networks: A test on the Ridgecrest Sequence, *Bull. Seismol. Soc. Am.*, **88**, 1353-1362, 1998.

Dziewonski, A. M. and D. L. Anderson, Preliminary reference Earth model, *Phys. Earth Planet. Inter.*, **25**, 297-356, 1981.

Dziewonski, A.M. and J.H. Woodhouse, Studies of the seismic source using normal-mode theory, in Kanamori, H. and E. Boschi, eds., *Earthquakes: observation, theory, and inter-*

pretation: notes from the International School of Physics "Enrico Fermi" (1982: Varenna, Italy), North-Holland Publ. Co., Amsterdam, pp. 45-137, 1983.

Efron, B., and R. J. Tibshirani, *An Introduction to the Bootstrap*, Chapman & Hall, New York, 1993.

Ekström, G, Time domain analysis of Earth's long-period background seismic radiation, *J. Geophys. Res.*, **106**, 26483-26493, 2001.

Ekström, G., and S. Ekström, Correlation of Earth's long-period background seismic radiation with the height of ocean waves, *Eos Trans. AGU*, **86**(52), Fall Meet. Suppl., Abstract S34B-02, 2005.

Ekström, G, J. Tromp, and E. Larson, Measurements and models of global surface wave propagation, *J. Geophys. Res.*, **102**, 8137-8157, 1997.

Ekström, G, M. Nettles, and G. A. Abers, Glacial earthquakes, *Science*, **302**, 622-624, 2003.

Elgar, S., T. H. C. Herbers, M. Okihiro, J. Oltman-Shay, and R. T. Guza, Observations of infragravity waves, *J. Geophys. Res.*, **97**, 15,573-15,577, 1992.

Fine, I. V., A. B. Rabinovich, and R. E. Thomson, The dual source regoin for the 2004 Sumatra tsunami, *Geophys. Res. Lett.*, **32**, L16602, doi:10.1029/2005GL023521, 2005.

Friedrich, A., Krüger, F., and K. Klinge, Ocean-generated microseismic noise located with the Grafenberg array, *J. Seismol.*, **2**, 47-64, 1998.

Fukao, Y., K. Nishida, N. Suda, K. Nawa, and N. Kobayashi, A theory of the Earth's background free oscillations, *J. Geophys. Res.*, **107**, 2206, doi:10.1029/2001JB000153, 2002.

Hartzell, S. H., and T. H. Heaton, Inversion of strong ground motion and teleseismic waveform data for the fault rupture history of the 1979 Imperial Valley, California earthquake, *Bull. Seismol. Soc. Am.*, **73**, 1553-1583, 1983.

Hasselmann, K., On the non-linear energy transfer in a gravity-wave spectrum, Part I. General Theory, *J. Fluid Mech.*, **12**, 481-500, 1962.

Hasselmann, K., A statistical analysis of the generation of microseisms, *Rev. Geophys.*, **1**, 177-210, 1963.

Haubrich, R. A., and K. McCamy, Microseisms: Coastal and pelagic sources, *Rev. Goephys.*, **7**, 539-571, 1969.

Herbers, T. H. C., S. Elgar, and R. T. Guza, Infragravity-frequency (0.005-0.05 Hz) motions on the shelf, Part I: Forced waves, *J. Phys. Oceanogr.*, **24**, 917-927, 1994.

Herbers, T. H. C., S. Elgar, and R. T. Guza, Generation and propagation of infragravity waves, *J. Geophys. Res.*, **100**, 24,863-24,872, 1995a.

Herbers, T. H. C., S. Elgar, R. T. Guza, and W. C. O Reilly, Infragravity-frequency (0.005 0.05 Hz) motions on the shelf, Part II: Free waves, *J. Phys. Oceanogr.*, **25**, 1063-1079, 1995b.

Ishii, M., P. M. Shearer, H. Houston, and J. E. Vidale, Extent, duration and speed of the 2004 Sumatra Andaman earthquake imaged by Hi-Net array, *Nature*, **435**, 933-936, 2005.

Kanamori, H., and J. Mori, Harmonic excitation of mantle Rayleigh waves by the 1991 eruption of Mount Pinatubo, Philippines, *Geophys. Res. Lett.*, **19**, 721-724, 1992.

Kaverina, A., D. Dreger, and E. Price, The Combined Inversion of Seismic and Geodetic Data for the Source Process of the 16 October 1999 M_w 7.1 Hector Mine, California Earthquake, *Bull. Seismol. Soc. Am.*, **92**, 1266-1280, 2002.

Kobayashi, N. and K. Nishida, Continuous excitation of planetary free oscillations by atmospheric disturbances, *Nature*, **395**, 357-360, 1998.

Krüger, F., and M. Ohrnberger, Tracking the rupture of the $M_w = 9.3$ Sumatra earthquake over 1,150 km at teleseismic distance, *Nature*, **435**, 937-939, 2005.

Lay, T., H. Kanamori, C. J. Ammon, M. Nettles, S. N. Ward, R. C. Aster, S. L. Beck, S. L. Bilek, M. R. Brudzinski, R. Butler, H. R. Deshon, G. Ekström, K. Satake, S. Sipkin, The Great Sumatra-Andaman Earthquake of 26 December 2004, *Science*, **308**, 1127-1133, 2005

Lomax, A., Rapid estimation of rupture extent for large earthquake: Application to the 2004, M9 Sumatra-Andaman mega-thrust, *Geophys. Res. Lett.*, **32**, L10314, doi:10.1029/2005GL022437, 2005.

Longuet-Higgins, M. S., A theory of the origin of microseism, *Philos. Trans. R. Soc. London, Ser. A*, **243**, 1-35, 1950.

Longuet-Higgins, M. S., and R. W. Stewart, Radiation stress and mass transport in surface gravity waves with application to "surf beats", *J. Fluid Mech.*, **13**, 481-504, 1962.

Muirhead, K. J. and R. Datt, The N-th root process applied to seismic array data, *Geophys. J. R. Astr. Soc.*, **47**, 197-210, 1976.

Munk, W., Surf beats, *EOS Trans. AGU.*, **30**, 849-854, 1949.

Munk, W., F. Snodgrass, and F. Gilbert, Long waves on the continental shelf: an experiment to separate trapped and leaking modes, *J. Fluid Mech.*, **20**,l 529-554, 1999.

Nawa, K, N. Suda, Y. Fukao, T. Sato, Y. Aoyama, and K. Shibuya, Incessant excitation of the Earth's free oscillations, *Earth Planets Space*, **50**, 3-8, 1998.

Nawa, K, N. Suda, Y. Fukao, T. Sato, Y. Tamura, K. Shibuya, H. McQueen, H. Virtanen, and J. Kääriäinen, Incessant excitation of the Earth's free oscillations: global comparison of superconducting gravimeter records, *Phys. Earth Planet. Int.*, **120**, 289-297, 2000.

Nawa, K., N. Suda, S. Aoki, K. Shibuya, and T. Sato, Sea level variation in seismic normal mode band observed with on-ice GPS and on-land SG at Syowa Station, Antarctica, *Geophys. Res. Lett.*, **30**, 1402, doi:10.1029/2003GL016919, 2003.

Ni, S., H. Kanamori, and D. Helmberger, Energy radiation from the Sumatra earthquake, *Nature*, **434**, 582, 2005.

Nishida, K., and Y. Fukao, Spatial variations of excitation amplitudes of Earth's background free oscillations, *Eos Trans. AGU*, **84**(46), Fall Meet. Suppl., Abstract S31B-1068, 2004.

Nishida, K. and N. Kobayashi, Statistical features of Earth's continuous free oscillations, *J. Geophys. Res.*, **104**, 28741-28750, 1999.

Nishida, K., N. Kobayashi, and Y. Fukao, Resonant oscillations between the solid Earth and the atmosphere *Science*, **287**, 2244-2246, 2000.

Nishida, K., N. Kobayashi, and Y. Fukao, Origin of Earth's ground noise from 2 to 20 mHz, *Geophys. Res. Lett.*, **29**, 1413, doi:10.1029/2001GL013862, 2002.

Nishida, K., Y. Fukao, S. Watada, N. Kobayashi, M. Tahira, N. Suda, K. Nawa, T. Oi and T. Kitajima, Array observation of background atmospheric waves in the seismic band from 1 mHz to 0.5 Hz, *Geophys. J. Int.*, **162**, 824-840, 2005.

Okada, Y., Surface deformation due to shear and tensile faults in a half-space, *Bull. Seismol. Soc. Am.*, **75**, 1135-1154, 1985.

Okihiro, M., R. T. Guza, and R. J. Seymour, Bound infragravity waves, *J. Geophys. Res.*, **97**, 11,453-11,469, 1992.

Park, J., T.-R. A. Song, J. Tromp, E. Okal, S. Stein, G. Roult, E. Clevede, G. Laske, H. Kanamori, P. Davis, J. Berger, C. Braienberg, M. V. Camp, X. Lei, H. Sun, H. Xu, and S. Rosat, Earth's Free Oscillations Excited by the 26 December 2004 Sumatra-Andaman Earthquake, *Science*, **308**, 1139-1144, 2005.

Peterson, J., *Observations and Modeling of Seismic Background Noise,* USGS Open File Report 93-322, United States Geological Survey, Albuquerque, NM, 1993.

Rhie, J., and B. Romanowicz, Detection and location of potential sources of background low frequency surface wave energy, *Eos Trans AGU*, **83**, Fall Meet. Suppl., Abstract S12A-1184, 2002

Rhie, J., and B. Romanowicz, Detection and location of long period surface wave energy sources, *Eos Trans. AGU*, **84**(46), Fall Meet. Suppl., Abstract S42E-0211, 2003.

Rhie, J., and B. Romanowicz, Excitation of Earth's continuous free oscillations by atmosphere-ocean-seafloor coupling, *Nature*, **431**, 552-556, 2004.

Rhie, J., and B. Romanowicz, A study on the relation between ocean storms and the Earth's hum, *Geochem. Goephys. Geosyst.*, (submitted), 2006.

Rhie, J., D. Dreger, R. Bürgmann, and B. Romanowicz, Joint slip inversion of the 2004 Sumatra-Andaman earthquake from long period global seismic waveforms and GPS static offsets, *Bull. Seismol. Soc. Am.*, (submitted), 2006.

Rost, S., and C. Thomas, Array seismology: Method and applications, *Rev. Geophys.*, **40**, doi:10.1029/2000RG000100, 2002.

Rouland, D., C. Condis, C. Parmentier, and A. Souriau, Previously undetecdted earthquakes in the Southern Hemisphere from long-period Geoscope data, *Bull. Seismol. Soc. Am.*, **82**, 2448-2463, 1992.

Roult G. and W. Crawford, Analysis of 'background' free oscillations and how to improve resolution by subtracting the atmospheric pressure signal, *Phys. Earth Planet. Int.*, **121**, 325-338, 2000.

Roult G. and J. P. Montagner, The GEOSCOPE program, *Ann. Geofis.*, **37**, 1054-1059, 1994.

Sambridge, M. S. and B. L. N. Kennett, A novel method of hypocenter location, *Geophys. J. R. Astr. Soc.*, **87**, 679-697, 1986.

Schimmel M. and H. Paulssen, Noise reduction and detection of weak, coherent signals through phase-weighted stacks, *Geophys. J. Int.*, **130**, 497-505, 1997.

Schulte-Pelkum, V., P. S. Earle, and F. L. Vernon, Strong directivity of ocean-generated seismic noise, *Geochem. Geophys. Geosyst.*, **5**, doi:10.1029/2003G3000520, 2004.

Shapiro, N. M., M. Campillo, L. Stehly, and M. H. Ritzwoller, High-Resolution Surface-Wave Tomography from Ambient Seismic Noise, *Science*, **307**, 1615-1618, 2005.

Stein, S., and E. A. Okal, Speed and size of the Sumatra earthquake, *Nature*, **434**, 581-582, 2005.

Subarya, C., M. Chlieh, L. Prawirodirdjo, J.-P. Avouac, Y. Bock, K. Sieh, A. J. Meltzner, D. H. Natawidjaja, and R. McCaffrey, Plate-boundary deformation of the great Aceh-Andaman earthquake, *Nature*, (in press), 2006.

Suda, N. K. Nawa, and Y. Fukao, Earth's background free oscillations, *Science*, **279**, 2089-2091, 1998.

Sutton, G. H., W. G. McDonald, D. D. Prentiss, and S.N. Thanos, Ocean-bottom seismic observatories, *Proc, IEEE*, **53**, 1909-1921, 1965.

Tanimoto, T., Jet stream, roaming ocean waves,and ringing Earth, *Eos Trans. AGU*, **84**(46), Fall Meet. Suppl., Abstract S12F-04, 2003.

Tanimoto, T., The oceanic excitation hypothesis for the continuous oscillations of the Earth, *Geophys. J. Int.*, **160**, 276-288, 2005.

Tanimoto, T. and J. Um, Cause of continuous oscillations of the Earth, *J. Geophys. Res.*, **104**, 28723-28739, 1999.

Tanimoto, T., J. Um, K. Nishida, and N. Kobayashi, Earth's continuous oscillations observed on seismically quiet days, *Geophys. Res. Lett.*, **25**, 1553-1556, 1998.

Tolman, H. L., User manual and system documentation of WAVEWATCH III, version 1.18, *Tech. Rep. Ocean Modeling Branch Contribution 166*, NOAA/NWS/NCEP, 1999.

Tolstoy, M., and D. R. Bohnenstiehl, Hydroacoustic constraints on teh rupture duration, length, and speed of the great Sumatra-Andaman earthquake, *Seismol. Res. Lett.*, **76**, 419-425, 2005.

Tsai, V. C., M. Nettles, G. Ekström, and A. M. Dziewonski, Multiple CMT source analysis of the 2004 Sumatra earthquake, *Geophys. Res. Lett.*, **32**, L17304, doi:10.1029/2005GL023813, 2005.

Tucker, M. J., Surf beats: sea waves of 1 to 5 min period, *Proc. R. Soc. London, Ser. A*, **207**, 565-573, 1950.

Uhrhammer, R. A., D. Dreger, and B. Romanowicz, Best practice in earthquake location using broadband three-component seismic waveform data, *Pure Appl. Geophys.*, **158**, 259-276, 2001.

Vigny, C., W. J. F. Simons, S. Abu, R. Bamphenyu, C. Satirapod, N. Choosakul, C. Subarya, A. Socquet, K. Omar, H. Z. Abidin, and B. A. C. Ambrosius, Insight into the 2004 Sumatra-Andaman earthquake from GPS measurements in southeast Asia, *Nature*, **436**, 201-206, 2005.

von Seggern, D., Relative location of seismic events using surface waves, *Geophys. J. R. Astr. Soc.*, **26**, 499-513, 1972.

Watada, S., and G. Masters, Oceanic excitation of the continuous oscillations of the Earth, *Eos Trans. AGU*, **82**(47), Fall Meet. Suppl., Abstract S32A-0620, 2001.

Webb, S., Broadband seismology and noise under the ocean, *Rev. Geophys.*, **36**, 105-142, 1998.

Webb, S., and W. Crawford, Long-period seafloor seismology and deformation under ocean waves, *Bull. Seismol. Soc. Am.*, **89**, 1535-1542, 1999.

Webb, S. C., and C. S. Cox, Observations and modeling of seafloor microseisms, *J. Geophys. Res.*, **91**, 7343-7358, 1986.

Webb, S., X. Zhang, and W. Crawford, Infragravity waves in teh deep ocean, *J. Geophys. Res.*, **96**, 2723-2736, 1999.

Wessel, P., and W. H. F. Smith, Free software helps map and display data, *EOS*, **72**, 445-446, 1991.

Wielandt, E., and G. Streckeisen, The leaf spring seismometer: design and performance, *Bull. Seismol. Soc. Am.*, **72**, 2349-2367, 1982.

Wielandt, E., and J. M. Steim, The very broad band seismograph; Part I, Sensor, *Eos, Trans. AGU*, **66**, 312, 1985.

Zürn, W. and Widmer, R., On noise reduction in vertical seismic records below 2 mHz using local baromatric pressure, *Geophys. Res. Lett.*, **22**, 3537-3540, 1995.